Modelling Arctic Lower Tropospheric Ozone: processes controlling seasonal variations

Wanmin Gong[1], Stephen R. Beagley[1], Kenjiro Toyota[1], Henrik Skov[2], Jesper Heile Christensen[2], Alex Lupu[1], Diane Pendlebury[1], Junhua Zhang[1], Ulas Im[2], Yugo Kanaya[3], Alfonso Saiz-Lopez[4], Roberto Sommariva[5,6], Peter Effertz[7,8], John W. Halfacre[9], Nis Jepsen[10], Rigel Kivi[11], Theodore K. Koenig[12], Katrin Müller[13], Claus Nordstrøm[2], Irina Petropavlovski[7,8], Paul B. Shepson[14], William R. Simpson[15], Sverre Solberg[16], Ralf M. Staebler[1], David W. Tarasick[1], Roeland Van Malderen[17], Mika Vestenius[18]

[1]Air Quality Research Division, Science and Technology Branch, Environment and Climate Change Canada, Toronto, M3H 5T4, Canada
[2]Department of Environmental Science, iClimate, Aarhus University, Roskilde, 4000, Denmark
[3]Research Institute for Global Change (RIGC), Japan Agency for Marine–Earth Science and Technology (JAMSTEC), Yokohama 2360001, Japan
[4]Department of Atmospheric Chemistry and Climate, Institute of Physical Chemistry Blas Cabrera, CSIC, Madrid, 28006, Spain
[5]School of Geography, Earth and Environmental Sciences, University of Birmingham, Birmingham, B15 2TT, UK
[6]School of Chemistry, University of Leicester, Leicester, UK
[7]Cooperative Institute for Research in Environmental Sciences, University of Colorado, Boulder, CO, 80309, USA
[8]National Oceanic and Atmospheric Administration Global Monitoring Laboratory, Boulder, CO 80305, USA
[9]Wolfson Atmospheric Chemistry Laboratories, Department of Chemistry, University of York, York YO10 5DD, United Kingdom
[10]Danish Meteorological Institute, 2100 Copenhagen, Denmark
[11]Space and Earth Observation Centre, Finnish Meteorological Institute, Tähteläntie 62, 99600 Sodankylä, Finland
[12]Division of Environment and Sustainability, The Hong Kong University of Science and Technology, Hong Kong 999077
[13]Alfred Wegener Institute (AWI), Helmholtz Centre for Polar and Marine Research, Telegrafenberg A43, 14473 Potsdam, Germany
[14]Stony Brook University, Stony Brook, NY 11794, USA
[15]Department of Chemistry, Biochemistry, and Geophysical Institute, University of Alaska Fairbanks, Fairbanks, AK 99775-6160, USA
[16]Norwegian Institute for Air Research (NILU), Kjeller, Norway
[17]Royal Meteorological institute of Belgium (KMI), Brussels, Belgium
[18]Finnish Meteorological Institute, Air Quality Expert services, FI-00101 Helsinki, Finland

Correspondence to: Wanmin Gong (wanmin.gong@ec.gc.ca)

Abstract

Previous assessments on modelling Arctic tropospheric ozone (O_3) have shown that most atmospheric models continue to experience difficulties in simulating tropospheric O_3 in the Arctic, particularly in capturing the seasonal variations at coastal sites, primarily attributed to the lack of representation of surface bromine chemistry in the Arctic. In this study, two independent chemical transport models (CTMs), DEHM (Danish Eulerian Hemispheric Model) and GEM-MACH (Global Environmental Multi-scale – Modelling Air quality and Chemistry), were used to simulate Arctic lower tropospheric O_3 for the year 2015 at considerably higher horizontal resolutions (25-km and 15-km, respectively) than the large-scale models in the previous

assessments. Both models include bromine chemistry and a representation of snow-sourced bromine mechanism: a blowing-snow bromine source mechanism in DEHM and a snowpack bromine source mechanism in GEM-MACH. Model results were compared with a suite of observations in the Arctic, including hourly observations from surface sites and mobile platforms (buoys and ship) and ozonesonde profiles, to evaluate models' ability to simulate Arctic lower tropospheric O_3, particularly in

45 capturing the seasonal variations and the key processes controlling these variations.

The study found that both models behave quite similarly outside the spring period and are able to capture the observed overall surface O_3 seasonal cycle and synoptic scale variabilities, as well as the O_3 vertical profiles in the Arctic. GEM-MACH (with the snowpack bromine source mechanism) was able to simulate most of the observed springtime Ozone Depletion Events (ODEs) at the coastal and buoy sites well, while DEHM (with the blowing-snow bromine source mechanism) simulated much

50 fewer ODEs. The study showed that the springtime O_3 depletion process plays a central role in driving the surface O_3 seasonal cycle in Central Arctic, and that the bromine-mediated ODEs, while occurring most notably within the lowest few hundred metres of air above the Arctic Ocean, can induce a 5-7% of loss in the total pan-Arctic tropospheric O_3 burden during springtime. The model simulations also showed an overall enhancement in the pan-Arctic O_3 concentration due to northern boreal wildfire emissions in summer 2015; the enhancement is more significant at higher altitudes. Higher O_3 excess ratios

55 ($\Delta O_3/\Delta CO$) found aloft compared to near the surface indicate greater photochemical O_3 production efficiency at higher altitudes in fire-impacted air masses. The model simulations further indicated an enhancement in NO_y in the Arctic due to wildfires; a large portion of NO_y produced from the wildfire emissions is found in the form of PAN that is transported to the Arctic, particularly at higher altitudes, potentially contributing to O_3 production there.

1 Introduction

60 Tropospheric ozone (O_3) is a green-house gas (GHG) and, near the surface, an air pollutant harmful for human health as well as affecting crop and ecosystem productivity (Archibald et al., 2020). It also plays a central role in tropospheric chemistry owing to its role in the initiation of photochemical oxidation processes via direct reaction, photolysis and the subsequent reactions of the photoproducts to form the hydroxyl (OH) radical (Monks et al., 2015a). The Arctic is an area currently undergoing 4 times faster warming than the rest of the world (Rantanen et al., 2022) and, as a result, changes in local

65 anthropogenic and natural sources of ozone precursors and in the transport pattern from lower latitudes as well as increased vertical mixing are to be expected. For increasing confidence in the projection of future Arctic tropospheric O_3 from different anthropogenic and/or natural perturbations, it is important to have a modelling capability for simulating the observed present-day Arctic tropospheric O_3, including its spatial-temporal variability and its sources, sinks, and the associated atmospheric processes.

70 The tropospheric O_3 budget in the Arctic has contributions from long-range transport from mid-latitudes, photochemical production from anthropogenic and natural precursors either local (within the Arctic) or transported to the Arctic, and transport

from the stratosphere (Hirdman et al., 2010; Law et al., 2014). In turn, the transport of Arctic ozone-poor and halogen-rich air masses through polar front intrusions toward lower latitudes reduce ozone in the northern mid-latitudes (Fernandez et al., 2024). Processes contributing to tropospheric O_3 loss or removal from the Arctic atmosphere include photochemical
75 destruction via HO_x chemistry involving hydroperoxyl (HO_2) and OH radicals (Arnold et al., 2015; Wang et al., 2003), reactions with halogen species (e.g., Barrie et al., 1988; Simpson et al., 2007; Skov et al., 2004; Wang et al., 2019), direct reaction with biogenic organic compounds (BVOCs; primarily isoprene) under low NOx conditions, and surface removal through dry deposition (Clifton et al., 2020; Van Dam et al., 2016). These processes vary with geographical locations and have distinct seasonal patterns, which give rise to the seasonal variations in the Arctic tropospheric O_3. Long-term ground-based
80 observations in the Arctic show distinctively different surface O_3 seasonal cycles depending on whether the sites are located near the coast, inland, or at high elevation (Whaley et al., 2023). For example, Whaley et al. (2023) showed that coastal sites have springtime minima due to halogen chemistry causing O_3 depletion events (ODEs) and maxima during the winter, while inland sites near the Arctic Circle in the European subarctic boreal region have seasonal cycles with maxima in spring (April) and minima in summer (August), resembling the seasonal cycles at remote European locations. At the high-elevation Summit
85 site (located in Greenland at ~ 3000 m ASL), the observed O_3 seasonal cycle has a late spring (May) maximum and an early fall (September) minimum, which is consistent with the seasonal cycle of free tropospheric O_3 based on long-term ozonesonde observations in the Arctic (Christiansen et al., 2017).

The ability of current models to simulate Arctic tropospheric O_3 has been evaluated in several studies (e.g., Monks et al., 2015b; Shindell et al., 2008; Whaley et al., 2023) involving largely global models. These studies have found that there were
90 large variabilities amongst the model simulations and that the models performed particularly poorly in capturing the observed surface O_3 seasonal cycles at coastal sites. In a recent assessment on Arctic tropospheric O_3, Whaley et al. (2023) suggested that, despite the model development and updates over the past decade or so, model results are still highly variable and have not increased in accuracy for representing Arctic tropospheric O_3. The poor model performance during spring found in these studies has been linked to the missing representation of halogen chemistry in the models. A recent study using a global
95 chemistry-climate model has highlighted the need to add halogens in a global model to reproduce Arctic ozone seasonality (Fernandez et al., 2024). Springtime ODEs have been primarily attributed to catalytic destruction of O_3 by reactive bromine (Barrie et al., 1988; Hausmann and Platt, 1994; Simpson et al., 2007; Skov et al., 2004; Wang et al., 2019) released from snowpacks (Custard et al., 2017; Pratt et al., 2013) and blowing snow (Jones et al., 2009; Yang et al., 2008) over sea ice via photochemical reactions in/on snow particles and cycled through heterogeneous reactions on aerosol surfaces (Fan and Jacob,
100 1992; Michalowski et al., 2000; Toyota et al., 2014). Mechanisms to represent polar springtime bromine explosions and ODEs have been developed and tested in various atmospheric models, by considering both blowing snow (e.g., Yang et al., 2008, 2010, 2020; Huang and Jaeglé, 2017; Huang et al., 2020; Marelle et al., 2021; Swanson et al., 2022) and snowpacks (e.g., Toyota et al., 2011; Falk and Sinnhuber, 2018; Marelle et al., 2021; Swanson et al., 2022), with varying degrees of success when compared with observations of reactive bromine and O_3 in the Arctic (and Antarctic). In addition, Fernandez et al. (2019)

105   implemented a different parameterization for the source terms of inorganic gaseous halogens (chlorine, bromine, and iodine) on polar sea ice in their global chemistry-climate model. Clearly, our understanding of the mechanisms and dynamics controlling the ODEs in the Arctic springtime is still evolving, as a recent study suggested that iodine radical chemistry may also contribute significantly to Arctic O_3 destruction during the extended sunlit period not only in summer but also substantially during ODEs in spring (Benavent et al., 2022) with effects far south of the Arctic area (Fernandez et al., 2024).

110   Aside from locations where air masses are persistently in contact with sea ice (e.g., Bottenheim et al., 2009; Bottenheim and Chan, 2006; Van Dam et al., 2013), Arctic surface O_3 concentrations are often lowest during summer (Whaley et al., 2023), which can be associated with reduced transport from lower latitudes, photochemical degradation, and increased surface removal (Barrie, 1986; Law et al., 2014). However, spatiotemporal variabilities in the biogenic emissions of volatile organic compounds (VOCs) (e.g., (Aaltonen et al., 2011; Angot et al., 2020; Junninen et al., 2022; Pernov et al., 2021) and the dry
115   deposition of O_3 (e.g., Helmig et al., 2007, 2009; Van Dam et al., 2016) are still understudied for the quantification of their impacts on the summertime Arctic surface O_3. On the other hand, there is increasing evidence that biomass burning (boreal wildfires) is an important source of pollutants in the Arctic during late spring to fall (Law et al., 2014). The estimate of their impact on Arctic ozone is challenged by uncertainties in characterizing the net effects of simultaneously emitted aerosols, nitrogen oxides (NO_x) and VOCs in the perturbations of photochemical and heterogeneous surface reactions within fire plumes
120   (Jaffe and Wigder, 2012). While the ARCTAS-B aircraft campaign found that boreal fire emissions had only negligible impact on tropospheric ozone profiles in summer 2008 over Alaska and Canada (Alvarado et al., 2010; Moeini et al., 2020; Singh et al., 2010), a multi-model study by Arnold et al. (2015) suggests that emissions from biomass burning lead to large-scale enhancement in high-latitude NO_y and tropospheric O_3 during summer.

    In this study, model simulations for the year 2015 from two different models, GEM-MACH (Global Environmental Multi-
125   scale – Modelling Air quality and Chemistry) and DEHM (Danish Eulerian Hemispheric Model), were conducted over the Arctic, at relatively high resolution (15- and 25-km, respectively). Both models include atmospheric reactive bromine chemistry, but the two models employ different bromine source mechanisms over sea ice in the Arctic, namely a snowpack-sourced mechanism (in GEM-MACH) and a blowing-snow-sourced mechanism (in DEHM). The model results are compared with a range of observations in the Arctic, including surface sites, mobile platforms (buoys, ship, and airborne), and
130   ozonesondes, to evaluate the models' ability to simulate the Arctic lower tropospheric O_3, particularly in capturing the seasonal cycles of surface and lower tropospheric O_3 in the Arctic. Sensitivity simulations turning off bromine chemistry were conducted by both models, allowing an in-depth examination of the representation of bromine sources and reactions on modelled ODEs in the Arctic. Additional sensitivity simulations turning off wildfire emissions were also undertaken (using GEM-MACH) to assess the impact of boreal fire emission on Arctic O_3. To our knowledge, this study is a first attempt in
135   simulating Arctic lower tropospheric O_3 seasonal variability using regional models at much higher spatial resolution (~ 20-km) than global models. The study aims to address the following questions:

- How well can current state-of-the-art regional models simulate the observed Arctic surface O_3 seasonal cycle?

- What are the key processes driving the Arctic surface O_3 seasonal cycle, and how well are these processes represented in the models?

140   - How do the different processes contribute to the Arctic lower tropospheric O_3 budget, and in particular, what is the impact of spring ODEs on Arctic lower tropospheric O_3, locally and Arctic-wide?

In what follows, we will first provide a brief description of the study methodology including model configuration and simulation setup as well as measurement data used (Section 2). We will then discuss model simulations and comparison with observations (Section 3), including an examination of modelled seasonal distribution of lower tropospheric O_3 in the Arctic

145   and an evaluation against surface and ozonesonde observations. In Section 4, we will examine the model simulation of the Arctic springtime ODEs in details, including the roles of different bromine sources on ODEs, uncertainty in the parameterization of snowpack bromine source mechanism, and comparative roles of snowpack bromine emission and atmospheric bromine production through heterogeneous cycling on aerosol surfaces. We will also examine the impact of boreal wildfires on summertime Arctic O_3, as well as how different processes contribute to the pan-Arctic lower tropospheric O_3

150   budget. The findings from this study are summarised in Section 5 with outlooks on modelling the Arctic lower tropospheric O_3.

2 Study method

2.1 Models and simulation setup

Two chemical transport models were used in this study, DEHM (the Danish Eulerian Hemispheric Model) and GEM-MACH

155   (Global Environmental Multiscale model – Modelling Air quality and Chemistry). Brief descriptions of the two models and their setup for the year 2015 simulations are provided in this section. Key model features and configurations are summarised in Appendix 1. The year 2015 was selected on the basis that it was one of the years featured in the recent AMAP assessment of short-lived climate forcers (AMAP, 2021) and a reference year for ECLIPSE (Evaluating the Climate and Air Quality Impacts of Short-Lived Pollutants) v6b emission dataset which was used by all the models participated in the AMAP

160   assessment (Whaley et al., 2022) as well as by the two models in this study.

2.1.1 DEHM

DEHM is a three-dimensional atmospheric chemistry transport model used to study long-range transport of air pollution in the Northern Hemisphere to the Arctic originated from anthropogenic and natural sources outside the Arctic (Brandt et al., 2012; Christensen, 1997; Eckhardt et al., 2015; Heidam et al., 2004; Massling et al., 2015; Skov et al., 2020). The DEHM model has

165   been used for many years to study the transport of air pollution from the mid-latitudes, presented in many articles (e.g., Barrie et al., 2001; Christensen et al., 2004; Hansen et al., 2008; Hole et al., 2009; Thomas et al., 2022), and has contributed to many

of the assessments in the Arctic Monitoring and Assessment Program (AMAP) since its first assessment in 1998 (Kämäri et al., 1998).

In this study the model was set up with two nested model domains: an outer domain of 300 x 300 grid points with a horizontal
170 resolution of 75 km x 75 km (polar stereographic projection, true at 60°N) covering the whole northern hemisphere and a nested domain covering the whole Arctic down to approximately 50°N at a higher resolution of 25 km x 25 km; both model domains have the North Pole at the centre of the grid (the core high-resolution domain is shown in Fig. 1(a)). In the vertical, there are 29 unevenly distributed layers that extend up to 100 hPa, approximately 15km above sea level (ASL), with the finest resolution in the atmospheric boundary layer (lowest model layer of ~20 m, 3 – 4 model layers below the lowest 100 m).
175 DEHM is driven by meteorological fields from the numerical weather prediction model WRF v4.1 (Skamarock et al., 2008), where the model grid setup is identical to that of the DEHM model system both horizontally and vertically, so that the 2 and 3-d WRF data can be directly mapped onto the DEHM grids without needing interpolation. The WRF model is driven by global data from the ERA5 reanalysis from ECMWF (Hersbach et al., 2017). The WRF data were archived with 1 hour resolution and interpolated in time within the DEHM model.
180 The basic chemical scheme in DEHM includes 89 different species and is based on the scheme by Strand and Hov (1994), with modifications based on the chemical scheme in the EMEP model (Simpson et al., 2012) and ACDEP model (Hertel et al., 1995). The chemical scheme has been extended with a detailed description of the inorganic heterogeneous ammonia chemistry and a Volatility Basis Set (VBS) based scheme to describe the formation of Secondary Organic Aerosols (SOA) (Bergström et al., 2012). Furthermore, reactions concerning the wet-phase production of sulfate have been included, based on Jonson and
185 Isaksen (1993). The basic chemistry module is extended with bromine chemistry based on the work by Yang et al. (2010) with bromine emissions from blowing snow, sea salt and $CHBr_3$ and CH_2Br_2 from open oceans (see 2.1.3). The model setup used describes concentration fields of 75 photo-chemical compounds (including NO_x, SO_x, VOC, NH_x, CO, O_3 etc.), 12 species for the SOA part and several classes of particulate matter as EC, primary OM, primary ash/dust and sea salt. All aerosols are assumed to be presented as a single bulk representation with a particle diameter of 0.33 µm for the fine fraction and 4.8 µm
190 for the coarse fraction. The anthropogenic emissions used are from the ECLIPSE v6b with a 0.5° x 0.5° resolution (Klimont et al., 2017). The emissions from the EMEP expert database (European Monitoring and Evaluation Programme) are used for the areas over Europe with 0.1° x 0.1° resolution (see https://www.ceip.at/). Furthermore, the biomass burning emissions are obtained from the Global Fire Assimilation System (GFAS) from ECMWF (Kaiser et al., 2012), which have a horizontal resolution of a 0.1° x 0.1° on a daily time basis. The calculation of the dry deposition velocity is based on the resistance
195 method; for land-surface and sea-ice it is based on Simpson et al. (2012), while for open sea it is based on Hertel et al. (1995), where the surface resistance takes into account the solubility and reactivity in the water. The parameterisation of wet deposition is based on a simple scavenging ratio formulation with in-cloud and below-cloud scavenging coefficients for both gas and particulate phases (see Simpson et al., 2012 and Huang et al., 2010).

2.1.2 GEM-MACH

200   GEM-MACH is the Environment and Climate Change Canada (ECCC) air quality prediction model. It consists of an online tropospheric chemistry module embedded within ECCC's GEM numerical weather forecast model (Charron et al., 2012; Côté et al., 1998a, b). The chemistry module includes a comprehensive representation of air quality processes, such as gas-phase chemistry, aqueous-phase chemistry, and aerosol chemical thermodynamics and microphysical processes (e.g., Gong et al., 2015; Makar et al., 2015b, a; Moran et al., 2018). Specifically, gas-phase chemistry is represented by a modified ADOM-II

205   mechanism with 47 species and 114 reactions (Lurmann et al., 1986); inorganic aerosol thermodynamics is parameterized by a modified version of the ISORROPIA algorithm of Nenes et al. (1999), as described in detail in Makar et al. (2003); SOA formation is parameterized using a two-product, overall, or instantaneous aerosol yield formation (Odum et al., 1996; Jiang, 2003; Stroud et al., 2018); aerosol microphysical processes, including nucleation and condensation (sulfate and SOA), hygroscopic growth, coagulation, and dry deposition and sedimentation, are parameterized as in Gong et al. (2003); the

210   representation of cloud processing of gases and aerosols includes uptake and activation, aqueous-phase chemistry, and wet removal (Gong et al., 2006, 2015). Aerosol chemical composition is represented by eight components: sulfate, nitrate, ammonium, elemental carbon (EC), primary organic aerosol (POA), secondary organic aerosol (SOA), crustal material (CM), and sea salt; aerosol particles are assumed to be internally mixed. A sectional approach is used for representing aerosol size distribution. For the current 2015 pan-Arctic simulations, a 12-bin (between 0.01 and 40.96 μm in diameter, logarithmically

215   spaced: 0.01–0.02, 0.02–0.04, 0.04–0.08, 0.08–0.16, 0.16–0.32, 0.32–0.64, 0.64–1.28, 1.28–2.56, 2.56–5.12, 5.12–10.24, 10.24–20.48, and 20.48–40.96 μm) configuration is used.

The Arctic implementation of GEM-MACH includes several upgrades: the inclusion of dimethyl sulfide (DMS) from oceanic sources and its oxidations in the atmosphere as described in Ghahreman et al. (2019), updated ozone dry deposition velocity over ice and snow (Gong et al., 2018; Helmig et al., 2007), a parameterized representation of iodide-mediated ozone deposition

220   on seawater based on Sarwar et al. (2015), an updated particle dry deposition scheme based on Emerson et al. (2020) from the original Zhang et al. (2001) scheme, and updated particle wet removal parameterization with consideration for the Wegener-Bergeron-Findeisen (WBF) process in mixed-phase clouds (Gong, W. et al., 2024).

For this study, the model's ADOM-II gas-phase chemical mechanism was extended to include bromine chemistry and a snowpack bromine source mechanism, based on Toyota et al. (2011), and was also adapted in the representation of odd nitrogen

225   chemistry. The bromine chemistry extension constitutes additional 26 reactions, including the heterogeneous aerosol surface reactions involving HOBr, $BrONO_2$ and HBr, for 7 inorganic bromine species (Br, BrO, Br_2, $BrNO_2$ and the three aforementioned species). One difference from the earlier study is the inclusion of the gas-phase association of Br and NO_2 to form $BrNO_2$ and its loss via photolysis and the reaction with Br (Burkholder et al., 2019; Orlando and Burkholder, 2000). In addition, the uptake coefficients on aerosol surfaces are revised for each of HOBr (Wachsmuth et al., 2002), $BrONO_2$ (Hanson

230   et al., 1996), and HBr (Schweitzer et al., 2000). The model representations of bromine source mechanisms in the Arctic will be described in the next section (2.1.3). The adaptation of odd nitrogen chemistry contains the following changes in the

ADOM-II mechanism: (1) introducing the photolytic decomposition of peroxyacetyl nitrate (PAN) and N_2O_5 neglected previously, and (2) replacing the kinetic representation for the hydrolysis of N_2O_5 into HNO_3 and of NO_2 into HONO and HNO_3 from binary gas-phase reactions with water vapor to heterogenous surface reactions on size-resolved aerosols simulated

235   online in GEM-MACH using uptake coefficients for N_2O_5 and NO_2 from McDuffie et al. (2018) and Jaeglé et al. (2018), respectively. The version 2.2.3 of the Kinetic PreProcessor (Sandu and Sander, 2006) was used to generate the Fontran90 source code from our revised set of chemical species and reactions to carry out the numerical integration of photochemical tendencies for the concentrations of chemical species. Actinic fluxes and photolysis rates are calculated online by the photolysis module JVAL (Sander et al., 2014) implemented in GEM-MACH.

240   The GEM-MACH pan-Arctic limited-area model (LAM) domain is set on a rotated latitude-longitude grid, at 0.1375° x 0.1375° (or ~ 15 km) horizontal resolution, covering the Arctic (>60°N) and extending to the southern US–Canada border (see Figure 1). Anthropogenic emissions used are based on a combination of North American emission inventories (specifically, the 2016 US National Emission Inventories, 2015 Canadian National Air Pollution Emission Inventories, and 2015 MEIT Canadian marine shipping emission inventories) and global ECLIPSE v6b 2015 baseline emissions. North American wildfire

245   emissions were processed using the Canadian Forest Fire Emission Prediction System (CFFEPS) from satellite-detected fire hotspot data (MODIS, AVHRR, and VIIRS). CFFEPS consists of a fire growth model, a fire emissions model, and a thermodynamic-based model to predict the vertical penetration height of a smoke plume from fire energy (see Chen et al., 2019, for details). For wildfires outside North America, the Fire INventory from NCAR (FINN; Wiedinmyer et al., 2011) v1.5 data was used, in which case the plume heights were estimated based on the global satellite retrieval statistics from Val Martin

250   et al. (2018). Biogenic emissions were calculated online in GEM-MACH based on the algorithm from BEIS version 3.7 with BELD4-format vegetation land cover for North America and GLC2000 global land cover for elsewhere. Modelled sea salt emissions were based on Gong et al. (2003). The 6-hourly chemical lateral boundary conditions were from the ECMWF Atmospheric Composition Reanalysis 4 (EAC4) (https://ads.atmosphere.copernicus.eu/cdsapp#!/dataset/cams-global-atmospheric-composition-forecasts?tab=form; Inness et al., 2019). The meteorology was initialized daily (at 00:00 UTC) using

255   the Canadian Meteorological Centre's global objective analyses, while the chemistry is continuous (i.e., the chemistry fields are cycled from the previous day integration).
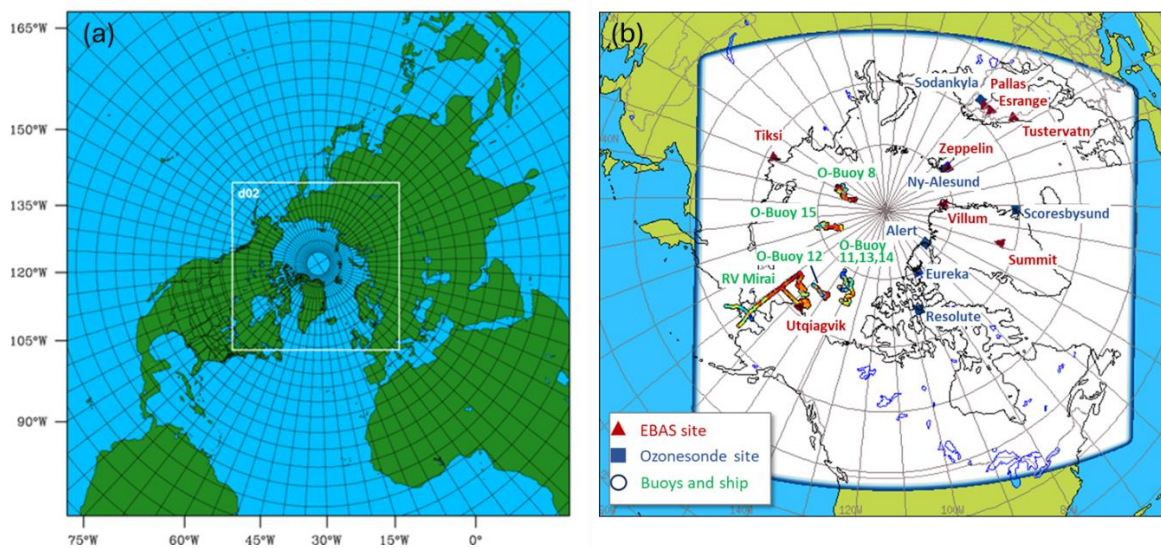
Figure 1. Model domain: (a) DEHM – northern hemispheric (75 x 75 km) and nested Arctic (25 x 25 km) domains; (b) GEM-MACH-Arctic domain (at 15-km resolution), along with surface and ozonesonde sites, as well as locations of buoys and ship observations used in this study.

2.1.3 Model representations of bromine source mechanisms in the Arctic

In the Arctic, the snowpack over sea ice and terrestrial surfaces near the coast serves as an extensive reservoir of bromide anions of seawater origin (Krnavek et al., 2012; Peterson et al., 2019; Simpson et al., 2005). Its exposure to gaseous oxidants and actinic radiation coming through the atmosphere is a main driver for the transformation of bromide to photoactive volatile forms such as Br_2 and BrCl (Oum et al., 1998; Foster et al., 2001; Adams et al., 2002; Pratt et al., 2013; Custard et al., 2017). While molecular diffusion perpetually mediates the mass transfer of gaseous reactants and products between porous snowpacks and ambient air, the rate of mass exchange is enhanced under windy conditions due to the reduced aerodynamic resistance in the surface boundary layer (Toyota et al., 2014), the pumping of air within the pore space of snowpacks (Albert and Shultz, 2002), and the lofting of bromide-containing ice grains detached from the surface of snowpacks into the ambient air (i.e., blowing snow) and aerosol particles formed as residues from the sublimation of the blowing snow (Jones et al., 2009; Yang et al., 2010).

For simulating springtime ODEs in the polar regions, the following two approaches have been adopted most commonly among chemical transport models (CTMs) so far: a snowpack-sourced mechanism, based on Toyota et al. (2011), and a blowing-snow sourced mechanism, based on Yang et al. (2010). Toyota et al. (2011) developed a semi-empirical parameterization to represent Br_2 emission from the surface snowpacks via autocatalytic bromine explosion arising from the dry deposition of HOBr and $BrONO_2$ produced in the ambient air (Lehrer et al., 2004) as well as via the net outcome of multiphase reactions within bromide-containing porous ice substrates exposed to O_3 and actinic radiation (e.g., Pratt et al., 2013). The bromine source strength modelled with this scheme is also influenced by the effectiveness of heterogeneous cycling of bromine species on atmospheric aerosols (Michalowski et al., 2000). This snowpack-sourced mechanism has been adopted and tested in several

280 CTMs (e.g., Falk and Sinnhuber, 2018; Marelle et al., 2021; Herrmann et al., 2021; Swanson et al., 2022; Zhai et al., 2023) with reasonable success in simulating springtime bromine explosion and ODEs in the Arctic and Antarctic boundary layer. Yang et al. (2008, 2010) proposed that salty snow lying on sea ice can be an important source for sea salt aerosols in the polar boundary layer during blowing snow events, which can subsequently release bromine contributing to the spring bromine explosion and ODEs. Using a physical parameterization for the sublimation of blowing snow combined with assumed snow

285 salinity levels based on available field data, this scheme estimates sea salt aerosol production and bromine release during blowing snow events. It was shown that by including bromine release from the sea salt aerosols during blowing snow events the model was able to simulate some of the bromine explosion events in polar regions during spring (Yang et al., 2010). This approach has also been incorporated and tested in a number of modelling studies (e.g., Huang and Jaeglé, 2017; Huang et al., 2020; Marelle et al., 2021; Swanson et al., 2022; Yang et al., 2020). Finally, we should add that Fernandez et al. (2019)

290 conceived a more empirical approach than those of Toyota et al. (2011) and Yang et al. (2008, 2010) for modelling the source terms of inorganic gaseous halogens on sea ice in their global chemistry-climate model. Unlike the Toyota et al. and Yang et al. models, this approach included the chemistry of chlorine and iodine along with that of bromine where the emissions of gaseous chlorine ($BrCl$ and Cl_2) and iodine (I_2) species from sea ice were also parameterized.

Representation of bromine source in GEM-MACH

295 In this study, GEM-MACH employs the snowpack-sourced bromine mechanism following Toyota et al. (2011) with a few minor adaptations. The production of reactive bromine Br_2 from snowpacks consists of two components: the production of Br_2 from deposited $HOBr$ and $BrONO_2$ on snowpacks reacting with bromide (Br^-) present and the production of Br_2 from O_3 mediated bromide oxidation in snow grain under sunlight (Pratt et al., 2013). The calculation of bromine flux upon the dry deposition of $HOBr$ and $BrONO_2$ on first-year (FY), multi-year (MY) sea ice and terrestrial surfaces (including over inland

300 water surfaces) follows exactly as in Toyota et al. (2011). As for the O_3-mediated Br_2 production from snowpacks, given the inadequate process-level understanding, Toyota et al. (2011) adopted a heuristic approach where a fraction of the dry deposition flux of O_3 was converted to the emission flux of Br_2 on the model snowpacks (or a molar yield Φ_1). The molar yield (Φ_1) was adjusted until a reasonable agreement was reached between the model and observations for the timing and magnitude of surface O_3 depletions and enhanced BrO vertical column densities (VCDs) across the high Arctic. In that study, Toyota et al. (2011)

305 selected Br_2 yields of 7.5% and 0.1% from the O_3 loss via dry deposition for solar zenith angles not greater than 85 degrees (sunlit condition) and greater than 85 degrees (dark condition) over snowpacks on FY sea ice only. In the current study, greater Br_2 yields from O_3 deposition on sea ice were selected, namely, 15.0% and 1.0% for sunlit and dark conditions, respectively, over FY sea ice. The higher yields were selected primarily to compensate for the potential underrepresentation of heterogeneous cycling of bromine on aerosol surfaces due to the model underprediction of Arctic haze aerosols (see Gong et

310 al., 2024). In addition, non-zero Br_2 yields from O_3 deposition over MY sea ice (half of the yields over FY sea ice) were used in this study. Krnavek et al. (2012) found bromide presence in snow samples collected from both FY and MY sea ice over the Arctic Ocean off Alaska (albeit with large variability in bromide content). Peterson et al. (2019) measured concentrations of

chloride, bromide, and sodium in snow samples collected during polar spring over MY and FY sea ice north of Greenland, Alaska, as well as over central Arctic Ocean, and found that surface snow over MY sea ice regions was more often depleted

315 of bromide indicating that it may have served as a source of bromine to the atmosphere. Swanson et al. (2022) further made an assumption that all snow has a uniform ability to produce molecular bromine, effectively assuming an infinite bromide reservoir with Br_2 production limited only by the deposition flux in the implementation of the snowpack bromine source mechanism of Toyota et al. (2011). The uncertainty in the parameter selections for the snowpack bromine source mechanism will be discussed later in section 4.1.

320 Other adaptations from Toyota et al. (2011) in the parameterization of the snowpack Br_2 production for this study include: (1) raising the temperature threshold to permit the snowpack Br_2 production to 272.15 K (Oum et al., 1998), (2) assuming the deactivation (without possibility for reactivation afterwards) of the snowpack's ability to form Br_2 after a snowmelt event diagnosed by the continuous occurrence over 6 hours of surface air temperature at 273.15 K or higher (Burd et al., 2017) and (3) setting the minimum snow depth at 5 cm to permit the Br_2 production from snowpacks (e.g., Swanson et al., 2022).

325 For discriminating the age of sea ice between FY and MY, the EASE-Grid Sea Ice Age Version 4 dataset (https://nsidc.org/data/nsidc-0611/versions/4), available from the National Snow and Ice Data Center at a weekly temporal resolution and a spatial resolution of 12.5 km × 12.5 km (Tschudi et al., 2020), was used. Daily total (FY + MY) sea ice concentrations are obtained from the Canadian Global Ice Ocean Prediction System data (Smith et al., 2016), which are used also as surface boundary conditions for our host meteorological model simulation. Since the EASE-Grid Sea Ice Age data do

330 not cover areas near the coastlines and within narrow channels of the sea, we fill in the data gaps by using a monthly climatology of sea ice thickness, taken again from the surface boundary condition data for the host meteorological model simulation, as a proxy for the age of sea ice. Here, MY sea ice is assumed where the climatological sea ice thickness for the meteorological model input is greater than 3.5 m. The monthly mean sea ice age used by the GEM-MACH simulation is shown in the supplementary material (SF.1)

335 ***Representation of bromine sources in DEHM***

DEHM includes the representation of bromine release from open ocean sea salt and the blowing-snow sea salt following Yang et al. (2008, 2010, 2020). The release of bromine from sea salt aerosols is thought to involve the heterogeneous uptake of gaseous inorganic bromine on sea salt aerosols and subsequent reaction with bromide (Fan and Jacob, 1992; Yang et al., 2005). Given that the details of the bromine release mechanisms are not completely known, Yang et al. (2005, 2008, 2010) proposed

340 a parameterization to estimate bromine release flux from sea salt aerosols, $E_{Br2}(SSA)$, based on sea salt flux, which can be either from open ocean (*OO*) or blowing snow (*BLSN*) production, the Br/NaCl mass ratio (R_a), and a bromine depletion factor (*DF*):

$$E_{Br2}(SSA) = R_a \times E_{SSA}(OO, BLSN) \times DF$$

For open ocean sea salt production, two different source functions are used: for the sea salt aerosols with dry diameters less

345 than 1.25 µm a source function based on Mårtensson et al. (2003) is used, while for those with sizes greater than 1.25 µm the source function of Monahan et al. (1986) is applied (see Soares et al., 2016 for details).

For blowing-snow production of sea salt, Yang et al. (2008, 2010) made use of a blowing snow sublimation rate, which is a complex function of wind speed (at 10m), air temperature, relative humidity, snow age, etc. For this study, the size dependent salinity of snow in Yang et al. (2008) was scaled to a mean salinity for the Arctic of 0.93 psu for snow on FY sea ice, which

350 is 3 times the Antarctic mean salinity of 0.31 psu as given in Frey et al. (2020), and the salinity of the snow on MY sea ice was assumed to be half of that on FY sea ice. It was assumed that a single sea salt particle is produced per snowflake as in Yang et al. (2008 and 2010). Monthly bromine depletion factors (DF) for the Northern Hemisphere from Yang et al. (2020) were used to estimate the bromine release from blowing snow sea salt.

2.2 Observations used in this study

355 Ozone observations from multiple platforms were used for comparison with model simulations in this study, including surface O_3 observations from 8 Arctic ground sites, 7 buoys and a research vessel over the Arctic Ocean, as well as O_3 vertical profile observations from ozonesondes and research aircraft. In addition, observations of bromine monoxide (BrO) vertical column density (VCD) obtained from multiple axis differential optical absorption spectroscopy (MAX-DOAS) measurements were also used to compare with model results. Table 1 lists all the sites and observational data used in this study.

360 **Table 1. Site and observational data used in this study (latitudes are given in degrees north; longitudes are in degrees east (E) or west (W); altitudes are given in meters above mean sea level, masl).**

Site/platform	Location (lat, lon, elev)	Data coverage	Data source
Ground sites (O_3, met)			
Utqiaġvik	(71.3N, 156.6W, 11.0)	Full year 2015	EBAS (https://ebas-data.nilu.no/Default.aspx)
Villum	(81.58N, 16.64W, 31.0)	10 months in 2015 (missing Jan – Feb 2015)	
Tiksi	(71.6N, 128.9E, 8.0)	11 months in 2015 (missing Dec 2015)	
Zeppelin	(78.9N, 11.9E, 474.0)	Full year 2015	
Pallas	(67.97N, 24.12E, 565.0)	Full year 2015	
Esrange	(67.88N, 21.07E, 475.0)	Full year 2015	
Tustervatn	(65.83N, 13.92E, 439.0)	11 months in 2015 (missing Feb 2015)	
Summit	(72.58N, 38.48W, 3238.0)	8 months in 2015 (missing mid July – late Oct 2015)	
Buoys (O_3)			
O-buoy 8	East Siberian Sea	2015-09-05 to 2016-02-14[†]	TOAR-II Ozone over the Ocean Focus Working Group database (Kanaya et al., 2024); original data source:
O-buoy 11	Beaufort Sea	2014-10-07 to 2015-08-27	
O-buoy 12	Beaufort Sea	2014-10-11 to 2015-04-18	
O-buoy 13	Beaufort Sea	2015-09-28 to 2016-04-28	

O-buoy 14	Beaufort Sea	2015-10-01 to 2017-09-30	https://doi.org/10.18739/A2WD4W (Simpson et al., 2009)
O-buoy 15	East Siberian Sea	2015-09-12 to 2016-02-22	
Ship (O$_3$)			
R/V Mirai	Bering Strait & Chukchi Sea	2015-09-04 to 2015-10-05‡	TOAR-II Ozone over the Ocean Focus Working Group database (Kanaya et al., 2024); original data source: https://www.godac.jamstec.go.jp/darwin_cruise/view/metadata?key=MR15-03_leg1&lang=en
Ozonesondes			
Alert	(82.49N, 62.34W, 66.0)	Weekly to bi-weekly launches (no launches in Jan and Dec 2015)	TOAR-II/HEGIFTOM database (https://hegiftom.meteo.be/datasets/ozonesondes) (Van Malderen et al., 2024)
Eureka	(79.98N, 85.93W, 10.0)	Weekly, with additional launches in March (no launches in June 2015)	
Resolute	(74.70N, 94.96W, 64.0)	Mostly weekly launches (no launches in June 2015)	
Ny-Ålesund	(78.92N, 11.92E, 11.0)	Weekly launches (additional launches during Jan – March and Nov – Dec 2015)	
Scoresbysund	(70.48N, 21.97W, 68.0)	Mostly weekly launches (reduced launches in Aug and Sept 2015)	
Sodankylä	(67.37N, 26.65E, 179.0)	Mostly weekly launches	
Aircraft			
NETCARE (AWI/Polar 6)	Canadian Arctic Archipelago	9 research flights, 2015-04-07 to 2015-04-13	TOAR-II Ozone over the Ocean Focus Working Group database (Kanaya et al., 2024); original data source: Government of Canada Open Data portal (https://open.canada.ca/data/en/dataset, last access: 2024-07-31)
MAX-DOAS (BrO)			
O-buoy 10	Beaufort Sea	2015-04-21 to 2015-06-10	NSF Arctic Data Center (https://arcticdata.io/catalog/view/doi:10.18739/A2XD0QZ0X, https://arcticdata.io/catalog/view/doi:10.18739/A2X921K6B, https://arcticdata.io/catalog/view/doi:10.18739/A2SJ19S3P, last access: 2017-01-05)
O-buoy 11	Beaufort Sea	2015-04-21 to 2015-06-10	
O-Buoy 12	Beaufort Sea	2015-04-21 to 2015-05-22	
BARC	(71.3N, 156.7W)	2015-02-21 to 2015-06-10	NSF Arctic Data Center (https://arcticdata.io/catalog/view/doi:10.18739/A29882N5H, last access: 2023-11-24)

† Dates shown are the start and end date of deployment for each of the O-buoys. Note, however, O_3 measurements were not always available for the full deployment period, and only the data within 2015 was used in this study. Also note that the end date of the deployment for O-buoy 14 was not available but the buoy was active beyond the end of 2015.

365   ‡ This is the period when RV Mirai was north of 60°N.

2.2.1 Arctic ground sites

Hourly O_3 mixing ratio data for the year 2015 from 8 long-term ground-based monitoring sites in the Arctic were obtained from the EBAS database infrastructure (https://ebas.nilu.no) hosted by NILU, which handles data submitted to AMAP (Arctic Monitoring Assessment Programme), EMEP (European Monitoring Evaluation Programme), and GAW-WDCRG (Global

370   Atmosphere Watch – World Data Centre for Reactive Gases). These are the only ground sites with available O_3 observations in 2015. The 8 sites (marked on Fig. 1) include 3 coastal sites (Utqiaġvik, Villum, Tiksi), a coastal mountain site (Zeppelin), 3 inland sites (Pallas, Esrange, and Tustervatn), and a high-elevation site (Summit) on Greenland plateau. Surface O_3 measurements at these monitoring stations are all undertaken using a UV-absorption based instrumentation.

The Utqiaġvik site (71.3°N, 156.6°W, 11.0 m ASL), the NOAA Global Monitoring Laboratory's Barrow Atmospheric Baseline

375   Observatory, is located on the northernmost shore of Alaska, about 8 km northeast of the community of Utqiaġvik (formerly Barrow) and 3 km away from the Arctic Ocean. The site, with its east-northeasterly prevailing winds off the Beaufort Sea, is characterized as having an Arctic maritime climate affected by variations of weather and sea ice conditions in the Central Arctic. Villum Research Station (Villum) is in northeast Greenland (81.58° N, 16.64° W, 31.0 m ASL) on a small Peninsula of 20 x 15 km on lowland plain and 750 m from the coast, at the military outpost Station Nord. The sea around the peninsula

380   is frozen about 11 months of the year. Tiksi (Tiksi International Hydrometeorological Observatory) is located in northern Siberia (71.6°N, 128.9°E, 8.0 m ASL) on the shore of Laptev Sea (Uttal et al., 2013, 2016). The Zeppelin station is located on the top of Zeppelin Mountain (78.9°N, 11.9°E, 474.0 m ASL) on Spitsbergen in the Svalbard archipelago, surrounded by glaciers, mountains, and the sea. Due to its location, for most of the time the station is above the local inversion layer and hence not impacted by local emissions (Platt et al., 2022).

385   The 3 inland sites are all located in the European subarctic boreal forest region close to the Arctic circle. The Pallas site (67.97°N, 24.12°E, 565.0 m ASL) is located in the Pallas-Yllästunturi National Park on top of a fjeld. The site is part of the Pallas Global Atmospheric Watch (GAW) station operated by the Finnish Meteorological Institute (Hatakka et al., 2003). The Esrange site (67.88°N, 21.07°E, 475.0 m ASL), at similar latitude to the Pallas site but on the Swedish side, is part of the EMEP monitoring network. Tustervatn (65.83°N, 13.92°E, 439 m ASL) located in Northern Norway just south of the Arctic

390   circle is also an EMEP regional monitoring site. The high-elevation site Summit (72.58°N, 38.48°W, 3238.0 m ASL), operated by the National Science Foundation (NSF) and the NOAA Global Monitoring Laboratory, is located at the top of the Greenland Ice Sheet. Given its geographical location and high elevation, measurements at this site are particularly influenced by free troposphere long-range transport to the Arctic.

2.2.2 Surface mobile platforms (ship and buoys)

395 Surface O_3 observations from mobile platforms were used to compare with model simulations. Hourly data were obtained from the Tropospheric Ozone Assessment Report – Phase Two (TOAR-II) Ozone Over the Ocean Focus Working Group database (Kanaya et al., 2024), including from the O-Buoy Project (Simpson et al., 2009; https://arcticdata.io/catalog/view/doi%3A10.18739%2FA2WD4W) and the R/V Mirai cruise (Kanaya et al., 2019).

As part of the Arctic Observing Network program, a series of autonomous ice-tethered buoy systems (O-buoys) capable of
400 year-round measurement of O_3, CO_2, and BrO were deployed over the Arctic Ocean during 2011 – 2016 (Knepp et al., 2010; Halfacre et al., 2014; Burd et al., 2017). O_3 measurements were available from 6 O-buoys during 2015; they are listed in Table 1 with their deployment dates and the areas of deployment (also see Figure 1 for their tracks). The time and duration of the O_3 measurement varied between these buoys, e.g., O-buoy 11 and 12 covered the first half of 2015 while O-buoy 8, 13, 14, and 15 covered the latter half (starting in September). In all, the O-buoy O_3 measurement coverage extends nearly the full year of
405 2015 (with a gap in August), although measurements over the winter months (Jan, Feb, Nov, and Dec) were sparse.

In addition to buoy measurements, O_3 measurement (using a UV-absorption instrument) onboard the R/V Mirai of the Japan Agency for Marine–Earth Science and Technology (JAMSTEC) was available from its Arctic cruise in 2015 (MR15-03; Kanaya et al., 2019). MR15-03 took place in the fall of 2015. The cruise started from Mutsu, Japan in late August, sailing through North Pacific, Bering Strait, Chukchi Sea, and around northern coast of Alaska to Utqiaġvik, and then back through
410 Bering Strait and ended at Dutch Harbour, Alaska in early October. During the month of September 2015, the R/V Mirai was north of 60°N in Arctic waters (See Fig. 1 for R/V Mirai's track in the Arctic).

2.2.3 Ozonesondes

Ozonesonde data from six Arctic sites (Alert, Eureka, Resolute, Ny Ålesund, Scoresbysund and Sodankylä) were used to evaluate the modelled seasonal variations of O_3 between 0 and 5 km ASL (Fig.1 and Table 1). Alert (82.49°N, 62.34°W) is
415 located on the northeastern shore of Ellesmere Island, the northernmost island of the Canadian Arctic Archipelago (CAA), facing the vast area of perennial sea ice on the Arctic Ocean. Eureka (79.98°N, 85.93°W) is located on the coast of an inlet of the Arctic Ocean along Nansen and Eureka Sounds penetrating over 200 km inland from the northwestern coast of Ellesmere Island. Resolute (74.70°N, 94.96°W) is located on the southern shore of Cornwallis Island in the central part of the CAA. Alert, Eureka and Resolute are located where arriving air masses may have experienced prolonged contact with sea ice on the
420 Arctic Ocean and within the CAA. Ny Ålesund (78.92°N, 11.92°E) is located on the northwestern shore of the bay of Kongsfjord on Spitsbergen, Svalbard, a Norwegian archipelago in the marginal ice zone of the Arctic Ocean. The launch site is situated at the foot of the Zeppelin Mountain, the site of the Zeppelin station. Scoresbysund (70.48°N, 21.95°W) is located on the eastern shore of Greenland along a deep inlet of the Greenland Sea. Sodankylä (67.36°N, 26.62°E) is in the boreal forest region of northern Finland and is the only site located inland amongst the six ozonesonde sites selected for this study. The
425 ozonesondes were launched mostly on a weekly schedule at these sites with some variations as noted in Table 1. The

homogenized ozonesonde time series data was obtained from the TOAR-II Harmonization and Evaluation of Ground Based Instruments for Free Tropospheric Ozone Measurements (HEGIFTOM) project (Van Malderen et al., 2024; https://hegiftom.meteo.be/datasets/ozonesondes).

2.2.4 Aircraft data (2015 NETCARE-Polar6)

430 During the 2015 spring field campaign of NETCARE project (Network on Climate and Aerosols: Addressing Key Uncertainties in Remote Canadian Environments; Abbatt et al., 2019), airborne measurements were conducted with the Polar 6 aircraft, a Basler BT-67 (converted DC-3) owned and operated by the Alfred Wegener Institute (Aliabadi et al., 2016; Leaitch et al., 2016). O_3 mixing ratios were measured through UV photometry with a Thermo Scientific 49i analyzer (time resolution 10 s, ±0.2 ppbv). Supporting meteorological parameters were provided by an AIMMS-20 package (Aventech Research Inc.,

435 Canada). All data from NETCARE are available on the Government of Canada Open Data Portal (https://open.canada.ca/data/en/dataset, last access: 2024-07-31). Nine research flights were conducted around Ellesmere Island in the Canadian Arctic Archipelago between April 7 and 13, 2015, including profiling through the lowest 6 km of the atmosphere (Bozem et al., 2019). As shown later in section 4.1, many of these profiling flights captured ODEs prevalent at the time in the area.

440 ### 2.2.5 MAX-DOAS BrO VCD data

To evaluate modelled bromine chemistry in the Arctic, measurements of bromine monoxide (BrO) vertical column densities (VCDs) using multiple-axis differential optical absorption spectroscopy (MAX-DOAS) from several platforms were obtained from a repository at the NSF Arctic Data Center (https://arcticdata.io/, see Table 1). MAX-DOAS instruments were mounted on the aforementioned O-buoys deployed onto the Arctic Ocean (Swanson et al., 2020). The MAX-DOAS BrO measurements

445 on O-buoys were only available during spring after Polar sunrise and when enough O-Buoy solar power was gained to defrost the MAX-DOAS view port (usually some time in April), until summer when most of the O-Buoys were destroyed from being crushed between ice fragments on the Arctic Ocean (Swanson et al., 2022). During 2015, BrO measurements were available from O-buoy 11 and 12, as well as O-buoy 10 (Table 1). BrO measurements were also available from a MAX-DOAS instrument of the same type (as those installed on O-buoys) deployed at the Barrow Arctic Research Center (BARC) (Simpson,

450 2018; Simpson et al., 2017). The MAX-DOAS at BARC was able to operate much earlier in the year than those on the O-buoys as it was powered by local utilities and was able to defrost the MAX-DOAS viewport much earlier (Table 1).

3 Model simulations and comparison with observations

3.1 Seasonal distribution of lower tropospheric O_3 in the Arctic

Arctic lower tropospheric O_3 is influenced by transport from lower latitudes, photochemical production from anthropogenic

455 and biogenic ozone precursors of both local and distant origins, atmospheric removal processes (such as dry deposition and

(photo-)chemical loss through reactions with biogenic VOCs and surface sourced reactive halogens), as well as stratospheric-tropospheric exchange. All of these sources and processes, which are represented in the models in this study at various degree of complexity (see Section 2 above), vary seasonally which gives rise to the seasonal variations of Arctic O_3. Figure 2 shows the model simulated monthly mean O_3 concentrations over the Arctic for January, April, July, and October (representative for each of four seasons) at three model levels, the lowest (surface level), near 900 hPa, and near 700 hPa (GEM-MACH simulation shown in Fig. 2(a) and DEHM simulation in Fig. 2(b)). The GEM-MACH model simulated O_3 over the Arctic shows distinctively different seasonal patterns near the surface and aloft and between the central Arctic Ocean and subarctic regions. Over the central and western Arctic Ocean (Eurasian and North American side) close to the surface, this model computes the lowest O_3 in spring as a result of the O_3 depletion events (ODEs) from the prevalence of bromine explosions during this period, in broad agreement with an earlier report of a full-year of surface ozone measurements over the central Arctic Ocean (Bottenheim et al., 2009); the highest ozone from the GEM-MACH simulation is found in fall (October). In contrast, at higher altitudes, O_3 is highest in springtime; the same is also true for the inland subarctic regions. The springtime ozone maximum is thought to be driven by transport from the stratosphere, since intrusion events are more frequent during this season, and by photochemical production from the NO_x released from thermal decomposition of PAN (Walker et al., 2012). The model-simulated O_3 over subarctic boreal regions also displays a spring maximum; the model-simulated low O_3 over summer in these regions can be attributed to both the loss through O_3 reactions with biogenic VOCs (e.g., isoprene) under low NO_x conditions and enhanced dry deposition. The DEHM-simulated O_3 over the Arctic does not show a clear springtime minimum at the lowest model level; the model simulation shows a general spring maximum over the Arctic throughout the lower troposphere except for over the very centre of the Arctic Ocean (> 80°N) where the modelled (April) monthly mean O_3 concentration is slightly lower than surrounding areas at the lowest model level. The DEHM-simulated monthly mean O_3 for July shows clear enhancement at elevated levels (particularly at the near 900 hPa level) over northern Alaska and Chukchi Sea, extending into central Arctic Ocean, which is likely contributed by boreal wildfires (see discussions later in Section 4.2). Except near the surface and during spring, the two models are quite consistent in simulating O_3 over the Arctic particularly during winter (January) and fall (October); the two models also behaved similarly in simulating O_3 at higher altitude (e.g., near the 700 mb level). Both model simulations show low O_3 over subarctic boreal regions in summer, but the low O_3 simulated in GEM-MACH extends to a deeper layer compared to the DEHM simulation. The DEHM-simulated surface O_3 concentrations over the Arctic Ocean during summer are higher than those in the GEM-MACH simulation, which may partly be a result of the higher springtime O_3 concentrations simulated in DEHM.
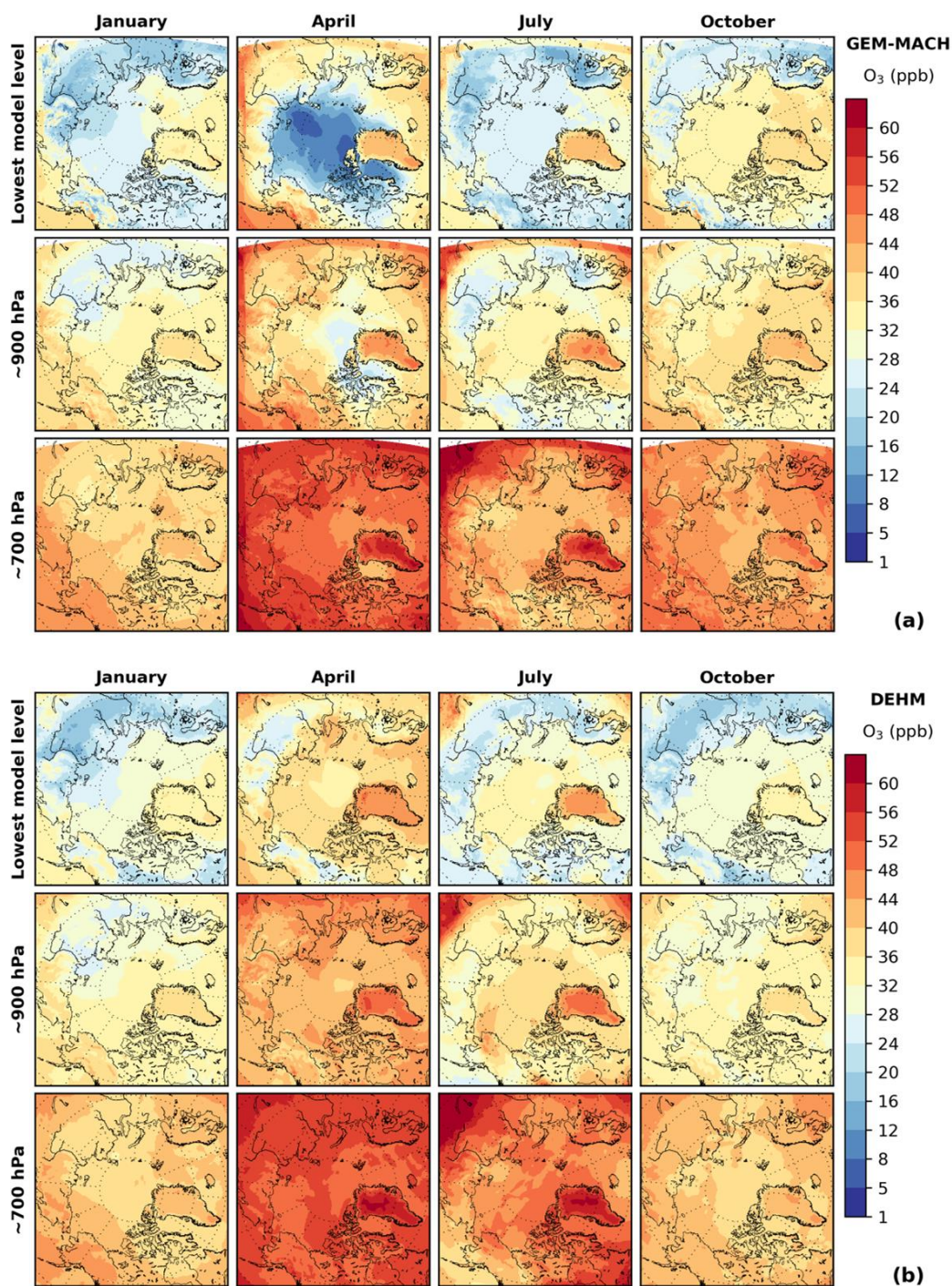
Figure 3 shows the spatial distribution of the times when the annual maximum and minimum monthly mean O_3 concentrations
490   occur at the three model levels seen in Figure 2 (left panels from the GEM-MACH simulation; right panels from the DEHM
simulation). At the 700 hPa level, the two models are consistent in showing that the annual O_3 maximum occurs in spring
months (April and May) over the Arctic while the annual O_3 minimum occurs in winter (December and January) and late fall
(November), with the exception over the Beaufort Sea and the Canadian Northwest Territories where the GEM-MACH-
simulated annual O_3 minimum occurs in late summer months (July and August). Near the surface, the two models differ over
495   the Arctic Ocean stemming from the model's differing ability to simulate the springtime ODEs which are prevalent over the
Arctic Ocean sea ice (Bottenheim et al., 2009); the GEM-MACH simulation shows annual minimum monthly O_3 in spring
months (April and May), due to modelled strong ODEs (see discussion later in Sections 3.2 and 4.1), and maximum in fall
(October), while the DEHM model simulates annual maximum monthly O_3 in spring over the Arctic (much like the upper
levels) due to considerably fewer ODEs simulated by the model (see Sections 3.2 and 4.1). It is evident that the springtime O_3
500   depletion process plays a central role in driving the O_3 seasonal cycle at low levels over the High Arctic in the GEM-MACH
simulation. Away from the Arctic Ocean and the Canadian Archipelago overland, the two models are again consistent in
producing an annual maximum O_3 in spring and minimum O_3 in late summer and early fall over Alaska, Northwest Territories,
and eastern Russian Arctic.
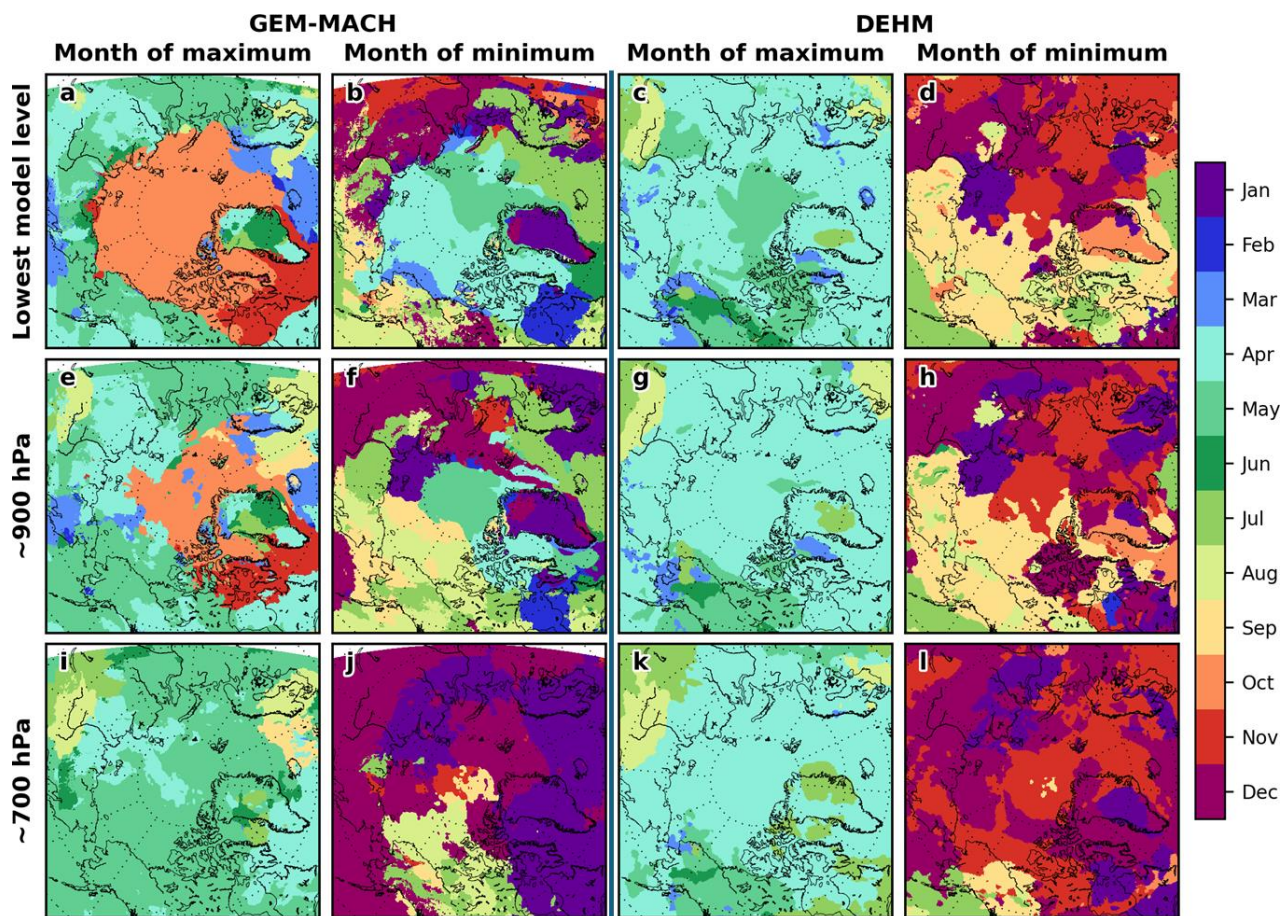
Figure 3. Timing of modelled annual maximum and minimum monthly mean O₃ concentration at the three model levels as in Figure 2: GEM-MACH – left panels (a, b, e, f, i, j); DEHM – right panels (c, d, g, h, k, l).

3.2 Annual O₃ time series comparison with observations

To evaluate the models' ability to simulate Arctic boundary layer O₃, the modelled surface (or lowest model level) O₃ concentrations are compared with observations from ground-based monitoring sites and surface mobile platforms (O-Buoys and Mirai cruise). To do this, the modelled O₃ concentrations are extracted at the ground-based sites and following buoy tracks and ship paths from the nearest model grid cells and hours and compared with hourly observations. Existing model evaluations related to tropospheric ozone assessment (e.g., Monks et al., 2015; Whaley et al., 2023; Young et al., 2018) have been mostly performed on long-term annual and monthly averages. With the two regional models used in this study run at much higher spatial resolutions, as compared to the global models involved in the previous assessment studies, we can examine model simulations and compare with observations at much finer temporal resolutions (e.g., hourly) here. Figure 4 shows the O₃ time series comparisons at the eight Arctic monitoring sites described in 2.2.1. Overall, both DEHM and GEM-MACH simulations captured the observed O₃ seasonal as well as synoptic-scale variations at these Arctic ground sites. The three Arctic coastal

sites, Utqiagvik, Villum, and Tiksi, are strongly influenced by the spring ODEs, which are captured reasonably well by the GEM-MACH simulation. The DEHM model was less successful in capturing the springtime ODEs at these sites. The modelling of ODEs will be examined in more details later in section 4.1. The seasonal variation in the observed O_3 at the subarctic inland sites (Tustervatn, Pallas, and Esrange) follows the typical pattern of a maximum in spring and minimum in summer, with greater variability in summer and fall. The model simulations from both DEHM and GEM-MACH follow closely the observed O_3 variations throughout the year. The GEM-MACH simulation has a larger low bias at the two northern European boreal sites (Pallas and Esrange) particularly during the spring and summer seasons, while the DEHM performed better (particularly at Esrange; see statistical evaluation below: Table 2, SF.2 and 3). This may be partly attributable to the difference in modelled O_3 dry deposition velocity over the boreal landcover between GEM-MACH and DEHM. Clifton et al. (2023) examined O_3 dry deposition velocity formulations across contemporary regional chemical transport models, including the formulations used in GEM-MACH (based on Wesely, 1989) and DEHM (as in Simpson et al., 2012). They showed that the formulation used in GEM-MACH ("GEM-MACH Wesely") significantly overestimated O_3 dry deposition velocity over the European boreal forest during summer compared to an estimate based on ozone flux measurements. In contrast, the formulation used in DEHM ("DO$_3$SE") was shown to produce O_3 dry deposition velocities in much closer agreement with those derived from observations over the European boreal forest in summertime. In addition, the biogenic emission inventory system (BEIS; see https://www.epa.gov/air-emissions-modeling/biogenic-emission-inventory-system-beis) used by GEM-MACH for estimating biogenic emissions was developed primarily for North America. The recent update to BEIS v3.7 and BELD4 North American vegetation data in GEM-MACH led to a reduction in modelled isoprene and increased O_3 over the North American boreal region in summertime, as the biogenic isoprene contributes to O_3 loss under low NO_x conditions (Gong et al., 2022). However, there is still uncertainty in GEM-MACH modelled biogenic emissions over the European boreal region, which may also be contributing to the low O_3 bias. The two high-elevation sites (Zeppelin and Summit) exhibit somewhat different O_3 seasonal patterns. The Zeppelin site, situated at 474 m above the Arctic Ocean, is situated approximately half of the time above the top of the atmospheric boundary layer (Dekhtyareva et al., 2018). The observed O_3 time series in 2015 displays an overall maximum in April and a minimum in July, in contrast to the Arctic coastal sites. This is consistent with the seasonal patterns based on a longer time (multi-year) observations (e.g., Whaley et al., 2023). However, it is evident from the time series in Fig. 4 that the site is sporadically impacted by springtime ODEs during April and May in 2015. Previous observations of ODEs at this site have been reported by others (e.g., Berg et al., 2003; Eneroth et al., 2007; Lehrer et al., 1997; Solberg et al., 1996). The O_3 observation at Summit has a gap between the end of July and the end of October in 2015. The incomplete observed O_3 time series shows no clear trend over the first 5 months (January – May) of 2015 before increasing over June to reach a maximum in July. This is a departure from the seasonal trend shown in Whaley et al. (2023) based on multi-year data (2003 – 2018), which showed a maximum in May. Both Zeppelin and Summit surface observations show high O_3 events in July 2015. As will be discussed later in 4.2, there is an indication that these events may be associated with transport of wildfire plumes in the free troposphere. Again, model simulations from both DEHM and GEM-MACH compare well with

the observations at these sites, though neither model simulations was able to fully capture the July high O$_3$ events observed at Summit.
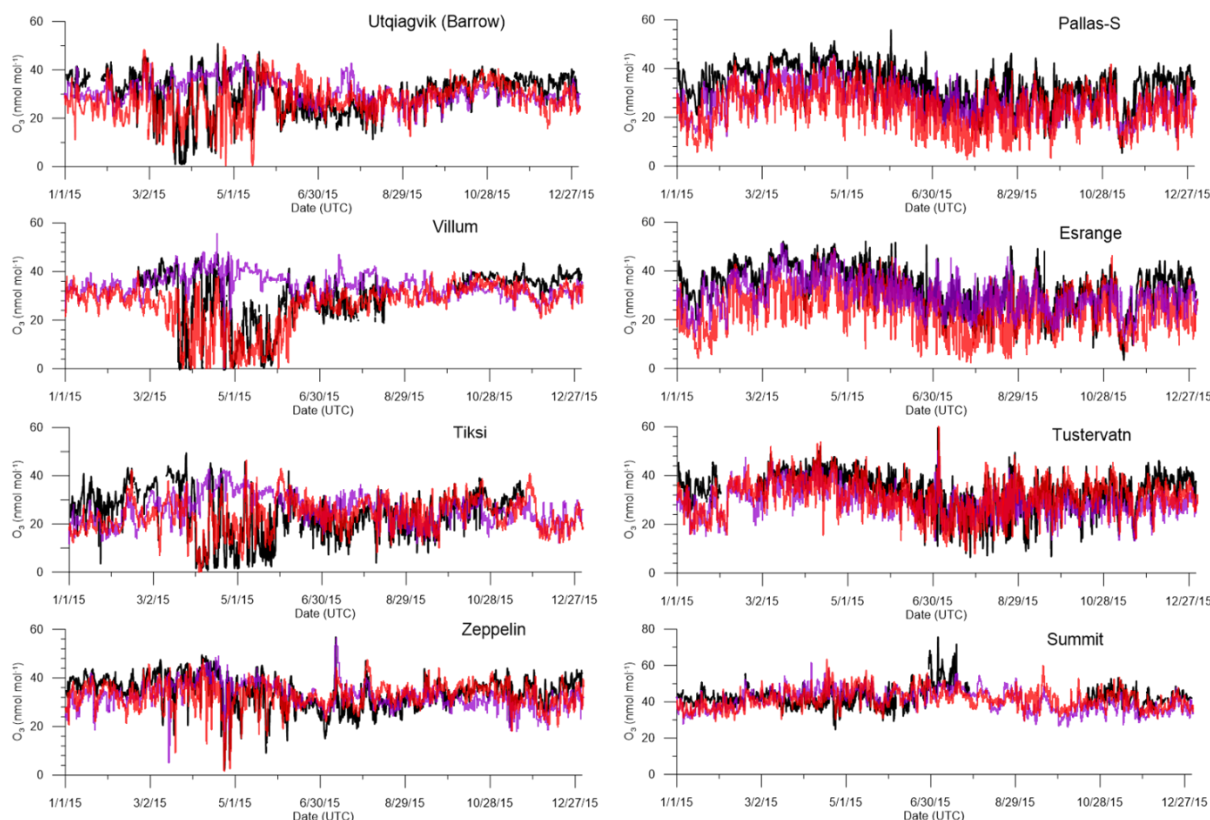
Figure 4. Observed and modelled 2015 annual surface ozone time series at selected Arctic sites: observation – black line, DEHM – magenta line, GEM-MACH – red line.

Statistical evaluations were conducted on the hourly time series. Table 2 shows selected seasonal and annual model performance scores at the 8 Arctic ground sites, including normalised mean bias (NMB), Pearson correlation coefficient (r), and unbiased root-mean-square-error (URMSE), while the corresponding monthly scores are shown in SF.2. The seasonal scatter plots (colour coded for each month separately) of model vs. observations at the 8 surface sites are shown in SF.3. The evaluation (Table 2) shows that both models underpredict wintertime Arctic surface ozone at all sites, with GEM-MACH having a greater negative bias at Utqiagvik, Villum, Pallas and Esrange. At coastal sites, the DEHM model has significant positive bias during the spring months due to its under-representation of the springtime ODEs, while the GEM-MACH model has considerably better performance scores. It is interesting to note the significant positive bias in both models during the summer months at the coastal sites, except for a small negative bias in GEM-MACH at Villum, which is largely driven by the month of June values; see SF.3(b). Neither DEHM nor GEM-MACH currently includes iodine chemistry, which can play a prominent role in ozone destruction over polar oceans during (as well as after) the time of springtime bromine explosions (Benavent et al., 2022; Fernandez et al., 2024; Mahajan et al., 2010; Wittrock et al., 2000). At the two northern European

boreal sites, Pallas and Esrange, the models are generally biased low throughout the year. GEM-MACH has the most difficulty

570   in simulating surface ozone accurately at these two sites as evident by the relatively poor performance scores shown in Table

2 (and SF.3) compared to other sites, while DEHM performed considerably better at these sites. As discussed earlier, the larger

low bias in GEM-MACH simulated surface ozone over the northern European boreal region is attributable, in part, to the

probable overprediction of ozone dry deposition in this region (most pronounced during summer). Overall, the two regional

models seem to demonstrate better skill in capturing the observed seasonal variations in the Arctic surface ozone, compared

575   to the large-scale global atmospheric chemistry models reported in previous assessments (e.g., Law et al., 2023; Whaley et al.,

2023; Young et al., 2018), which can be attributed, at least in part, to better resolved atmospheric dynamics and boundary layer

processes modelled at finer spatial and temporal scales.

Table 2. Selected seasonal and annual model performance scores (NMB, r, and URMSE) based on hourly time series at the 8 Arctic ground sites.

		NMB* (%)					r†					URMSE (ppbv)‡				
		DJF	MAM	JJA	SON	Annual	DJF	MAM	JJA	SON	Annual	DJF	MAM	JJA	SON	Annual
Utqiagvik	DEHM	-14.92	27.22	20.17	-12.37	**2.83**	0.62	0.03	0.21	0.75	**0.09**	3.30	12.09	5.86	3.40	**9.09**
	G-M	-23.90	-12.50	11.90	-5.12	**-5.89**	0.81	0.65	0.76	0.59	**0.69**	3.03	8.61	2.87	2.71	**4.42**
Villum	DEHM	-16.05	66.64	22.21	-12.84	**17.80**	0.58	0.32	0.29	0.49	**-0.09**	2.90	14.24	5.32	2.29	**12.5**
	G-M	-22.70	-36.00	-4.05	-9.44	**-18.00**	0.77	0.46	0.37	0.55	**0.48**	2.72	9.25	4.27	2.17	**5.29**
Tiksi	DEHM	-30.44	44.15	22.73	-10.43	**7.25**	0.63	-0.38	0.43	0.62	**-0.18**	4.26	16.72	5.16	4.70	**12.3**
	G-M	-30.90	6.85	16.50	-1.95	**0.22**	0.70	0.79	0.70	0.64	**0.71**	2.96	5.91	2.95	3.35	**3.87**
Zeppelin	DEHM	-16.48	4.27	11.16	-10.93	**-3.61**	0.70	0.52	0.45	0.45	**0.41**	3.04	7.17	5.15	3.81	**6.31**
	G-M	-13.20	-9.71	11.30	-2.65	**-1.53**	0.91	0.77	0.69	0.65	**0.73**	1.73	4.34	2.98	2.12	**3.10**
Pallas	DEHM	-26.66	-17.51	-14.58	-18.04	**-19.30**	0.82	0.52	0.55	0.73	**0.74**	3.42	5.08	5.62	4.75	**5.16**
	G-M	-35.00	-25.60	-34.20	-20.00	**-28.10**	0.66	0.56	0.35	0.61	**0.53**	3.96	4.24	5.15	4.94	**4.63**
Esrange	DEHM	-19.33	-9.36	-0.12	-5.28	**-9.13**	0.82	0.64	0.70	0.70	**0.76**	3.54	4.78	4.88	5.73	**5.45**
	G-M	-36.30	-24.80	-29.00	-18.30	**-27.10**	0.62	0.51	0.44	0.57	**0.53**	3.99	4.57	5.51	5.94	**5.00**
Tustervatn	DEHM	-24.73	-15.24	-4.20	-12.39	**-13.90**	0.69	0.60	0.49	0.52	**0.62**	3.33	4.09	6.54	5.69	**5.86**
	G-M	-14.20	-12.00	-4.80	3.21	**-6.94**	0.78	0.66	0.77	0.77	**0.74**	2.12	3.34	3.36	3.35	**3.04**
Summit	DEHM	-11.55	8.43	-6.75	-13.57	**-4.17**	0.59	0.36	0.56	0.72	**0.40**	3.28	4.70	6.76	3.07	**5.99**
	G-M	-10.40	5.02	-6.41	-3.57	**-3.61**	0.74	0.59	0.25	0.66	**0.58**	1.87	3.58	5.97	2.51	**3.33**

*Normalised mean bias (NMB): $NMB = 100 \times \frac{\sum(M_i - O_i)}{\sum O_i}$

†Pearson correlation coefficient (r): $r = \frac{\sum_1^N M_i O_i - \sum_1^N M_i \sum_1^N O_i / N}{\sqrt{\sum_1^N M_i^2 - N\bar{M}}\sqrt{\sum_1^N O_i^2 - N\bar{O}}}$, where $\bar{M} = \frac{\sum_1^N M_i}{N}$ and $\bar{O} = \frac{\sum_1^N O_i}{N}$

‡Un-biased root-mean-square-error (URMSE): $URMSE = \sqrt{\frac{\sum_1^N [(M_i - \bar{M}) - (O_i - \bar{O})]^2}{N}}$

The model simulations are also compared with buoy and ship observations in Figure 5. As described in Section 2.2.2, the O₃ observations were available from the six O-buoys (8, 11, 12, 13, 14, and 15) and the Japanese research vessel Mirai for different time periods in 2015 with their tracks over various parts of the Arctic Ocean (Fig. 1). In Figure 5, the time series of observed and modelled O₃ are collaged into single plots, respectively, to illustrate that the composite O₃ seasonal patterns shown in the observations over the Arctic Ocean appear to be consistent with those observed at the Arctic coastal sites, i.e.,

the spring period is dominated by ODEs followed by a brief rebound before decreasing to its summer minimum and then

590   recovery in the fall. Like the observations, the modelled O_3 time series along the buoys and ship tracks is also consistent with
those modelled at the Arctic coastal site (Utqiagvik shown, as an example, in Fig.5). The similarity between O_3 observations
over the Arctic Ocean and the coastal sites was also found in other studies (e.g., He et al., 2016; Sommar et al., 2010;
Bottenheim et al., 2009) with the exception of springtime. The model-observation comparisons for individual buoys and
ship, including time series, scatter plots, and statistical scores (i.e., normalised mean bias, NMB, Pearson correlation

595   coefficient, r, and unbiased root-mean-square error, URMSE) are provided in supplementary material (SF.4). The two
models generally track the buoys and ship observations well, particularly for the latter half of the year. The GEM-MACH
model was able to simulate the observed ODEs (O-buoy 11 and 12) during spring. Outside the spring period, the two models
exhibit a similar performance in simulating surface O_3 over the Arctic Ocean compared against observations on the buoys
(O-buoy 8, 13, 14, and 15) and the ship (R/V Mirai), as indicated in the statistical evaluation (SF.4). As for the comparisons

600   at the coastal sites in Figure 4, the model simulated surface O_3 is also biased low over the winter season at the buoy sites
(e.g., O-buoy 11 and 12 over January and February, O-buoy 8, 13, 14, and 15 over November and December; SF.4). It is
notable that both models simulated the O_3 observations on R/V Mirai cruise (September 2015) very well (SF.3), which is in
contrast to the previous effort in simulating the O_3 observations from the multi-year (2013 – 2018) Mirai cruises in the Arctic
(all during September) using global models (Kanaya et al., 2019), where the models in that study significantly

605   underpredicted the surface O_3 observations in the Arctic. Kanaya et al. (2019) suggested that the dry deposition of O_3 over
the ocean may be overrepresented in their model (a dry deposition velocity of ~ 0.04 cm s^{-1} over open water was used in
their case), which may be responsible for the model under-prediction of O_3. As mentioned earlier, GEM-MACH uses a
parameterization representing iodide-mediated O_3 deposition over the open ocean (Sarwar et al., 2015) for the Arctic
simulation, which can result in a dry deposition velocity smaller than the original fixed value of 0.03 cm s^{-1} at locations over

610   high-latitude open oceans, while the O_3 dry deposition velocity of ~ 0.05 cm s^{-1} over open water is used in DEHM (see
Appendix 1). This suggests that the model representation of O_3 dry deposition may only be partially responsible for the
global model underprediction of O_3 over the Arctic Ocean in the earlier study.
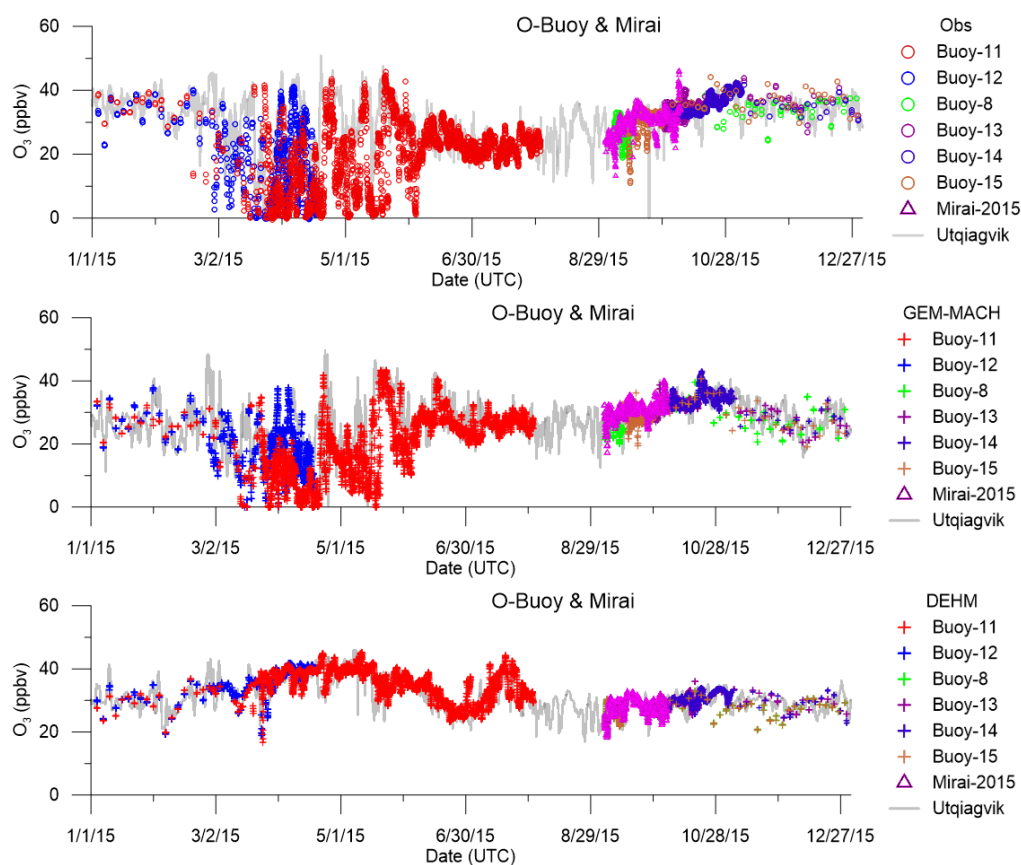
Figure 5. Observed (top panel) and modelled (GEM-MACH – middle panel, DEHM – bottom panel) surface ozone time series along the O-
615 Buoy and Mirai 2015 cruise paths. Also plotted (in grey lines) are the observed (in the top panel) and modelled (GEM-MACH and DEHM, respectively; in the lower two panels) surface O_3 at Utqiagvik site, to illustrate the similarity in seasonal patterns at the buoy and ship locations (over the Arctic Ocean) and coastal sites (e.g., Utqiagvik) shown in both observations and the two models.

3.3 Ozone vertical profiles comparison with ozonesondes

620 To evaluate the models' abilities to simulate the vertical distribution of O_3 over the Arctic, the modelled vertical O_3 profiles at the Arctic ozonesonde sites (see 2.2.3) are compared with the ozonesonde observations. For the comparison, both modelled and observed (ozonesondes) profiles were interpolated at 10-m resolution and binned to 100-m intervals. The vertical profiles of model data were extracted over the grid cells nearest to the ozonesonde launching sites and at the hours closest to the launch times. We focus on the lowest 5 km (ASL) altitude range in this study. Figure 6 includes the seasonal comparisons at the six

625 Arctic sites: Alert, Eureka, Resolute, Ny Ålesund, scoresbysund, and Sodankylä (observation in black, GEM-MACH in red, and DEHM in purple). For the lowest 5 km, the model simulations and observations are in overall good agreement. The spring (MAM) ozonesonde profiles at Alert, Eureka, and Resolute over the Canadian Archipelago are strongly influenced by the ODEs below 1 to 1.5 km (ASL). The GEM-MACH model was more successful in capturing the ODEs at these sites, though

the modelled ODEs were not as strong as the observations close to the surface. The vertical depths of the ODEs, mostly limited
630 to the lowest 1 km, were simulated well. The DEHM simulation did not capture the observed ozone depletion close to the surface. However, above the boundary layer (~1.5 km), the modelled O_3 profiles from the two models do agree well and are in good agreement with observations. The model simulated ozone profiles (from both models) are biased low compared to the ozonesonde measurements over the winter months (DJF) at most of the sites, consistent with the model low bias shown at the surface sites. In the case of GEM-MACH, the overall model low bias in winter could, at least in part, be attributable to the
635 chemical lateral boundary condition from the ECMWF-CAMS reanalysis; both Inness et al. (2019) and Wagner et al. (2021) have found that the CAMS reanalysis (for the period of 2003 to 2018) tends to have a negative bias in surface and tropospheric ozone over the winter season at high latitudes, particularly after 2012/2013, which was linked to a switch in data assimilation procedure. At the Sodankylä site, located in the European boreal region (in close proximity with two of the surface observation sites, Pallas and Esrange), the GEM-MACH simulated ozone has a significant negative bias throughout the lowest 5 km during
640 summer (JJA). The DEHM simulation also shows a similar negative bias above 1.5 km but recovers in the lowest 1.5 km layer where the modelled O_3 concentrations are much closer to that observed. The modelled ozone profiles at Ny Ålesund and Scoresbysund also show similar negative biases at altitudes above 2-3 km during JJA months. This may be indicative of insufficient transport in the free troposphere in both models, but the GEM-MACH model's underprediction of ozone close to the surface at the Sodankylä site could be attributed to the model's over-representation of the O_3 dry deposition over the
645 European boreal region as well as the possible over-predicted biogenic isoprene as discussed earlier in 3.2.
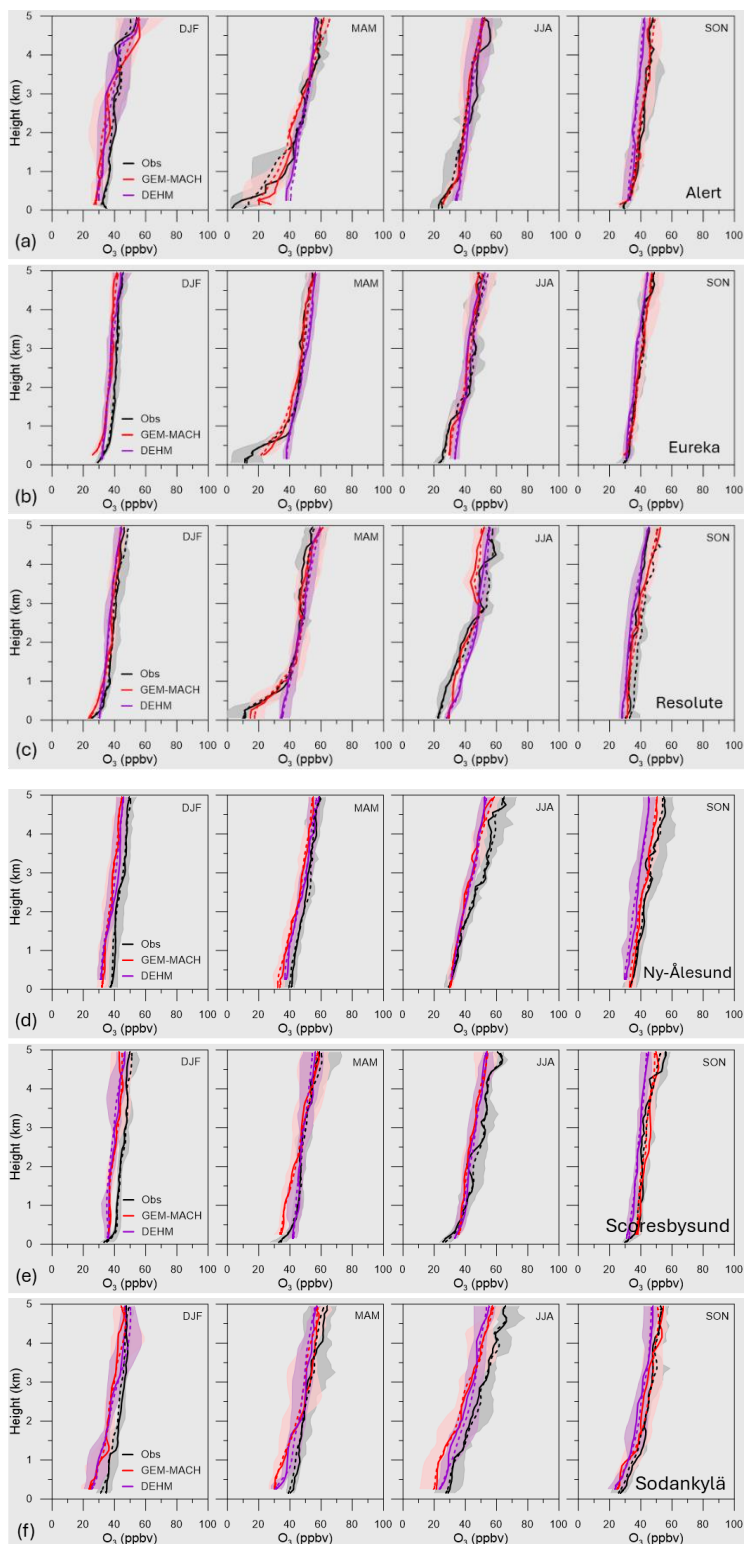
Monthly statistical evaluations for three altitude ranges, 0 – 1 km, 1 – 2 km, and 2 –5 km, are presented in Figure 7, comparing monthly mean, maximum, minimum, and interquartile range between model and ozonesondes at the six Arctic ozonesonde sites. Note that there were no ozonesonde launches in January and December 2015 at Alert and in June 2015 at Resolute and Eureka. Here, again, the distinctively different ozone seasonal patterns between the lowest altitude range (0 – 1

655   km) and the higher altitude range in the free troposphere (2 – 5 km) are evident at all three ozonesonde sites in the Canadian archipelago (Alert, Eureka, and Resolute). The springtime ozone minimum, occurring in May at Alert and in April at Resolute and Eureka, is prominently seen in the lowest 1 km range, driven by the ODEs. The influence of ODEs can be seen in the 1 – 2 km altitude range also at these sites. In contrast, ozone in the 2 – 5 km altitude range exhibits a maximum in late spring (in the month of May) at all sites. The ozonesonde observations in the lowest 1 km altitude range also indicates a

660   maximum in October at the three ozonesonde sites over the Canadian Archipelago, consistent with the GEM-MACH model results shown in Figure 2 and 3. It is also interesting to notice that the usual summer O_3 minimum observed at the surface sites (see Fig. 4) is evident at lower altitudes (below 2 km) but less evident in higher altitudes (e.g., 2 – 5 km) from the ozonesonde observations at these Arctic sites. The statistical evaluation shows generally good agreement between the models and the ozonesonde observations for the three selected altitude ranges at most of the sites. Larger discrepancies between the

665   GEM-MACH model and observations are seen in June and July at the Sodankylä site, consistent with the model's underprediction of summertime O_3 at the surface sites in the European boreal region (as discussed above). Again, overall, the two models are seen to have good skills in reproducing the observed O_3 vertical distribution and seasonal cycles over the Arctic (except for the coastal sites where DEHM was unable to reproduce the observed O_3 influenced by ODEs in spring).
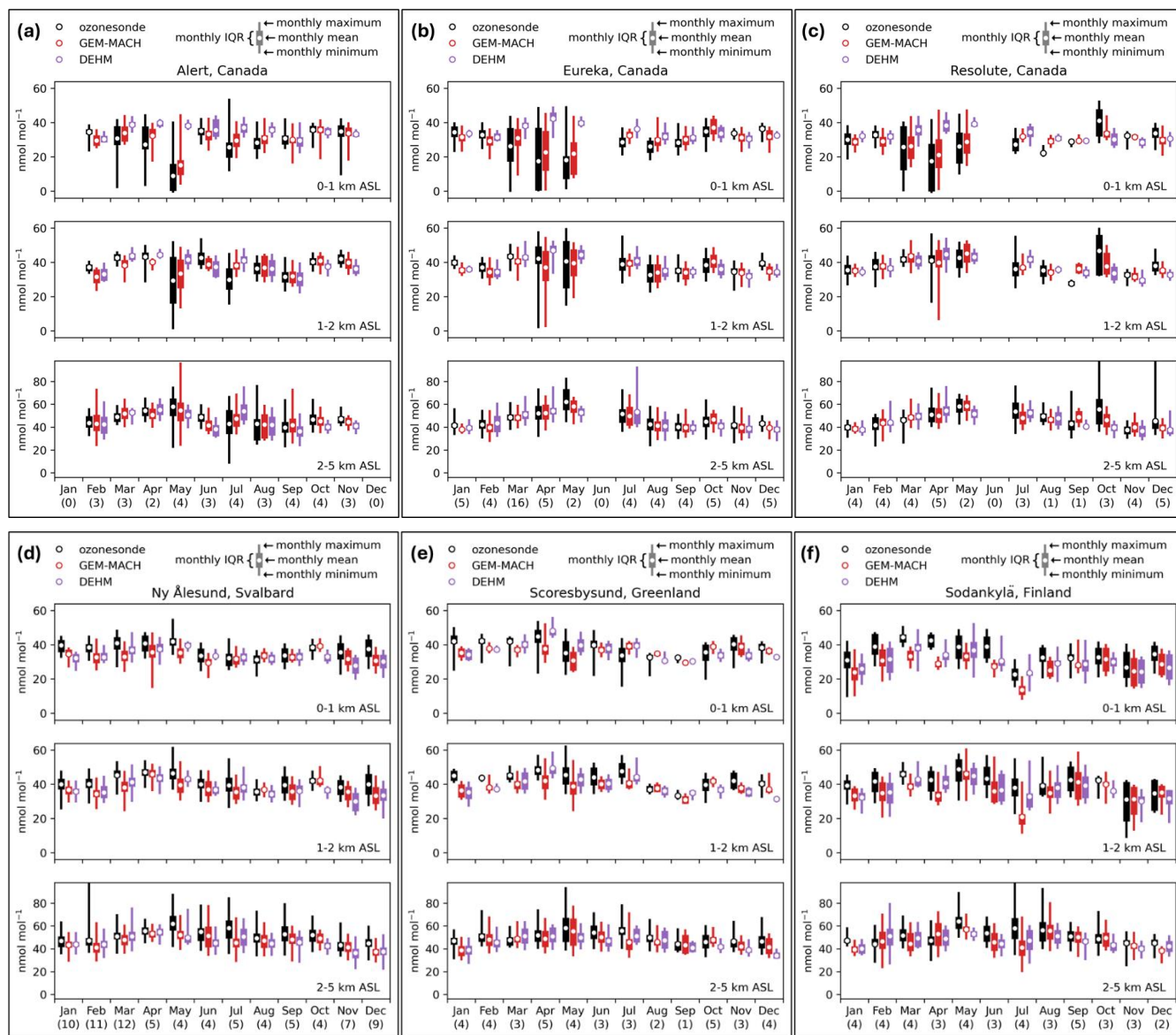
Figure 7. Statistical evaluation of modelled O₃ profiles against ozonesonde observations at Alert (a), Eureka (b), Resolute (c), Ny-Ålesund (d), Scoresbysund (e), and Sodankylä (f), for three altitude ranges (top: 0 – 1 km ASL, middle: 1 – 2 km ASL, and bottom: 2 – 5 km ASL). Monthly mean, interquartile range (IQR) and full data range from minimum to maximum for each month are denoted by open circles, thick bars and thin bars, respectively (observation in black; GEM-MACH in red; DEHM in purple). The number of observed ozone profiles available in each month of the year 2015 at each site is indicated in parentheses (underneath each month).

4 Discussions

4.1 Modelling springtime ODEs: sensitivities to process representations and their uncertainty

As shown from the observations and model results presented in Section 3, the springtime ODEs play an important role in driving the Arctic surface O_3 seasonal cycles. The main uncertainty in modelling the springtime ODEs is in quantifying the

680 sources for reactive bromine in the Arctic boundary layer. As described in 2.1.3, the two models included in this study, DEHM and GEM-MACH, each consider different sources of reactive bromine; GEM-MACH adopted a representation of a snowpack bromine source mechanism following Toyota et al. (2011), while DEHM implemented a representation of sea-salt aerosol sourced bromine from blowing snow and open ocean sea spray following Yang et al. (2010).

In Figure 8, we examine model simulations of ODEs at the 4 coastal sites (Utqiagvik, Villum, Tiksi, and Zeppelin) in more

685 detail; these are the only Arctic coastal sites under the strong influence of ODEs with surface O_3 data available for 2015. Included in Figure 8 (a-d) are time series of observed and modelled (DEHM and GEM-MACH) surface O_3 for March, April, and May. Included with the O_3 time series are the modelled O_3 deficit (or depletion) due to bromine chemistry (computed from the difference between the modelled surface O_3 concentration with and without the snow-sourced bromine[1]), modelled surface BrO, modelled and observed wind speed and direction at these sites. Note that the modelled O_3 deficit (or depletion) due to

690 bromine chemistry shown in Fig. 8 can be a result of the photochemical O_3 loss having occurred either locally or regionally, i.e., transport of ozone-depleted air mass from elsewhere, and their combination. Similar to those reported previously, the observed ODEs at these coastal sites are highly variable with time, and dependant on local and synoptic meteorological conditions that can promote or diminish the accumulation of O_3-destroying bromine species sourced from the surface and can also facilitate the concentration recovery of O_3 via vertical and horizontal air mass exchanges (Halfacre et al., 2014; Jacobi et

695 al., 2010; Oltmans et al., 2012; Pernov et al., 2024; Simpson et al., 2007). Most of the ODEs observed at these Arctic sites occurred between mid-March and early June. There were a few brief episodes of depletion in early March observed at Utqiagvik when surface O_3 concentrations decreased by about 20 ppbv from the background level of 30 – 40 ppbv to about 10 ppbv, which may well be associated with bromine chemistry given its relatively southern location (71.32°N, hence having more than 10 hours daylight by early March) (Frieß et al., 2011) and its proximity to FY sea ice. The GEM-MACH simulation

700 was able to reproduce these episodes, while the DEHM simulation produced a minor depletion of an order of 5 ppbv (Fig. 8(a)). Both model simulations showed the notable presence of BrO during this period, an indication of active bromine chemistry. In contrast, Tiksi did not experience any significant depletion events until late March and into April, (except for one event at the beginning of March that is captured by the GEM-MACH simulation), despite its relatively southern location (71.59°N). It is worth noting that the local winds at this site were predominantly south-westerly, i.e., from the land, over most

705 of March, while during the months of April and May, the winds were relatively light and variable with a large onshore

---

[1] In the case of GEM-MACH, a sensitivity run was conducted with the snowpack bromine flux turned off which effectively turned off the bromine chemistry in the simulation. In the case of DEHM, a sensitivity run was conducted by turning off the blowing-snow-sourced bromine while the open-ocean sea-spray-sourced bromine remained active.

component (from the Arctic Ocean), coinciding with the observation of more frequent ODEs (Fig. 8(c)). The close association between ODEs and onshore winds is evident at all three coastal sites shown in Fig. 8 (a-c), which is consistent with the finding from a recent observation-based analysis (Pernov et al., 2024). The Zeppelin site on Svalbard is at 474 m above sea level and the observations at this site are less influenced by the surface and often representative of the air above the stable polar boundary

710 layer above the ice-covered ocean (Dekhtyareva et al., 2018). Compared to other coastal surface sites, ODEs were observed less frequently during the spring O_3 depletion season at this site. The GEM-MACH model with a representation of snowpack bromine source mechanism (as described in Sect. 2.1.3) was able to simulate the observed ODEs reasonably well at each of the sites shown in Fig. 8. In comparison, the DEHM model with a representation of blowing-snow sea salt bromine source mechanism (see Sect. 2.1.3) captured fewer ODEs and generally produced weaker ozone depletions, though it sometimes

715 reproduced the ODEs reasonably well such as at the Zeppelin site in April. The DEHM-simulated ODEs (and the accompanied enhancements in surface BrO) are more episodic (short duration) and are often associated high wind periods consistent with possible blowing snow events. This is particularly evident at the Utqiagvik and Villum sites (Fig. 8(a) and (b)). On the other hand, while GEM-MACH generally simulated the observed ODEs at the Villum site well, reproducing the multiple ODEs over late March and April and the extended low O_3 period (well below the background level) during the entire month of May, the

720 modelled ODEs do not always temporally coincide with the observed ODEs. This can be linked to the poor agreement between the modelled and the observed wind at this site, which is particularly evident during the first half of April when the modelled and observed O_3 time series are out-of-phase during the periods when the modelled wind directions are also out-of-phase with the observations, switching between onshore and offshore. The discrepancy between modelled and observed winds at this site appears to be largely due to the poor model representation of the local topography that is dominated by the Flade Isblink

725 Icesheet south of Villum Research Station. It is worth noting that the DEHM model did capture a deep ODE at Villum on April 23, though the duration of this modelled ODE is much shorter than the observed ODE; the DEHM model also captured a few ODEs observed at Zeppelin in late April. Overall, it seems that the inclusion of the snowpack-sourced bromine is more successful in simulating the spring Arctic ODEs while the blowing snow sourced bromine alone is insufficient in reproducing the observed springtime ODEs in the Arctic. This is in line with the findings from recent studies (Huang et al., 2020; Marelle

730 et al., 2021; Swanson et al., 2022). Swanson et al. (2022) compared their model simulations with only the snowpack bromine source mechanism and with both snowpack and blowing snow bromine sources and found that, while both sources are needed for simulating the springtime ODEs in their study, the snowpack-sourced bromine plays a major role. This is perhaps understandable, as the snowpack bromine source mechanism triggered by the dry deposition of O_3, HOBr and $BrONO_2$ can be sustained continually under a variety of meteorological conditions, while the blowing snow bromine source mechanism

735 triggered by high wind conditions tends to be more episodic. Indeed, both Halfacre et al. (2014) and Pernov et al. (2024) have found that the ODEs observed in the Arctic tend to be more associated with calm wind conditions.
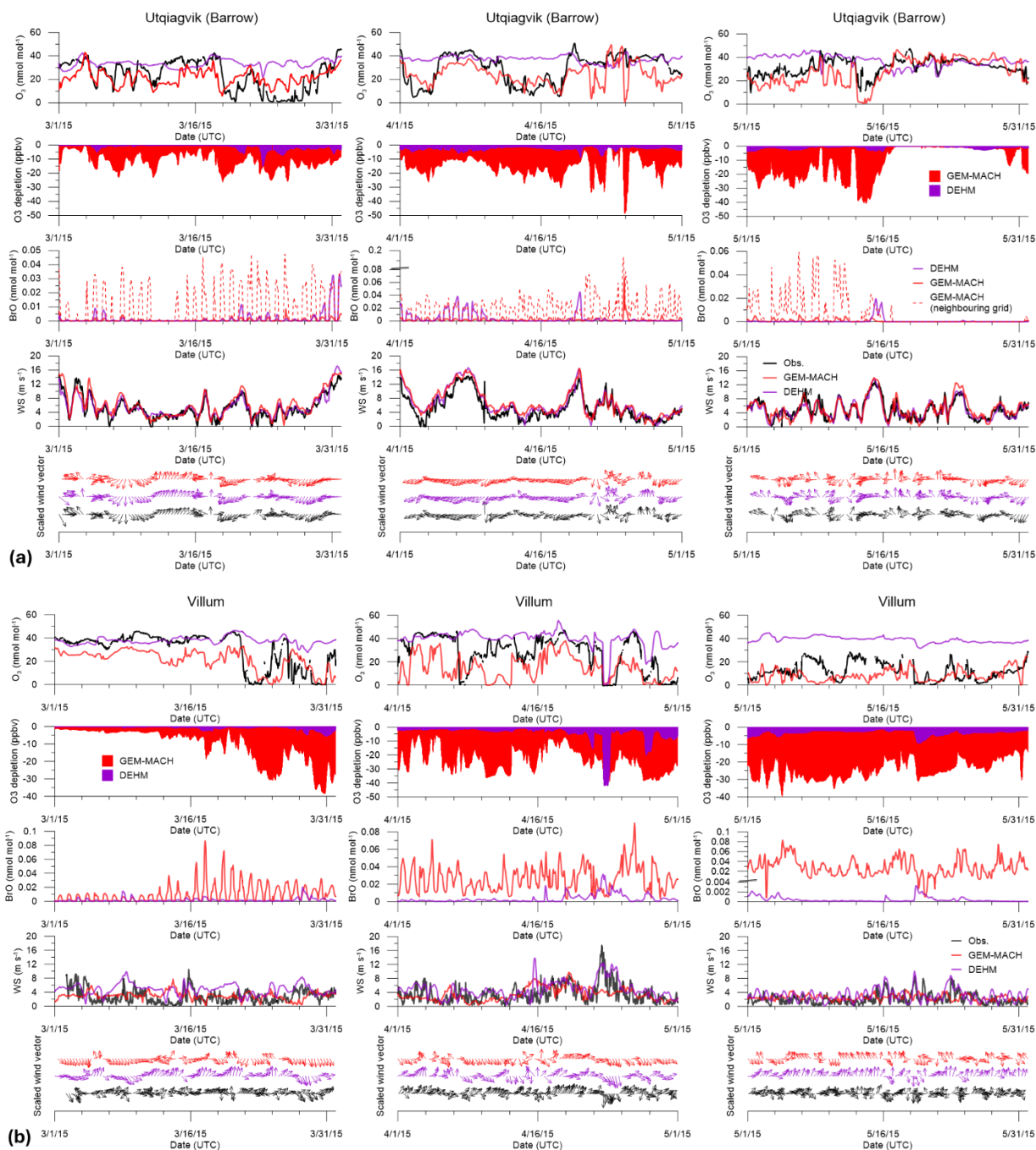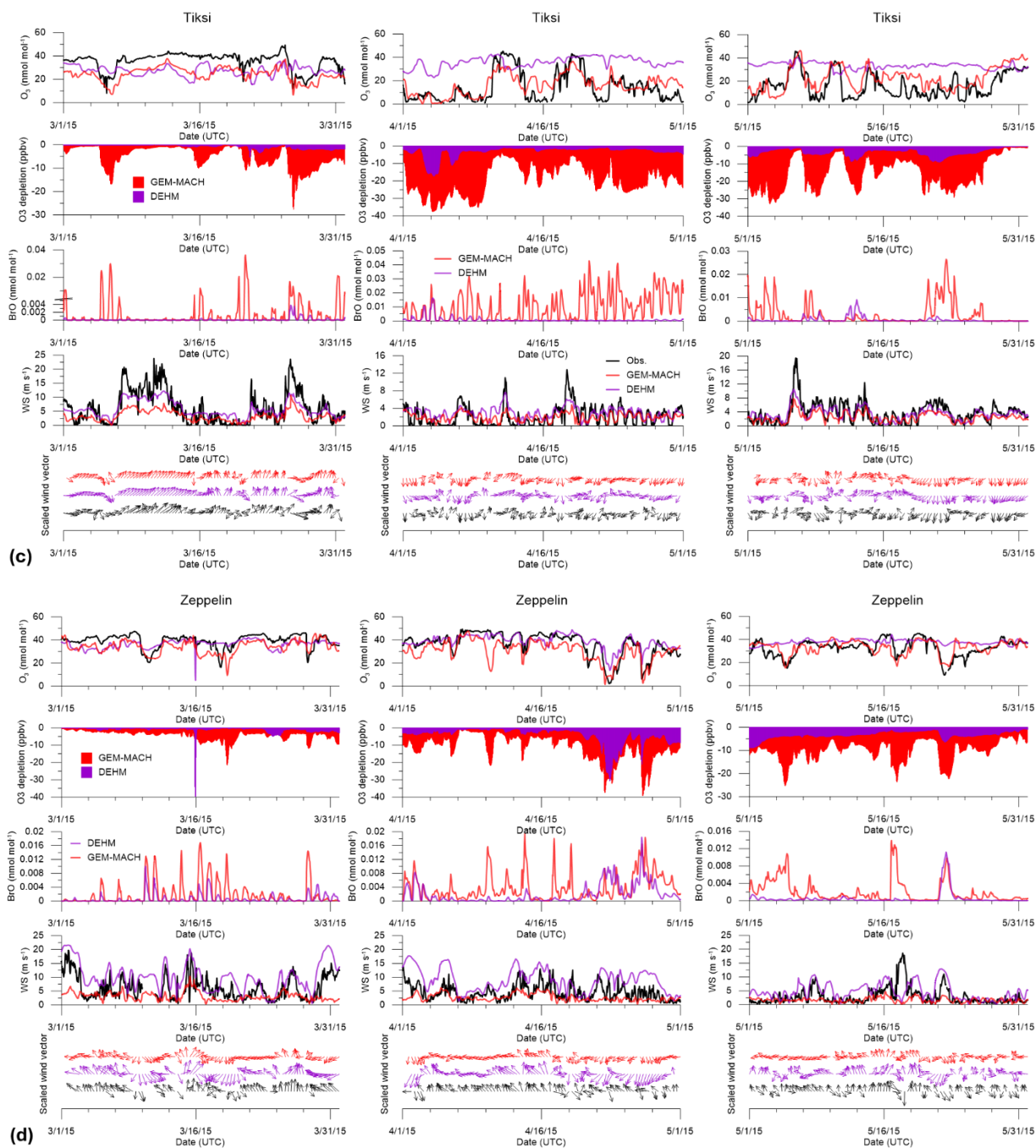
Figure 8. Model simulated spring ODEs at 4 Arctic coastal sites (for March, April, and May; shown in separate panels): (a) Utqiagvik, (b) Villum, (c) Tiksi, and (d) Zeppelin. In each panel: top row – time series of modelled surface O3 (GEM-MACH in red and DEHM in purple) compared with observation (in black); 2nd row: time series of modelled O3 deficit (depletion) due to bromine, or the difference between model simulated surface O₃ with snow sourced bromine (i.e., snowpack sourced bromine in the case of GEM-MACH, and blowing-snow sourced bromine in the case of DEHM) and the model simulation without the snow sourced bromine, (red shade – GEM-MACH; purple shade – DEHM); 3rd row: time series of the modelled surface BrO concentrations (red – GEM-MACH, purple – DEHM); 4th row: time series

of the modelled and observed wind speed at the Utqiagvik site (black – observation, red – GEM-MACH, purple – DEHM); 5th (bottom) row: comparison of modelled and observed wind direction (shown as scaled vectors) at the Utqiagvik site (black – observation, red – GEM-MACH, purple – DEHM). The meteorological observation data at the Utqiagvik site were collected by NOAA Global Monitoring Laboratory
750 (GML) and obtained from https://gml.noaa.gov/data/data.php?site=brw (last access: 2024-11-27).

While there are relatively abundant surface observations of the Arctic springtime ODEs from the ground-based monitoring sites and mobile platforms (e.g., buoys and research vessels) in the Arctic Ocean (Bottenheim et al., 2009), observations on the vertical structure of ODEs are scarce. During the 2015 NETCARE spring field campaign, O_3 measurements were made onboard the Alfred Wegener Institute Polar-6 aircraft. Figure 9 shows the ozone vertical profiles taken by the aircraft during
755 the 2015 NETCARE field campaign over the Canadian archipelago (around Ellesmere Island over an ice-covered sea surface) along with the modelled profiles (from GEM-MACH and DEHM) extracted at the flight profiling location and time. Also included are the modelled profiles from the runs with the snow-sourced bromine emissions turned off. The segments of the flight tracks during profiling are shown in the inserted map. A shallow ozone depletion layer, with depth ranging between about 500 m to about 1 km can be seen from the profiles taken over the Arctic Ocean off the west side of Ellesmere
760 Island (2015-04-07, 2015-04-08_2, 2015-04-11_2, and 2015-04-13_2). The profiles taken over the Nares Strait (2015-04-08_1 and 2015-04-09) and over Ellesmere Island (2015-04-10 and 2015-04-11_1) all show a deeper layer, ~ 2 km, of depleted O_3, likely due to transport and vertical mixing of the near-surface bromine mediated O_3 depletion. In particular, over the interior of Ellesmere Island, a much deeper layer, up to 4 km, can be impacted by the ODEs due to enhanced mixing (comparing the model-simulated O_3 profiles with vs. without bromine corresponding to the flight on April 10). As shown,
765 the GEM-MACH simulation with snowpack-sourced bromine was able to simulate the vertical structure of the depletion layer reasonably well. There are cases where the model was not able to fully simulate the observed depletion close to the surface (e.g., 2015-04-07, 2015-04-08_2, and 2015-04-10), which may be attributable, at least in part, to model resolution (15-km) and the very shallow mixing height of the Arctic atmosphere (e.g., Gryning et al., 2023). The DEHM simulation with the blowing-snow sourced bromine was not able to reproduce the observed near-surface depletion, although for several
770 flights (e.g., 2015-04-10, 2015-04-11_1, 2015-04-11_2, and 2015-04-13_2), the DEHM simulations do show some modest ozone loss from the blowing-snow sourced bromine (comparing the two DEHM model runs with and without the blowing-snow bromine). It is interesting to notice that the DEHM model simulated vertical O_3 profiles are in close agreement with the GEM-MACH simulated O_3 vertical profiles without bromine, and all the modelled profiles are in reasonably good agreement with the observed profiles above the atmospheric boundary layer, within the lowest 5 km.
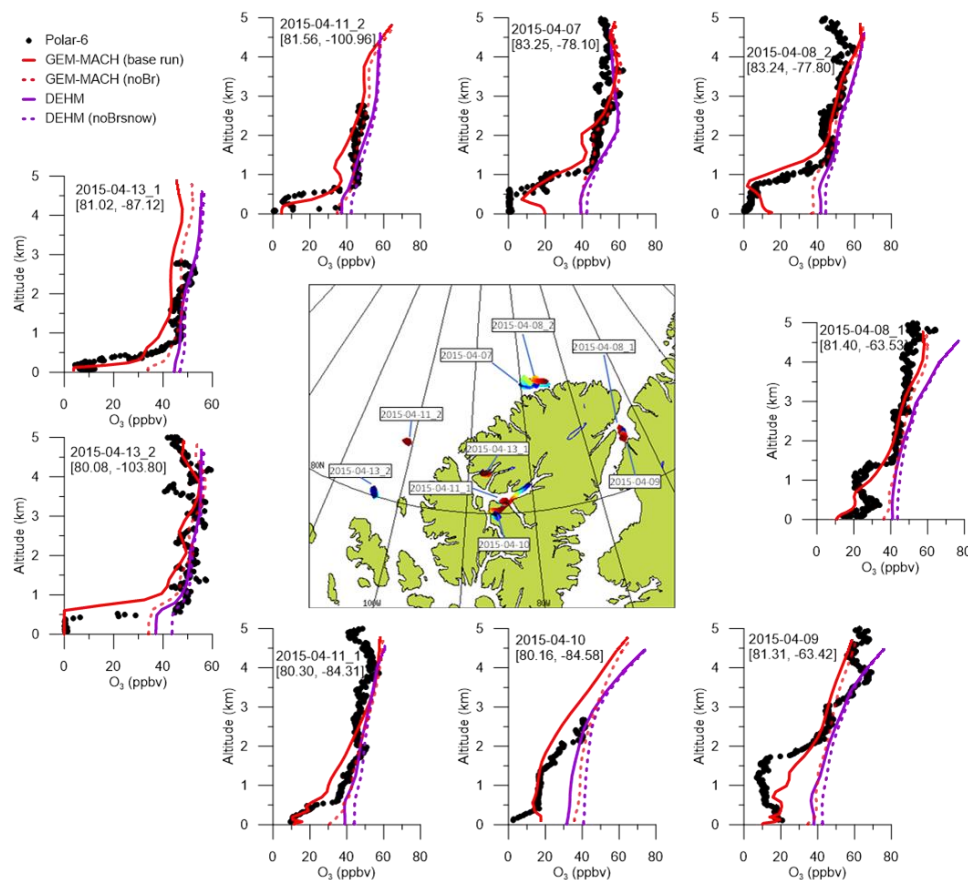
Figure 9. Modelled ozone profiles compared to observations from the Polar-6 flights conducted during the 2015 NETCARE spring campaign around Ellesmere Island, Canada in April 2015: observations (black dots), GEM-MACH in red, DEHM in purple. Also plotted are modelled profiles from the no-bromine GEM-MACH run (red dashed lines) and from the DEHM run with blowing-snow bromine turned off (dashed purple lines). Model profiles were extracted from the grid containing the average lat-lon locations of the aircraft profiling flight segment.

To evaluate the modelled bromine levels, the modelled bromine monoxide vertical column densities (BrO VCDs) are compared to the MAX-DOAS measurements available at the Utqiagvik site and on O-Buoy 10, 11, and 12 during spring 2015. Figure 10 shows the comparison in terms of monthly statistics while the hourly timeseries comparisons are shown in the supplementary material (SF.5), (note that the monthly stats for both measured and modelled BrO VCDs were calculated based on the data entries with available measurement). The difference between the two modelled BrO fields is largely due to the bromine sources considered in each model, i.e., snowpack-sourced bromine (based on Toyota et al., 2011) in GEM-MACH and open-ocean and blowing-snow sourced bromine (based on Yang et al., 2010) in DEHM. At the Utqiagvik site, the monthly BrO VCDs simulated with the snowpack-sourced bromine (GEM-MACH) tracked the MAX-DOAS measurement well over the period when the measurement was available (February 21 to June 10, 2015). The modelled monthly BrO VCDs with open-ocean and blowing-snow sourced bromine (DEHM) were considerably lower than the measurements for the month of March and April. The MAX-DOAS measurements on O-Buoys were available for much shorter periods in 2015, April 21 – June 10

for O-Buoy 10 and 11, April 21 – May 22 for O-Buoy 12. The GEM-MACH-simulated monthly BrO VCDs with the snowpack-sourced bromine were considerably higher than the measured BrO VCDs on Buoy 10 in April, mostly driven by an event at the beginning of the measurement period (SF.5). On the other hand, the DEHM simulated BrO VCDs with open-ocean and blowing-snow sourced bromine were significantly lower than the measurements on the buoys. These findings are consistent
795 with the results from Swanson et al. (2022) where simulations using the GEOS-CHEM model were conducted for a 10-month period (March – November) in 2015 with different snow sourced bromine mechanisms (i.e., snowpack and/or blowing snow). The DEHM simulated BrO VCDs are comparable to those from the Swanson et al. simulation with the blowing-snow bromine mechanism alone (their "BLOW" run). Their study also showed much higher BrO VCDs obtained from the simulations with the snowpack bromine mechanism alone (their "PACK" and "PHOTOPACK" runs; the latter considered an enhanced bromine
800 molar yield from snowpack upon O_3 deposition under sunlit conditions as in Toyota et al., 2011) compared to that with blowing snow mechanism alone. The comparison between the GEM-MACH simulated BrO VCDs from this study with those from Swanson et al. (2022) snowpack-only simulations varies. For example, the GEM-MACH-simulated BrO VCDs compared well with the MAX-DOAS measurement at Utqiagvik, while both simulations with snowpack-sourced mechanism ("PACK" and "PHOTOPACK") from Swanson et al. (2022) produced much higher BrO VCDs than the measurement particularly from the
805 run with enhanced bromine molar yield for sunlit conditions ("PHOTOPACK"). On the other hand, the GEM-MACH simulated BrO VCDs at the buoy locations are more comparable to those from the two snowpack runs in Swanson et al. (2022). This is partly due to the parameters selected (e.g., the bromine molar yields; see 2.1.3) for the snowpack bromine source mechanism in the different studies. Also worth mentioning is the dependency of bromine production on O_3 deposition in the snowpack bromine source mechanism of Toyota et al. (2011). GEM-MACH employs a reduced O_3 dry deposition velocity
810 over ice and snow surfaces, 0.01 cm s^{-1} (following Helmig et al., 2007), while a much higher O_3 dry deposition velocity over the Arctic sea ice, between 0.02 and 0.1 cm s^{-1}, was used in Swanson et al. (2022). The uncertainty in the parameterization of snowpack bromine source mechanism is examined next.
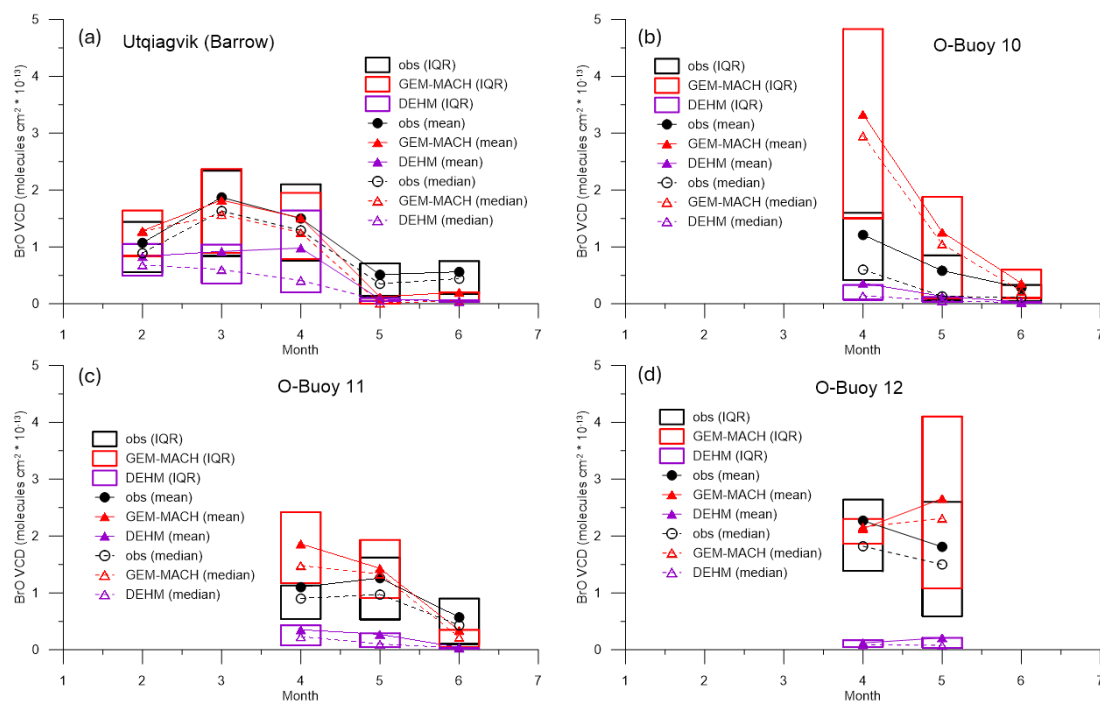
Figure 10. Comparison of modelled and measured (MAX-DOAS) monthly BrO VCDs (molecules cm^{-2}) at Utqiaġvik (a) and O-Buoy
locations (b, c, and d); observations in black, GEM-MACH (from snowpack sourced bromine) in red, and DEHM (from open ocean and
blowing-snow sea salt sourced bromine) in purple.

The current model representations of bromine source mechanisms are highly parameterized, and there are large uncertainties
in some of the parameters employed by these parameterizations due to lack of constraint by available lab or field experiments.
Some of the studies adopting the approach of Toyota et al. (2011) for the snowpack bromine source mechanism have chosen
parameters in variation to those recommended by Toyota et al. (2011). For example, Swanson et al. (2022) chose to make no
distinction between FY and MY sea ice in treating snowpack Br$_2$ production; Herrmann et al. (2021) considered an
enhancement factor β (≥ 1.0), to account for non-flat surfaces such as ice or snow and frost flowers, in computing fluxes from
Br$_2$ surface production. As mentioned in Sect. 2.1.3, in this study, the molar yields for Br$_2$ production from snowpacks over
FY and MY sea ice upon dry deposition of O$_3$ (Φ$_1$) were set at 0.15 and 0.075, respectively under sunlit, and at 0.01 and 0.005,
respectively, under dark conditions in the GEM-MACH simulation presented so far. These are larger than the original values
used in Toyota et al. (2011); they were chosen to partly compensate the possible under-representation of the Br$_2$ production
from reactive bromine cycling through aerosol heterogeneous chemistry due to under-predicted Arctic haze aerosols in the
model (see Gong et al., 2024). To explore the sensitivity to the Br$_2$ molar yields associated with O$_3$ dry deposition on snowpacks
(Φ$_1$) and the role of reactive bromine cycling through aerosol heterogeneous chemistry, two additional sensitivity runs with
GEM-MACH were conducted for the spring period (Feb – May; Feb as spin-up). The parameter settings for various GEM-
MACH runs are specified in Table 3.

Table 3. Parameter settings for the GEM-MACH simulations related to Br_2 production (FYI → first-year ice; MYI → multi-year ice).

	Φ_1 (Br_2 molar yields associated with O_3 dry deposition)				Enhanced heterogeneous chemistry production of Br_2
	FYI_sunlit	FYI_dark	MYI_sunlit	MYI_dark	
Base	0.15	0.01	0.075	0.005	no
Sens-Phi1	0.075	0.001	0.01	0.001	no
Sens-aerosol	0.075	0.001	0.01	0.001	yes
No-bromine	0.0	0.0	0.0	0.0	no

835 Figure 11 shows the modelled O_3 timeseries from the various GEM-MACH simulations compared to observations at three coastal sites that were most impacted by ODEs (Utqiagvik, Villum, and Tiksi) as well at O-Buoy 11 (the only buoy with observations during the entire spring O_3 depletion season); plots for additional sites are included in Supplements (SF.6). The Sens-Phi1 run used the molar yields Φ_1 close to the values recommended by Toyota et al. (2011), i.e., 0.075 and 0.001 for FYI, under sunlit and dark conditions, respectively. For MYI the molar yields Φ_1 were set at 0.01 and 0.001, respectively for sunlit

840 and dark conditions, as opposed to zero in Toyota (2011). As shown in Fig. 11, the model simulated ODEs are weaker in this case than those simulated from the base run, most significantly during March, the early stage of the O_3 depletion period (e.g., O-Buoy 11, Utqiagvik, and Tiksi in Fig. 11; O-Buoy 12, Alert, and Eureka in SF.6). In the Sens-aerosol run, the molar yields (Φ_1) were kept the same as in Sens-Phi1, but the aerosol heterogeneous reaction rates were enhanced by doubling the total aerosol surface area (considering the model under-prediction of Arctic haze aerosols, as mentioned above) to illustrate the role

845 of reactive bromine cycling through heterogeneous chemistry on aerosol surfaces. The enhanced aerosol heterogeneous chemistry (via the artificially increased aerosol loading) resulted in generally stronger model simulated ODEs than those from the Sens-Phi1 run shown in Fig. 11 and SF.6, with somewhat more significant enhancements in the modelled ODEs mostly during mid-April to mid-May (though at Tiksi, the most significant impact from aerosol heterogeneous chemistry is seen during an extended depletion event in the beginning of April). However, the impact of the enhanced aerosol heterogeneous

850 reaction on surface ODEs seems to be rather limited during the initial stages of the depletion season (March).
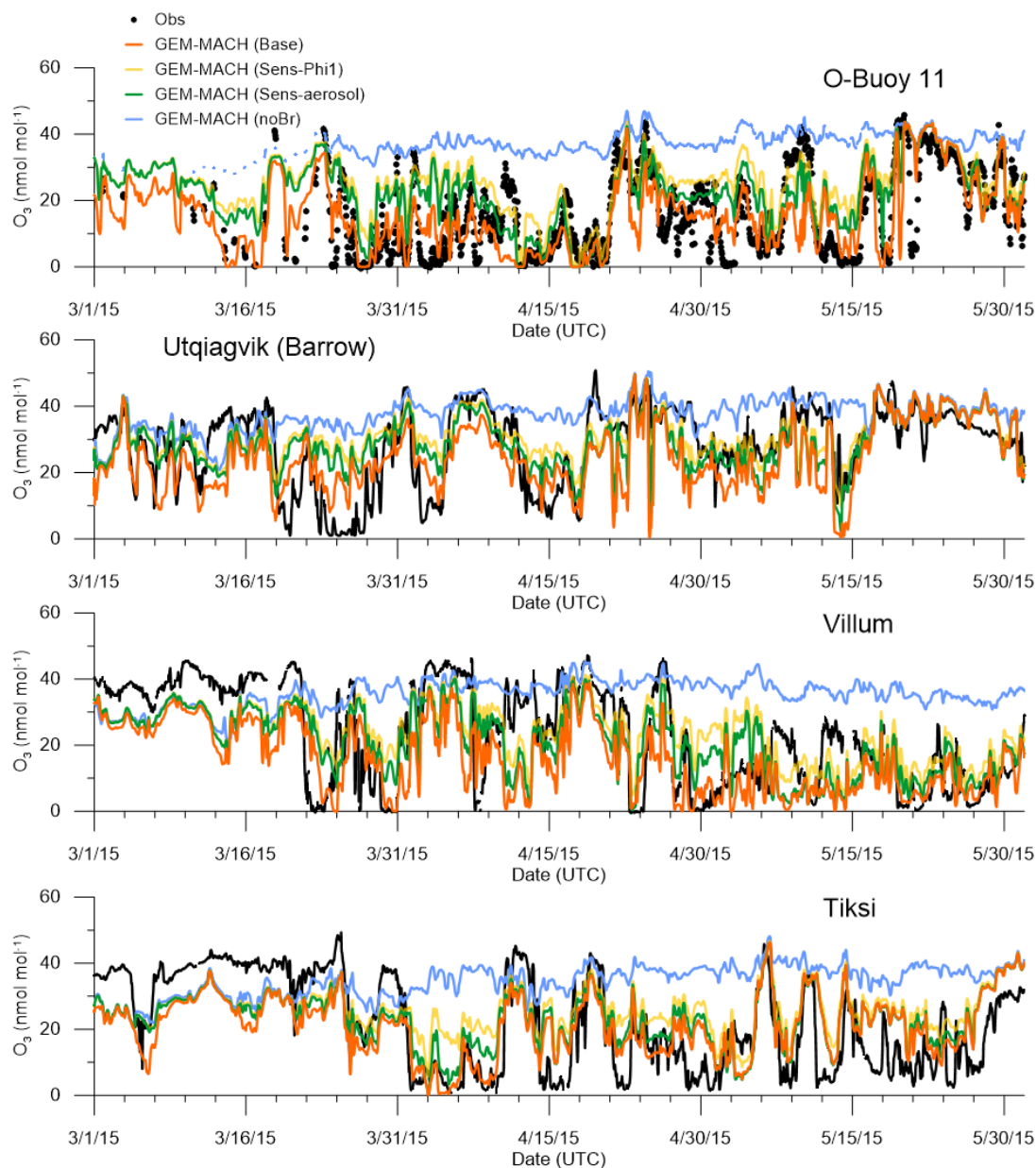
Figure 11. GEM-MACH simulated O_3 time series from the base (orange) and sensitivity runs, Sens-Phi1 (yellow) and Sens-aerosol (green), compared with observations (black) over Beaufort Sea (O-Buoy 11) and at coastal sites: Utqiagvik, Villum, and Tiksi. Also plotted are the modelled O_3 timeseries from the No-bromine run (blue).

855   The comparative roles of snowpack Br_2 emission and the Br_2 production through aerosol heterogeneous chemistry on ODEs are examined here. Figure 12 compares the modelled monthly averaged daily snowpack Br_2 flux and the daily Br_2 production from aerosol heterogeneous chemistry, both in moles per m^2, in the lowest 200, 500, and 1000 m of air from the three GEM-MACH runs (Base, Sens-Phi1, and Sens-aerosol) for March 2015. The same plots for April and May are included in

Supplementary (SF.7 and 8). For the Base run, the March-averaged daily snowpack Br_2 flux is mostly distributed along the
860 coastlines over FY sea ice. Comparing the Br_2 productions from snowpacks and through heterogeneous chemistry on aerosol surfaces, the former (snowpack production) is greater than the latter (aerosol surface chemistry) over the lowest 200 m of the atmospheric column, while for the increased column extent of over the lowest 500 m and 1 km layers, the latter becomes greater. It is particularly noticeable that the atmospheric Br_2 production through the heterogeneous reaction spreads much more widely over the Arctic compared to the snowpack fluxes of Br_2. With the reduced molar yields associated with O_3 dry
865 deposition (Φ_1) in Sens-Phi1, the Br_2 production from the snowpacks is reduced significantly; the production through aerosol heterogeneous reaction is also reduced as a result of reduced bromine oxidation products (HBr, HOBr, and $BrNO_3$) in the air. The snowpack Br_2 flux is further reduced in the Sens-aerosol run, compared to the Sens-Phi1 run, due to reduced O_3 deposition (resulting from enhanced ODEs), while the production of Br_2 in the atmosphere is increased from the enhanced heterogeneous reaction rate (through the doubling of aerosol surface area). By May, the atmospheric Br_2 production through heterogeneous
870 reactions from the Sens-aerosol run exceeds that from the Base run (see SF.8). Figure 13 shows the time series of the pan-Arctic (> 66.5°N) integrated daily snowpack Br_2 production and the Br_2 production through aerosol heterogeneous reactions from the three GEM-MACH runs (top two panels in Fig. 13). The reduction in snowpack production of Br_2 from the lower Φ_1 values in Sens-Phi1 is largest at the beginning of March and the difference between the Sens-Phi1 and Base runs in snowpack Br_2 production reduces gradually over time (particularly after April). In contrast, the increase in the atmospheric production
875 of Br_2 due to enhanced heterogeneous reactions in the Sens-aerosol run (as compared to the Sens-Phi1 run) starts small at the beginning of March but gradually increases with time to exceed the atmospheric production in the Base run by mid-April. This contrast is better illustrated from the bottom panel of Fig.13, showing the difference in snowpack Br_2 production in response to the change in snowpack bromine yield from O_3 dry deposition (Φ_1: Base – Sens-Phi1) and the difference in atmospheric Br_2 production (via aerosol heterogeneous reactions) in response to the change in aerosol surface area (Sens-aerosol – Sens-Phi1).
880 The gradual increase in atmospheric production of Br_2 (via aerosol heterogeneous reactions) over March and April may reflect the gradual increase in photolysis and photochemical reactivity over central Arctic during this time (polar sunrise).
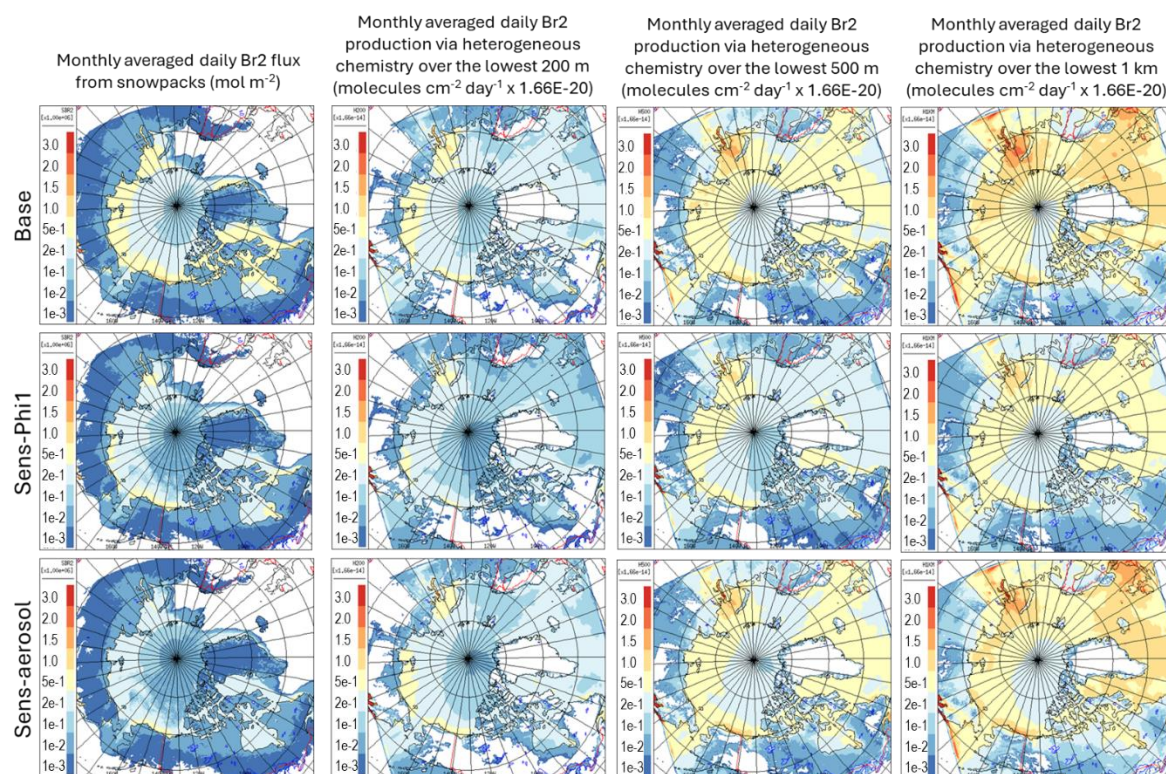
Figure 12. GEM-MACH modelled monthly mean (2015 March) Br_2 daily flux from snowpacks (leftmost column) and Br_2 daily production from aerosol heterogeneous reaction over the lowest 200 m (2nd column from left), the lowest 500 m (3rd column from left), and the lowest 1 km (rightmost column), all in moles m^{-2}, from the base (top), Sens-Phi1 (middle), and Sens-aerosol runs (bottom).
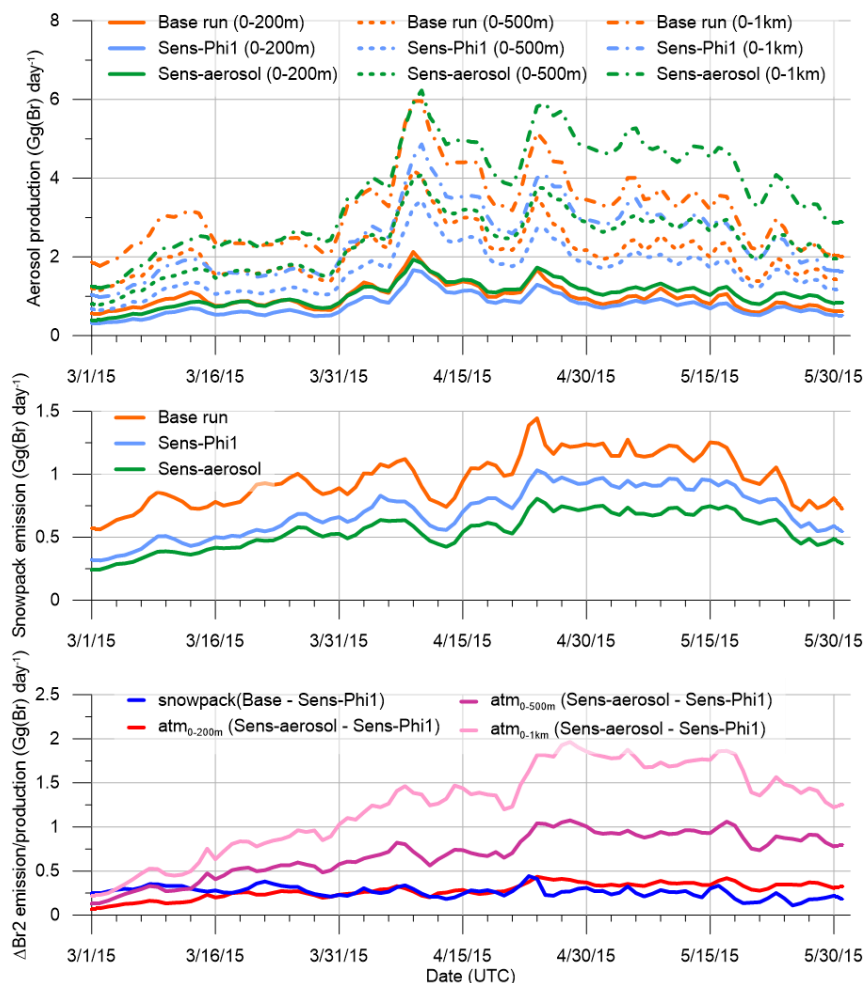
Figure 13. Pan-Arctic (> 66.5°N) integrated Br_2 production from aerosol heterogeneous reactions (top) and from snowpacks (middle) from GEM-MACH runs (Base, Sens-Phi1, and Sens-aerosol) during spring (March to May). The bottom plot shows the sensitivity of Br_2 productions to snowpack bromine yield upon O3 dry deposition (Φ_1: Base – Sens-Phi1) and to atmospheric reactive bromine cycling via aerosol heterogeneous reactions (Sens-aerosol – Sens-Phi1).

We examine the pan-Arctic O_3 loss from bromine chemistry and its sensitivity to the snowpack and atmospheric production of Br_2 in Figure 14. The bromine-induced O_3 loss (negative) is derived by subtracting the net O_3 production in the No-bromine run from those in the three runs with bromine, i.e., Base, Sens-Phi1, and Sens-aerosol runs, respectively. Fig.14(a) shows that the largest O_3 loss (or O_3 depletion) from bromine explosions happens within the lowest 200 m layer, followed by the 200-500m layer. The O_3 loss associated with bromine above 1 km contributes insignificantly to Arctic ODEs. Fig.14(b) further illustrates the comparative impact of snowpack production of Br_2 and the atmospheric production of Br_2 from reactive bromine cycling through heterogeneous reactions on aerosol surfaces. The reduced O_3 loss (or increase in O_3) from the lower molar yields associated with O_3 dry deposition on snowpacks in Sens-Phi1 is also most significant within the lowest 200 m of the air; its impact decreases with height. In contrast, the enhanced heterogeneous chemistry reactions (via doubling the aerosol

surface area) in Sens-aerosol have only a relatively modest impact on the O_3 loss in the lower atmosphere and are comparable initially at 0-200 m and 200-500 m. The impact increases with time and, by April, the most significant impact on O_3 loss due to enhanced heterogeneous reactions is found in the 200 – 500 m layer followed by the 500 m – 1 km layer. Overall, the bromine-induced O_3 loss seems to be more sensitive to the snowpack production of Br_2 than its atmospheric production via heterogeneous chemistry on aerosols. It is worth pointing out that the Br_2 produced through the heterogeneous reactions on aerosol surfaces is originally from the surface-sourced Br_2 (in GEM-MACH), which then undergoes gas-phase photochemical processing to form compounds like HBr, HOBr and $BrNO_3$ which, in turn, can reform Br_2 through heterogeneous reactions on acidic aerosol surfaces (Fan and Jacob, 1992; Michalowski et al., 2000; Saiz-Lopez and von Glasow, 2012). Hence the production of Br_2 through this reactive bromine cycling process and its subsequent impact on ODEs will ultimately depend on the bromine release from the snowpacks (or other sources, e.g., blowing snow and sea spray sea salt) and atmospheric oxidation processes that facilitate the formation of HOBr and $BrONO_2$. On the other hand, the heterogeneous cycling process allows the atmospheric production of Br_2 to be at distances far away from the original source locations (snowpacks in this case) through atmospheric transport as seen from Fig. 12 (and SF.7 and 8), which is consistent with the findings from the airborne field study of (Peterson et al., 2017).
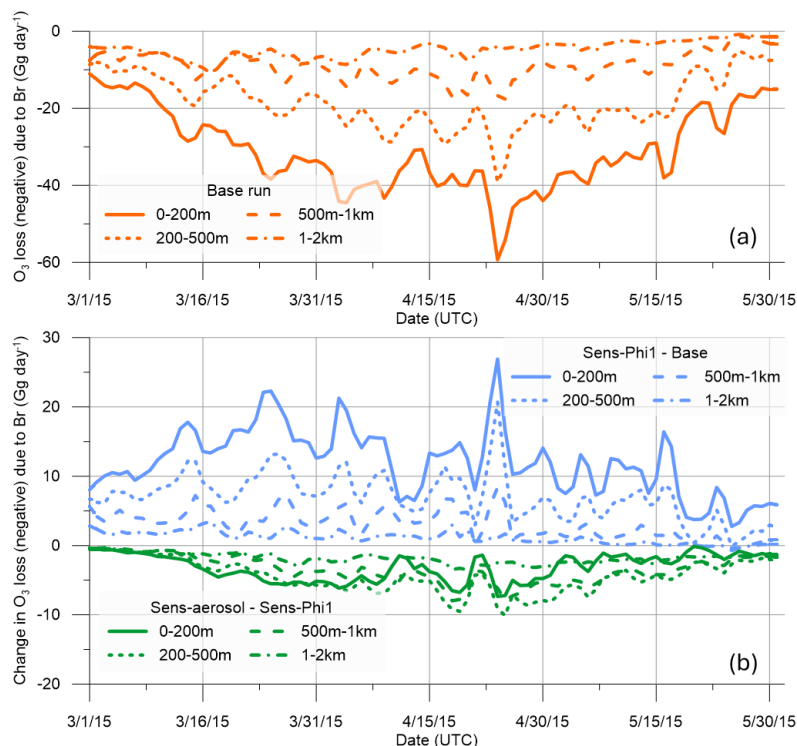
Figure 14. (a) Pan-Arctic (> 66.5°N) integrated daily net O_3 loss (negative) due to bromine chemistry over the lowest 2 km from the GEM-MACH base case run; **(b)** change in the pan-Arctic integrated daily net bromine-related O_3 loss due to reduction in Φ_1 (i.e., Sens-Phi1 vs. Base; positive for reduced O_3 loss or increase in O_3) and aerosol heterogeneous chemistry enhancement (Sens-aerosol vs. Sens-Phi1; negative for increased O_3 loss or decrease in O_3).

4.2 Impact of boreal wildfires on summertime Arctic O₃

920 To investigate the impact of northern boreal wildfire emissions on tropospheric ozone in the Arctic, the GEM-MACH base-case simulation was repeated with the wildfire emissions turned off within its pan-Arctic limited-area grid. Figure 15 compares the model-simulated July mean ozone concentration over the Arctic, with and without the wildfire emissions, at three model levels. The impact of wildfires is expected to have a large inter-annual variability due to the differences in characteristics of fire seasons and meteorological conditions each year (e.g., Magnussen and Taylor, 2012). In 2015 the Arctic was mostly

925 impacted by the wildfires in Alaska and northern Canada. Particularly, Alaska had a historically high number of fire events and acreage burnt for that fire season, with most of the fire activity concentrated in the late June to July period (Alaska Interagency Coordination Center, 2016). The model simulations show that the northern boreal wildfire emissions had a modest impact on tropospheric ozone concentration in 2015, most significantly in July. The monthly mean O_3 concentrations over the central Arctic are enhanced by $1 - 2$ ppbv at the surface due to northern boreal wildfires while the enhancement is higher at

930 elevations (e.g., ~ 900 and 850 hPa levels) by $3 - 4$ ppbv, representing a $5 - 10\%$ increase at the surface level and up to $10 - 20\%$ increase at the elevated levels. However, it is worth noting that the DEHM simulation showed pronounced elevated O_3 levels in the same area over northern Alaska extending into the Chukchi Sea and further into the central Arctic Ocean (See Fig. 2-2 (g) and (k)). This is consistent with the area impacted by the wildfires in Alaska. Also shown in Figure 15 is the excess (or enhancement) ratio $\Delta O_3/\Delta CO$, defined as the excess O_3 mixing ratio due to a particular source (wildfire, in this case) to the

935 increased CO from the same source, which is often used to characterize ozone production in smoke plumes (Jaffe and Wigder, 2012). Here ΔO_3 and ΔCO were evaluated from the modelled O_3 and CO concentrations with and without the wildfire emissions; a similar approach was used in Pfister et al. (2006) and Thomas et al. (2013). As expected, $\Delta O_3/\Delta CO$ values are small, ~ 0.02 ppbv/ppbv (surface) and ~ 0.04 ppbv/ppbv (elevated levels), over the fire regions in Alaska and the Canadian Northwest Territories, due to limited excess O_3 from photochemical production and large excess CO from fire emissions in

940 fresh plumes; the $\Delta O_3/\Delta CO$ values are considerably larger over the central Arctic, ~ 0.1 ppbv/ppbv (surface) and ~ 0.14 ppbv/ppbv (elevated levels), due to much lower ΔCO resulting from dilution during long-range transport, as well as continued O_3 production in aging plumes. The higher O_3 excess ratio at elevated levels compared to the surface (lowest model) level is consistent with the higher O_3 enhancement found at elevated levels in the Arctic due to the northern boreal wildfires. These regional enhancement ratio values may be compared with the wide range of $\Delta O_3/\Delta CO$ values reported from existing studies

945 for high-latitude boreal biomass burning plumes. For example, Jaffe and Wigder (2012) provided a summary of $\Delta O_3/\Delta CO$ estimated from observations by biome and plume age; for boreal and temperate regions, they reported $\Delta O_3/\Delta CO$ values ranging between 0.005 and 0.08 (average of 0.018 ppbv/ppbv) in fresh plumes ($\leq 1 - 2$ days), between 0.11 and 0.18 (average of 0.15 ppbv/ppbv) in plumes of age $2 - 5$ days, and between 0.035 and 0.59 (average of 0.22 ppbv/ppbv) in older plumes (age > 5 days). Thomas et al. (2013) found mean $\Delta O_3/\Delta CO$ values of 0.08 and 0.49 in fresh and aged biomass burning plumes (from

950 Canadian boreal forest fires), respectively, based on WRF-CHEM model simulations of the ARCTAS-B field campaign. Arnold et al. (2015) also found similar $\Delta O_3/\Delta CO$ values from the POLMIP model simulations, in the range of $0.039 - 0.196$

ppbv/ppbv for fresh fire plumes and 0.14 – 0.261 ppbv/ppbv for aged fire plumes. The July monthly $\Delta O_3/\Delta CO$ values found in this study over the North American boreal fire regions, 0.02 – 0.04 ppbv/ppbv, are consistent with the range of values found in previous studies for fresh boreal fire plumes, while the values over the central Arctic, 0.1 – 0.14 ppbv/ppbv, are somewhat

955   smaller than those previously reported values for aged boreal fire plumes. Note, however, here the excess ratios are evaluated based on monthly mean over a broad area while the previously reported values were mostly evaluated within plumes and for a short time period (e.g., duration of field campaign).
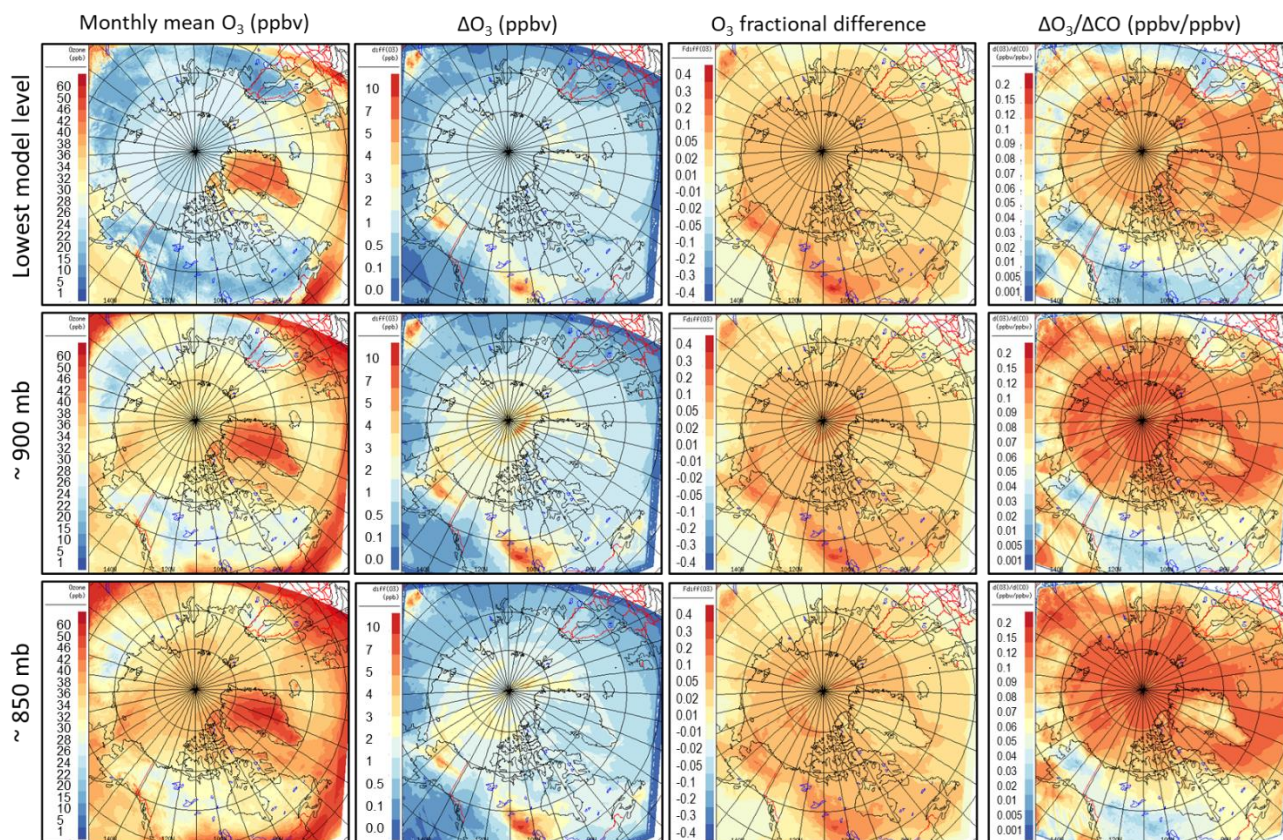
Figure 15. Impact of northern boreal wildfire emissions on Arctic lower tropospheric ozone (at 3 model levels: lowest – top, ~900 hPa –
960   middle, and ~850 hPa – bottom); leftmost column – 2015 July monthly mean ozone concentration simulated by GEM-MACH; second left column – difference in simulated ozone concentration (with wildfire – without wildfire); second right column – fractional difference (computed as (A-B)/0.5(A+B)); rightmost column – ΔO3/ΔCO enhancement ratio (see text).

Emissions from biomass burning can also lead to large-scale enhancement in high-latitude NO_y (e.g., Arnold et al., 2015).

Figure 16 shows the enhancement ratios (July monthly mean), $\Delta NO_y/\Delta CO$ and $\Delta PAN/\Delta CO$, evaluated from the GEM-MACH

965   simulations at several model levels (lowest and levels nearest to pressure levels, 900 and 700 hPa). At the lowest model level, higher $\Delta NO_y/\Delta CO$ values are found over the fire regions, while much lower $\Delta NO_y/\Delta CO$ values are found over the central Arctic due to the efficient removal of NO_y species due to dry deposition. Higher NO_y enhancement ratios over the central Arctic are found at elevated levels, highest (~8 pptv/ppbv) at the model level close to 700 hPa. Note that higher $\Delta NO_y/\Delta CO$

values are found over the Russian fire region compared to the North American fire region, indicating a more efficient NO_y

970   production in Russian fire plumes. This is likely due to the difference in fire emissions (e.g., NO_x emission factors used by the model) between the two regions. As mentioned in section 2.1.2, the GEM-MACH simulation used different data source for wildfire emissions over North America (CEFFPS) and outsides North America (FINN v1.5). PAN, a component of NO_y, is of particular interest as it serves as a reservoir for NO_x and can potentially contribute to O_3 formation in the Arctic from its thermal decomposition (Walker et al., 2012). The modelled PAN enhancement ratios (ΔPAN/ΔCO) due to boreal wildfires are

975   simulated to be ~3 – 4 pptv/ppbv over the North American boreal fire regions at the lowest model level, increasing with height to 6 – 7 pptv/ppbv near 700 hPa. These values are comparable to those deduced from aircraft measurements in boreal fire plumes during the ARCTAS-B campaign (Alvarado et al., 2010). Over the central Arctic, the PAN enhancement ratio has lower values at low altitudes compared to over the fire regions. In contrast, the ΔPAN/ΔCO values are significantly higher at more elevated levels (e.g. 700 hPa), similar to the case of NO_y. Also included in Figure 16 is the evaluated PAN-to-NO_y

980   enhancement ratio (ΔPAN/ΔNOy) from model simulations. As shown, ΔPAN/ΔNO_y ranges from 40% close to the surface to greater than 70% at 700 hPa level in the North American boreal fire region and downwind, indicating a significant portion of NO_y produced from the boreal fires being in the form of PAN. Over the Arctic, ΔPAN/ΔNO_y ranges from 20% near the surface to greater than 50% at upper levels. The smaller fraction of PAN at lower levels could be a result of PAN decomposition in releasing NO_x and contributing to O_3 formation over the Arctic (referring to the increased O_3 enhancement ratio over the Arctic

985   from the source region; see Figure 15, rightmost column).
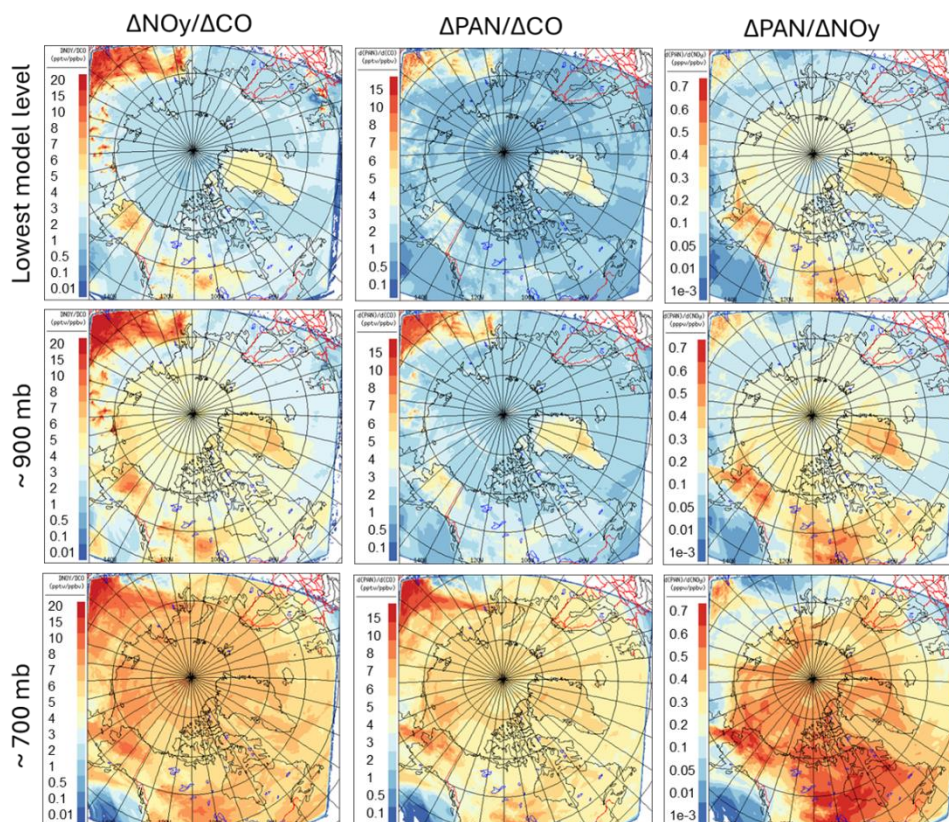
Figure 16. Modelled NO_y and PAN excess ratio, $\Delta NO_y/\Delta CO$ (left column) and $\Delta PAN/\Delta CO$ (middle column), as well as excess PAN-to-NO_y ratio, $\Delta PAN/\Delta NO_y$ (right column), for July 2015 (monthly mean), at 3 model levels (from top to bottom): lowest (surface), ~900 hPa, and ~700 hPa.

990 Figure 17 shows the modelled O_3 time series at Zeppelin and Summit sites for 2015 summer period, with and without the wildfire emissions. Also included are the corresponding modelled $PM_{2.5}$ time series as well as the aerosol absorption measurements available at these two sites. The time series show the main events of northern boreal wildfire plumes affecting the Arctic during July 2015, which are coincident with the high aerosol events indicated by the aerosol absorption measurements. The enhancements in ground level $PM_{2.5}$ from the fires are much more pronounced than in O_3. The enhancement

995 in $PM_{2.5}$ is largely driven by primary particulate matters (e.g., primary organic matters, crustal materials) directly emitted from the fires. O_3 is a secondary pollutant, and its formation depends upon the mix of its precursors in the fire plumes and the in-situ atmospheric reactivity. The model results indicate that northern boreal wildfires may raise the summertime background O_3 concentrations in the Arctic. However, the observed O_3 time series at Zeppelin and Summit show peak episodes during summer 2015 which could be associated with the transport of biomass burning plumes (Fig. 15); whilst the model did not fully

1000 simulate these peak events. This could be an indication of model underprediction of O_3 production in boreal fire plumes or that the long-range transport from lower latitudes is not being fully captured by the model's lateral boundary conditions.

However, there is also a possibility that the measured O_3 may be biased high at Summit under wildfire influenced conditions due to an instrument's VOC interference issue (Bernays et al., 2022; Long et al., 2021).
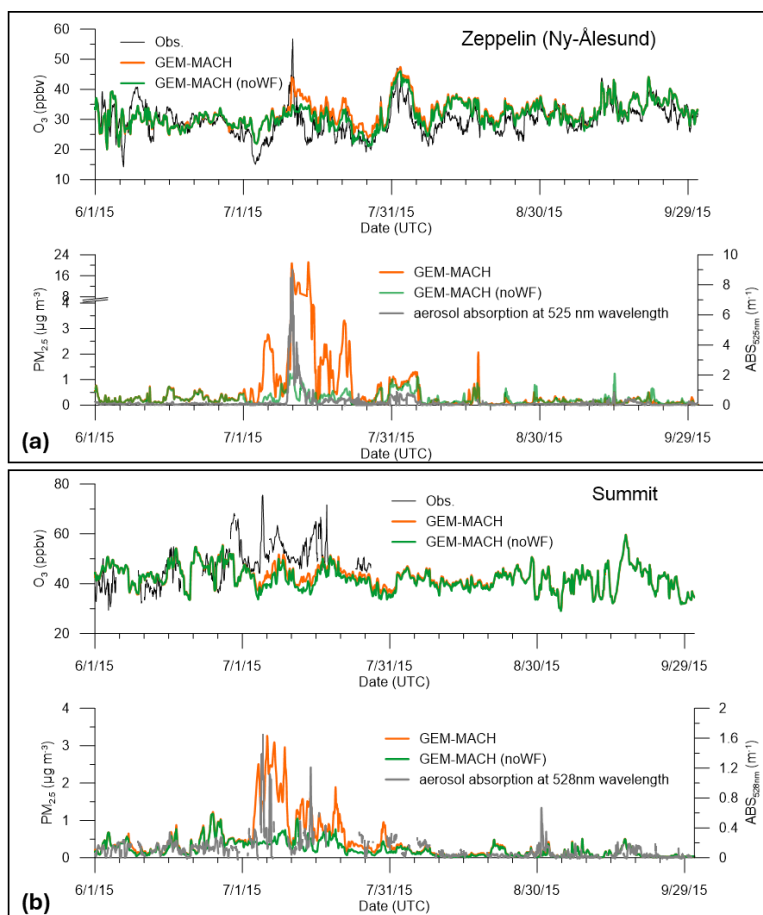
Figure 17. GEM-MACH Modelled O_3 and $PM_{2.5}$ time series (with and without wildfire emissions) at Zeppelin (a) and Summit (b) sites. Surface O_3 observations at the two sites are plotted in black. Also plotted along with modelled $PM_{2.5}$ is the observed aerosol absorption coefficient at the Zeppelin (@525nm) and Summit (@528nm) sites, obtained from an aethalometer and a multi angle absorption photometer (MAAP), respectively (accessed from EBAS (https://ebas.nilu.no) hosted by NILU; specifically, the use included data affiliated with the frameworks: GAW-WDCA, NOAA-ESRL).

Overall, the model simulations suggest that northern boreal wildfires do exert a modest impact on the Arctic tropospheric ozone by influencing the summertime background concentrations. The enhancement of O_3 concentration over the Arctic appears to be greater in the free troposphere than in the boundary layer; boreal wildfire plumes can often penetrate above the boundary layer where O_3 produced in fire plumes is less subjected to surface removal (dry deposition). Northern boreal wildfires also lead to the enhancement of NO_y in the Arctic. A significant portion of the NO_y in fire plumes is in the form of PAN, particularly at more elevated levels, which can play a role in O_3 production in the Arctic. It should be noted, however, due to the nature of the limited area model (LAM) configuration used in this study, that the model simulations discussed here

(with vs. without wildfire emissions) cannot capture the impact of Eurasian boreal wildfires as most of the Eurasian boreal fires in 2015 were located outside the GEM-MACH LAM domain.

4.3 Ozone tendency and budget analysis

1020 The GEM-MACH simulations incorporated diagnostics for ozone tendencies from each of the processes, (3-D) advection, vertical diffusion (including deposition at the lowest model layer), and chemistry. This was done to help understand how each of the processes influences the O_3 seasonal patterns in the Arctic. Figure 18 includes plots of the monthly averaged O_3 tendencies from each of the process operators in the GEM-MACH 2015 annual simulation for April and July at two model levels, the lowest and near 850 hPa. In April (spring), the O_3 in the Arctic lower atmosphere near the surface is strongly

1025 influenced by chemical loss driven by bromine explosions and ODEs, which is compensated by vertical diffusion (primarily) and advection, driven by the strong O_3 gradients (both vertical and horizontal) created by the chemical loss near the surface. In contrast, O_3 in the central Arctic at the elevated level (~850 hPa) is more strongly influenced by advection in spring with chemistry and vertical diffusion playing smaller roles. In July (summer), the net O_3 chemical tendency over the Arctic varies significantly spatially, from negative over large areas in the high Arctic (perhaps driven by loss through reactions mainly with

1030 HO_2, e.g. Wang et al., 2003) to positive (net production) at more polluted southerly locations, e.g., over northern Europe and northern Eurasia. There is an indication of net photochemical production of O_3 over the shipping channels along the southwestern coast of Greenland and the Canadian Atlantic coast. There is also considerable net O_3 chemical production over the central and northern coast of Alaska extending over the Beaufort Sea. SF.9 in the Supplement shows the July monthly net O_3 chemical tendency at various model levels from closest to the surface to near 700 hPa from both the GEM-MACH base

1035 annual simulation (with wildfires) and the GEM-MACH simulation without the wildfire emissions in the model LAM domain. The impact of boreal wildfires over central Alaska and northern Canada's Northwest Territories on O_3 production is evident. It is particularly interesting to note the potential interaction between the biomass burning plume and anthropogenic emissions of ozone precursors from Alaskan oil fields (Prudhoe Bay). The net O_3 chemical production extends further into the Arctic with the wildfires than without; the O_3 production in wildfire plumes also reaches higher altitudes than those from

1040 anthropogenic sources.
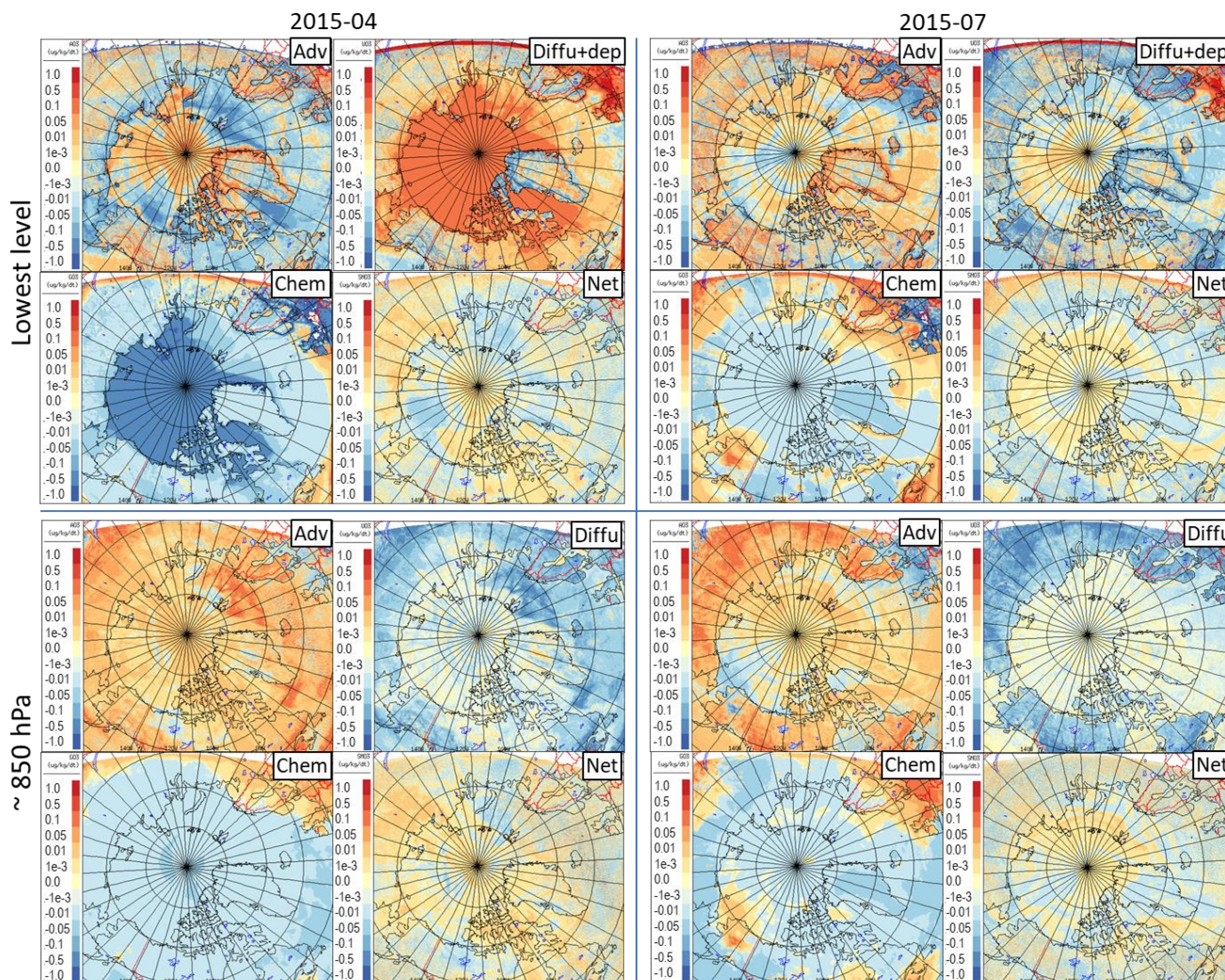
Figure 18. Monthly averaged O3 tendencies from each of the process operators in GEM-MACH, 3-D advection, vertical diffusion, and chemistry, as well as the net tendency for the month of April (left panels) and July (right panels) in 2015, at two model levels: lowest (top panels) and near 850 hPa (bottom); at the lowest model level, the vertical diffusion also includes dry deposition (as flux boundary condition).

1045   The pan-Arctic O3 budget for each month of 2015 is presented in Figure 19. It was computed by vertical integration of the

daily tendencies through specific depths of the atmospheric columns (from the surface) and then horizontal integration over

the area north of 66.5°N (Arctic Circle), given in gigagrams of O3 per day. The budgets for the lowest 200 m AGL, 1 km AGL,

and 4 km ASL are shown. Within the lowest 200 m of air across the Arctic Circle, the O3 budget is largely balanced off between

dry deposition (maximum in summer) and vertical diffusion outside the spring ODE season. During the ODE season, the

1050   budget is balanced between the combined loss through dry deposition and atmospheric chemistry and the gain from vertical

diffusion. Within the lowest 1 km of air, the O3 budget is largely balanced between the loss from dry deposition (throughout

the year) and chemistry (over spring) and O3 gains from advection (primarily) and vertical diffusion (much reduced compared

to over the lowest 200 m). Over a deeper layer (4 km asl), the O₃ budget is not always balanced, i.e., with non-zero O₃ net gain/loss. The processes contributing to the Arctic O₃ budget over the lowest 4 km (asl) are dry deposition and chemistry (both

1055   contributing to O₃ loss) and advection (contributing to O₃ gain). Also included in Fig.19 are the O₃ budgets computed from the GEM-MACH no-bromine (NoBr) run (shown for March to June) and the no-wildfire (NoWF) run (shown for July). It is evident that the O₃ chemical loss in the lowest 200m and up to 1 km is almost entirely due to bromine chemistry, with a minimal contribution from non-bromine chemistry (emerging during May – July). The O₃ non-bromine chemical loss occurs mainly above 1 km mainly in May through August. The impact of North American boreal wildfire on the Arctic O₃ budget is

1060   reflected in the reduced O₃ loss through chemistry (i.e., offset by the O₃ chemical production in wildfire plumes), most noticeable in the budget over the 4-km layer, indicating that most O₃ production from the North American wildfires is happening at elevated levels.
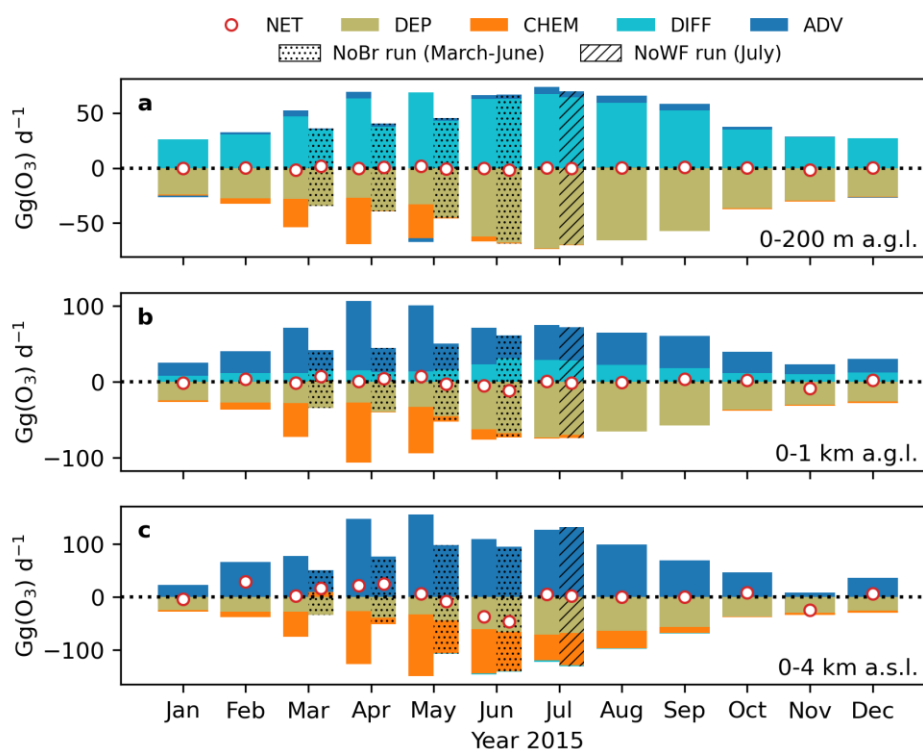
Figure 19. Pan-Arctic (> 66.5°N) integrated O₃ monthly budget for 2015, calculated for (a) the lowest 200 m AGL, (b) the lowest 1 km AGL, and (c) the lowest 4 km ASL. The net gain (NET, red circles) of O₃ over the domain of integration is determined by the balance

1065   between horizontal and vertical advection (ADV, blue bars), vertical diffusion (DIFF, light blue bars), photochemical reactions (CHEM, orange bars), and dry deposition (DEP, dark yellow bars). The O₃ budget from sensitivity runs is also shown by dotted (NoBr run between March and June) and hatched (NoWF run for July) bars again with red circles to denote the net gain of O₃.

While the springtime bromine explosion-induced O₃ loss mainly occurs within the lowest 1 km of air in the Arctic, it represents a considerable loss in O₃ tropospheric burden over the Arctic. The reductions in monthly mean partial O₃ columns due to

1070   snowpack bromine simulated by GEM-MACH is shown in SF.10 for the three spring months of 2015, including tropospheric column (surface to 400 hPa) and the lowest 4-km column (surface to 4 km ASL). The modelled snowpack bromine results in

up to 15% reductions in O_3 tropospheric column loading over the central Arctic (up to 30% reduction in the lowest 4-km O_3 column). These reductions amount to a 5-7% loss of pan-Arctic (> 66.5°N) tropospheric O_3 burden (8-12% loss of the O_3 burden over the lowest 4-km ASL of air).

5 Conclusions

In this study, we examine model simulations of Arctic lower tropospheric O_3 over the full year of 2015, conducted using two independent models, GEM-MACH and DEHM, configured at 15- and 25-km resolution, respectively, over the Arctic. Both models consider bromine chemistry with different process representations for the source term of bromine from snow in the Arctic: a snowpack-sourced mechanism in GEM-MACH (following Toyota et al., 2011) and a blowing-snow sourced mechanism in DEHM (following Yang et al., 2010). The annual model simulation results were compared with a suite of observations in the Arctic, including hourly observations from surface sites and mobile platforms (buoys and ship) and weekly (with some variability depending on the sites and the seasons) ozonesonde profiles, to evaluate the models' ability to simulate Arctic lower tropospheric O_3, particularly in capturing the seasonal variations and the key processes controlling these variations.

The model-observation comparisons show that both models are able to simulate Arctic lower tropospheric O_3 well, in capturing the overall surface O_3 seasonal cycle and synoptic scale variabilities, as well as the O_3 vertical profiles. Outside the spring O_3 depletion period, the behavior of the two models is remarkably similar to each other. The model simulated O_3 from the two models differs mostly during spring near the surface when GEM-MACH (with a representation of snowpack-sourced bromine) was able to capture most of the observed ODEs while DEHM (with a representation of blowing-snow soured bromine) simulated much fewer ODEs and of shorter duration and depth. As a result, GEM-MACH simulated O_3 showed distinctively different seasonal cycles between near the surface and aloft over central Arctic driven by the springtime ODEs, i.e., the O_3 spring minimum near the surface as opposed to the O_3 spring maximum aloft and at subarctic locations. The differing O_3 seasonal cycles between lower and upper levels simulated in GEM-MACH agree with the ozonesonde observations near the Arctic Ocean.

This study demonstrates that the springtime O_3 depletion process plays a central role in driving the O_3 seasonal cycle close to the surface in the Central Arctic, and that the ODEs are reproduced reasonably well with the representation of a snowpack bromine source mechanism (in the case of GEM-MACH), while bromine release from sea salt in the blowing snow mechanism alone (in the case of DEHM) does not produce sustained ODEs. The stronger impact of the snowpack-sourced bromine on modelled ODEs was also reported in recent studies (Marelle et al., 2021; Swanson et al., 2020). The snowpack-sourced mechanism seems to be essential in sustaining the continued bromine production under a variety of meteorological conditions, while the blowing-snow bromine source mechanism triggered by high wind conditions tends to be more episodic. This is consistent with observational evidence that the ODEs observed in the Arctic tend to occur during calm wind conditions favouring the snowpack bromine source mechanism to take effect in the surface air. The study also demonstrates that

atmospheric aerosols play an integral role in the Arctic springtime bromine explosions and ODEs through heterogeneous
1105   cycling of reactive bromine, particularly over a deeper vertical layer and at distance from the snowpack bromine source area.
This has implications for the potential role of Arctic haze aerosols that may play in the springtime ODEs, as indicated in
previous studies (e.g., Fan and Jacob, 1992).

Although GEM-MACH with the snowpack bromine source mechanism is able to simulate the observed ODEs reasonably well
in this study, there is a large uncertainty in the parameters employed by the parameterization due to lack of constraints by
1110   available laboratory or field experiments and the nature of the heuristic representation of highly complex multiphase processes
in snowpacks and in the atmosphere. This is demonstrated in this study through the sensitivity of modelled ODEs to the
snowpack bromine yield on FY sea ice (upon O_3 deposition) and the efficiency of heterogeneous cycling of reactive bromine
on atmospheric aerosol surfaces. Further investigation is needed to better constrain these parameters (and to better understand
the multi-phase processes controlling bromine cycle at the cryosphere-atmosphere interface).

1115   The present modelling study indicates that northern boreal wildfires can have an impact on the summertime Arctic tropospheric
O_3. The model simulations show an overall enhancement in the pan-Arctic O_3 concentration due to northern boreal wildfire
emissions during 2015; the enhancement is more significant at higher altitudes, consistent with higher O_3 excess ratio
($\Delta O_3/\Delta CO$) found there compared to near the surface. Wildfires also lead to an enhancement in NO_y in the Arctic, again more
significant at higher altitudes. A large portion of NO_y produced from the wildfire emissions is in the form of PAN, which is
1120   transported to the Arctic, particularly at higher altitudes, potentially contributing to O_3 production there. It should be noted
that wildfire activities are highly variable from year to year. With the current warming trend and increased northern boreal
wildfire activities, the impact of wildfires upon the Arctic tropospheric O_3 is expected to increase.

The O_3 budget analysis carried out in this study shows that the pan-Arctic lower tropospheric O_3 budget is largely balanced
off between pole-ward transport (advection), dry deposition, and chemistry (dominated by bromine chemistry during the spring
1125   period close to the surface and by HO_x chemistry at elevated levels). The springtime bromine-mediated ODEs contribute to 5-
7% of loss in the pan-Arctic tropospheric O_3 burden (and 8-12% loss of the pan-Arctic O_3 burden in the lowest 4 km of the
troposphere). While chemistry generally leads to an overall O_3 loss in the Arctic, net production of O_3 is found to occur locally
in ship plumes, downwind of oil and gas facilities in the Arctic, and in northern boreal wildfire plumes.

Overall, this study found that two independent chemical transport models, DEHM and GEM-MACH, configured at
1130   considerably higher resolution over the Arctic show better skills in capturing seasonal variation of surface and lower
tropospheric O_3 in the Arctic in comparison to the global models used in previous assessment studies. This may largely be
owing to their better skills in simulating synoptic systems at higher resolutions, implicating the important influence of synoptic
systems on poleward transport of pollutants. The important role of atmospheric transport in influencing the Arctic lower
tropospheric O_3 is also strongly evident from our O_3 budget analysis.

1135

Appendix 1 Model key features and configuration

	DEHM	GEM-MACH
Model type	Offline CTM (driven by WRF meteorology)	Regional online CTM
Horizontal grid and resolution	Hemispheric @ 75-km with nested Arctic grid @ 25-km; two-way nesting	Pan-Arctic LAM on a rotated lat-lon grid at 0.1375° (~15 km) resolution
Vertical coordinate and resolution	29 unevenly distributed layers, surface to 100 hPa, with the finest resolution in the atmospheric boundary layer: lowest model layer of ~20 m, with 3 – 4 model layers below the lowest 100 m.	Hybrid terrain-following sigma coordinate, 84 (unevenly spaced) levels (12 levels below 850 hPa) with a lid at 0.1 hPa; lowest momentum level at 20 m and lowest thermal level at 10 m.
Meteorology	WRF v4.1 driven by ERA5	GEM piloted by global GEM (GDPS); McTaggart-Cowan et al. (2019)
Chemistry mechanism	Strand and Hov (1994), with modifications based on chemical scheme in EMEP model (Simpson et al., 2012) and ACDEP model (Hertel et al., 1995), including bromine chemistry.	Gas-phase: ADOM-II (Stockwell and Lurmann, 1989: 42 gas-phase species and 114 reactions; based on Lurmann et al., 1986) + inorganic bromine chemistry (Toyota et al., 2011); Aqueous-phase: ADOM (inorganic sulfur chemistry; Venkatram et al., 1988; Fung et al., 1991) Atmospheric DMS oxidation (by OH and NO_3) (Ghahremaninezhad et al., 2019)
Bromine chemistry and source representation	Parameterized bromine source from blowing snow and open-ocean sea salt following Yang et al. (2008, 2010)	Simplified snowpack chemistry (Toyota et al., 2011) with termination due to seasonal snowmelt (Burd et al., 2017)
Aerosols	Bulk speciated aerosols, including SO4, NO3, NH4, EC, POM, SOA, and SS	Sectional (12 size bins between 0.01 and 40.96 um), chemically speciated (SO4, NO3, NH4, EC, POM, SOM, CM, SS), internally mixed
Dry deposition schemes	Gas and aerosol dry deposition as in EMEP models described in Simpson et al. (2012).	Gas: Wesley (1989) adapted as described in Makar et al. (2018) and Toyota et al. (2011) Aerosol: Emerson et al. (2020)

4000

10.5194/egusphere-2024-3750
2025-01-21
EGUsphere
journal article
en
Author(s) 2025. CC BY 4.0 License.

O_3 deposition (over ocean and sea ice)	Over sea-ice based on Simpson et al. (2012); over open sea based on Hertel et al. (1995); up to ~0.0005 m s^{-1} over North Atlantic (open water) and up to 0.0004 m s^{-1} over ice and snow in the Arctic.	Over the ocean: parameterized representation of iodide-mediated O3 dry deposition (Sarwar et al., 2015); Over ice: O3 dry deposition velocity set to 0.0001 m s^{-1} (Helmig et al., 2007)
Anthropogenic emissions	EMEP emissions for Europe, supplemented by 2015 ECLIPSE v6b global emissions; 2015 shipping emissions from STEAM	For 2015 simulations: 2016 US and 2015 Canadian inventories, supplemented by 2015 ECLIPSE v6b global emissions; 2015 MEIT Canadian marine shipping emissions
Biogenic emissions	MEGAN	BEIS v3.7 with BELD4 for NA and GLC2000 elsewhere
Wildfire emissions	GFAS from ECMWF	North America: Canadian Forest Fire Emissions Prediction System (CFFEPS, Chen et al., 2019 GMD); Outside North America: FINN v1.5; plume height estimate based on global satellite retrieval statistics (Val Martin et al., 2018)
Chemical LBC	Climatology for tropospheric O_3 (Logan, 1999).	Copernicus-CAMS reanalysis 6 hourly

Code and data availability:

All the observational data used in this study are available online (see Table 1). The surface O_3 monitoring data from the Arctic
1140 surface sites are available via the EBAS site (https://ebas-data.nilu.no/Default.aspx; last access 2024-11-13) hosted by NILU;
both the O-Buoy O_3 data and MAX-DOAS BrO data are available for download from the NSF Arctic Data Center
(https://arcticdata.io/catalog; last access 2024-11-23). Ozonesonde data can be downloaded from the World Ozone and
Ultrviolet Radiation Data Centre (WOUDC) hosted by Environment and Climate Change Canada (ECCC)
(https://www.woudc.org/about/data-policy.php; last access 2024-11-23) and NASA Network for Detection of Atmospheric
1145 Composition Change (NDACC) site (https://ndacc.larc.nasa.gov/data/use-agreement; last access 2024-11-23). The NETCARE
AWI/Polar-6 aircraft data are available from the Government of Canada Open Data portal
(https://search.open.canada.ca/opendata/; last access 2024-11-23). The GEM-MACH model data (monthly mean O_3 at three
model levels, lowest, nearest to 900 and 700 hPa) in NetCDF are available to download from the Zenodo site:
https://zenodo.org/records/14237307; other GEM-MACH model data are available upon request from the corresponding
1150 author Wanmin Gong (wanmin.gong@ec.gc.ca). The GEM-MACH-Arctic chemistry module code can be downloaded from

this Zenodo site: https://zenodo.org/records/14217327. The DEHM model code and data can be made available by contacting Jesper Heile Christensen (jc@envs.au.dk).

Author contribution:

WG designed the study with input from KT, SRB, UI, HS, JHC, ASL, RS, and YK. KT developed the bromine code employed in GEM-MACH-Arctic; KT and SRB implemented the code. DP provided the code for the Sarwar parameterization of iodine-mediated O_3 dry deposition over the ocean implemented in GEM-MACH-Arctic for this study. JZ and AL generated GEM-MACH anthropogenic emissions and meteorological piloting files for the study, respectively. GEM-MACH simulations were performed by SRB and WG. JHC was responsible for DEHM and provided DEHM simulation results. SRB, KT, and WG carried out the analysis. Observational data curation was provided by PE and IP (surface O_3 at Utqiaġvik, Summit, and Tiksi), SS (surface O_3 at Zeppelin and Tustervatn), MV (surface O_3 at Pallas), CN and HS (surface O_3 at Villum), JWH, PBS and TKK (O_3 from O-Buoys), YK (O_3 from R/V Mirai), WRS (BrO from O-Buoys and BARC), DWT (ozonsondes at Alert, Eureka, and Resolute), NJ (Scoresbysund ozonesonde), RK (Sodankylä ozonesonde), KM (Ny-Ålesund ozonesonde), RVM (homogenized ozonesonde data), and RMS (NETCARE Polar-6 O_3). WG wrote the manuscript with contributions from KT, HS, and JHC. All authors reviewed and edited the manuscript.

Competing Interests:

At least one of the (co-)authors is a member of the editorial board of Atmospheric Chemistry and Physics. The authors have no other competing interests to declare.

Acknowledgements:

The authors would like to acknowledge the various data centres (NILU/EBAS, NSF/Arctic Data Center, NASA/NDACC, ECCC/WOUDC) for access to the observational data used in this study. Peter von der Gathen is acknowledged for his long-time effort in creating and maintaining the Ny-Ålesund ozonesonde dataset. We acknowledge Patrick Sheridan and Peter Tunved for making the aerosol absorption measurements at Summit and Zeppelin, respectively, available. We are grateful to the managers, staff, and technicians at the various sites for their work in making the measurement data available, particularly, Karin Söderlund for Esrange surface O_3 data, Rune Keller and Bjørn Aaholm for Villum surface O_3 data. Gratitude is due to the Royal Danish Air Force and the Arctic Command for providing logistic support to Villum Research station and Christel Christoffersen, Bjarne Jensen and Martin Ole Bjært Sørensen are gratefully acknowledged for their technical support. WG, SRB, and KT would like to express their gratitude to the GEM-MACH development team at ECCC for technical support.

Financial Support:

Yugo Kanaya was supported by the KAKENHI grant no. 21H04933 and by the ArCS (Arctic Challenge for Sustainability; grant no. JPMXD1300000000) and ArCS II (Grant Number JPMXD1420318865) of the Ministry of Education, Culture, Sports, Science, and Technology of Japan. The research of Peter Effertz and Irina Petropavlovskikh was supported by a NOAA Cooperative Agreement with CIRES, NA17OAR4320101. Villum Foundation is gratefully acknowledged for financing the establishment of Villum Research Station (grant no. project no. VKR023001). The Danish EPA is acknowledged for

continuous funding of the ozone measurements at Villum Research Station during the years by means of Environmental
1185   Support to the Arctic.

References

Aaltonen, H., Pumpanen, J., Pihlatie, M., Hakola, H., Hellén, H., Kulmala, L., Vesala, T., and Bäck, J.: Boreal pine forest floor
biogenic volatile organic compound emissions peak in early summer and autumn, Spec. Issue Atmospheric Transp. Chem.
For. Ecosyst., 151, 682–691, https://doi.org/10.1016/j.agrformet.2010.12.010, 2011.

1190   Abbatt, J. P. D., Leaitch, W. R., Aliabadi, A. A., Bertram, A. K., Blanchet, J.-P., Boivin-Rioux, A., Bozem, H., Burkart, J.,
Chang, R. Y. W., Charette, J., Chaubey, J. P., Christensen, R. J., Cirisan, A., Collins, D. B., Croft, B., Dionne, J., Evans, G. J.,
Fletcher, C. G., Galí, M., Ghahreman, R., Girard, E., Gong, W., Gosselin, M., Gourdal, M., Hanna, S. J., Hayashida, H.,
Herber, A. B., Hesaraki, S., Hoor, P., Huang, L., Hussherr, R., Irish, V. E., Keita, S. A., Kodros, J. K., Köllner, F., Kolonjari,
F., Kunkel, D., Ladino, L. A., Law, K., Levasseur, M., Libois, Q., Liggio, J., Lizotte, M., Macdonald, K. M., Mahmood, R.,
1195   Martin, R. V., Mason, R. H., Miller, L. A., Moravek, A., Mortenson, E., Mungall, E. L., Murphy, J. G., Namazi, M., Norman,
A.-L., O'Neill, N. T., Pierce, J. R., Russell, L. M., Schneider, J., Schulz, H., Sharma, S., Si, M., Staebler, R. M., Steiner, N.
S., Thomas, J. L., von Salzen, K., Wentzell, J. J. B., Willis, M. D., Wentworth, G. R., Xu, J.-W., and Yakobi-Hancock, J. D.:
Overview paper: New insights into aerosol and climate in the Arctic, Atmos Chem Phys, 19, 2527–2560,
https://doi.org/10.5194/acp-19-2527-2019, 2019.

1200   Adams, J. W., Holmes, N. S., and Crowley, J. N.: Uptake and reaction of HOBr on frozen and dry NaCl/NaBr surfaces between
253 and 233 K, Atmos Chem Phys, 2, 79–91, https://doi.org/10.5194/acp-2-79-2002, 2002.

Alaska Interagency Coordination Center: 2015 Fire Season Weather Summary, Alaska Interagency Coordination Center,
Alaska, 2016.

Albert, M. R. and Shultz, E. F.: Snow and firn properties and air–snow transport processes at Summit, Greenland, AirSnowIce
1205   Interact. Arct. Results ALERT 2000 SUMMIT 2000, 36, 2789–2797, https://doi.org/10.1016/S1352-2310(02)00119-X, 2002.

Aliabadi, A. A., Thomas, J. L., Herber, A. B., Staebler, R. M., Leaitch, W. R., Schulz, H., Law, K. S., Marelle, L., Burkart, J.,
Willis, M. D., Bozem, H., Hoor, P. M., Köllner, F., Schneider, J., Levasseur, M., and Abbatt, J. P. D.: Ship emissions
measurement in the Arctic by plume intercepts of the Canadian Coast Guard icebreaker Amundsen from the Polar 6 aircraft
platform, Atmos Chem Phys, 16, 7899–7916, https://doi.org/10.5194/acp-16-7899-2016, 2016.

1210   Alvarado, M. J., Logan, J. A., Mao, J., Apel, E., Riemer, D., Blake, D., Cohen, R. C., Min, K.-E., Perring, A. E., Browne, E.
C., Wooldridge, P. J., Diskin, G. S., Sachse, G. W., Fuelberg, H., Sessions, W. R., Harrigan, D. L., Huey, G., Liao, J., Case-
Hanks, A., Jimenez, J. L., Cubison, M. J., Vay, S. A., Weinheimer, A. J., Knapp, D. J., Montzka, D. D., Flocke, F. M., Pollack,
I. B., Wennberg, P. O., Kurten, A., Crounse, J., Clair, J. M. St., Wisthaler, A., Mikoviny, T., Yantosca, R. M., Carouge, C. C.,
and Le Sager, P.: Nitrogen oxides and PAN in plumes from boreal fires during ARCTAS-B and their impact on ozone: an
1215   integrated analysis of aircraft and satellite observations, Atmos Chem Phys, 10, 9739–9760, https://doi.org/10.5194/acp-10-
9739-2010, 2010.

AMAP: AMAP Assessment 2021: Impacts of Short-lived Climate Forcers on Arctic Climate, Air Quality, and Human Health,
Arctic Monitoring and Assessment Programme (AMAP), Tromsø, Norway, 2021.

Angot, H., McErlean, K., Hu, L., Millet, D. B., Hueber, J., Cui, K., Moss, J., Wielgasz, C., Milligan, T., Ketcherside, D., Bret-
1220   Harte, M. S., and Helmig, D.: Biogenic volatile organic compound ambient mixing ratios and emission rates in the Alaskan
Arctic tundra, Biogeosciences, 17, 6219–6236, https://doi.org/10.5194/bg-17-6219-2020, 2020.

Archibald, A. T., Neu, J. L., Elshorbany, Y. F., Cooper, O. R., Young, P. J., Cox, R. A., Coyle, M., and Derwent, R. G.: Tropospheric Ozone Assessment Report: A critical review of changes in the tropospheric ozone burden and budget from 1850 to 2100, Elem Sci Anth, 8, 034, 2020.

1225 Arnold, S. R., Emmons, L. K., Monks, S. A., Law, K. S., Ridley, D. A., Turquety, S., Tilmes, S., Thomas, J. L., Bouarar, I., Flemming, J., Huijnen, V., Mao, J., Duncan, B. N., Steenrod, S., Yoshida, Y., Langner, J., and Long, Y.: Biomass burning influence on high-latitude tropospheric ozone and reactive nitrogen in summer 2008: a multi-model analysis based on POLMIP simulations, Atmos Chem Phys, 15, 6047–6068, https://doi.org/10.5194/acp-15-6047-2015, 2015.

Barrie, L. A.: Arctic air pollution: An overview of current knowledge, Atmos Envir, 20, https://doi.org/10.1016/0004-
1230 6981(86)90180-0, 1986.

Barrie, L. A., Bottenheim, J. W., Schnell, R. C., Crutzen, P. J., and Rasmussen, R. A.: Ozone destruction and photochemical reactions at polar sunrise in the lower Arctic atmosphere, Nature, 334, 138–141, https://doi.org/10.1038/334138a0, 1988.

Barrie, L. A., Yi, Y., Leaitch, W. R., Lohmann, U., Kasibhatla, P., Roelofs, G.-J., Wilson, J., Mcgovern, F., Benkovitz, C., Méliéres, M. A., Law, K., Prospero, J., Kritz, M., Bergmann, D., Bridgeman, C., Chin, M., Christensen, J., Easter, R., Feichter,
1235 J., Land, C., Jeuken, A., Kjellström, E., Koch, D., and Rasch, P.: A comparison of large-scale atmospheric sulphate aerosol models (COSAM): overview and highlights, Tellus B Chem. Phys. Meteorol., https://doi.org/10.3402/tellusb.v53i5.16642, 2001.

Benavent, N., Mahajan, A. S., Li, Q., Cuevas, C. A., Schmale, J., Angot, H., Jokinen, T., Quéléver, L. L. J., Blechschmidt, A.-M., Zilker, B., Richter, A., Serna, J. A., Garcia-Nieto, D., Fernandez, R. P., Skov, H., Dumitrascu, A., Simões Pereira, P.,
1240 Abrahamsson, K., Bucci, S., Duetsch, M., Stohl, A., Beck, I., Laurila, T., Blomquist, B., Howard, D., Archer, S. D., Bariteau, L., Helmig, D., Hueber, J., Jacobi, H.-W., Posman, K., Dada, L., Daellenbach, K. R., and Saiz-Lopez, A.: Substantial contribution of iodine to Arctic ozone destruction, Nat. Geosci., 15, 770–773, https://doi.org/10.1038/s41561-022-01018-w, 2022.

Berg, T., Sekkesæter, S., Steinnes, E., Valdal, A.-K., and Wibetoe, G.: Springtime depletion of mercury in the European Arctic
1245 as observed at Svalbard, Pathw. Process. Mercury Environ. Sel. Pap. Present. Sixth Int. Conf. Mercury Glob. Pollut. Minamata Jpn. Oct 15-19 2001, 304, 43–51, https://doi.org/10.1016/S0048-9697(02)00555-7, 2003.

Bergström, R., Denier van der Gon, H. A. C., Prévôt, A. S. H., Yttri, K. E., and Simpson, D.: Modelling of organic aerosols over Europe (2002–2007) using a volatility basis set (VBS) framework: application of different assumptions regarding the formation of secondary organic aerosol, Atmos Chem Phys, 12, 8499–8527, https://doi.org/10.5194/acp-12-8499-2012, 2012.

1250 Bernays, N., Jaffe, D. A., Petropavlovskikh, I., and Effertz, P.: Comment on "Comparison of ozone measurement methods in biomass burning smoke: an evaluation under field and laboratory conditions" by Long et al. (2021), Atmos Meas Tech, 15, 3189–3192, https://doi.org/10.5194/amt-15-3189-2022, 2022.

Bottenheim, J. W. and Chan, E.: A trajectory study into the origin of spring time Arctic boundary layer ozone depletion, J. Geophys. Res. Atmospheres, 111, https://doi.org/10.1029/2006JD007055, 2006.

1255 Bottenheim, J. W., Netcheva, S., Morin, S., and Nghiem, S. V.: Ozone in the boundary layer air over the Arctic Ocean: measurements during the TARA transpolar drift 2006–2008, Atmos Chem Phys, 9, 4545–4557, https://doi.org/10.5194/acp-9-4545-2009, 2009.

Bozem, H., Hoor, P., Kunkel, D., Köllner, F., Schneider, J., Herber, A., Schulz, H., Leaitch, W. R., Aliabadi, A. A., Willis, M. D., Burkart, J., and Abbatt, J. P. D.: Characterization of transport regimes and the polar dome during Arctic spring and summer
1260 using in situ aircraft measurements, Atmos Chem Phys, 19, 15049–15071, https://doi.org/10.5194/acp-19-15049-2019, 2019.

Brandt, J., Silver, J. D., Frohn, L. M., Geels, C., Gross, A., Hansen, A. B., Hansen, K. M., Hedegaard, G. B., Skjøth, C. A., Villadsen, H., Zare, A., and Christensen, J. H.: An integrated model study for Europe and North America using the Danish Eulerian Hemispheric Model with focus on intercontinental transport of air pollution, AQMEII Int. Initiat. Eval. Reg.-Scale Air Qual. Models - Phase 1, 53, 156–176, https://doi.org/10.1016/j.atmosenv.2012.01.011, 2012.

1265 Burd, J. A., Peterson, P. K., Nghiem, S. V., Perovich, D. K., and Simpson, W. R.: Snowmelt onset hinders bromine monoxide heterogeneous recycling in the Arctic, J. Geophys. Res. Atmospheres, 122, 8297–8309, https://doi.org/10.1002/2017JD026906, 2017.

Charron, M., Polavarapu, S., Buehner, M., Vaillancourt, P. A., Charette, C., Roch, M., Morneau, J., Garand, L., Aparicio, J. M., MacPherson, S., Pellerin, S., St-James, J., and Heilliette, S.: The Stratospheric Extension of the Canadian Global 1270 Deterministic Medium-Range Weather Forecasting System and Its Impact on Tropospheric Forecasts, Mon. Weather Rev., 140, 1924–1944, https://doi.org/10.1175/MWR-D-11-00097.1, 2012.

Christensen, J. H.: The Danish eulerian hemispheric model — a three-dimensional air pollution model used for the arctic, Atmos. Environ., 31, 4169–4191, https://doi.org/10.1016/S1352-2310(97)00264-1, 1997.

Christensen, J. H., Brandt, J., Frohn, L. M., and Skov, H.: Modelling of Mercury in the Arctic with the Danish Eulerian 1275 Hemispheric Model, Atmos Chem Phys, 4, 2251–2257, https://doi.org/10.5194/acp-4-2251-2004, 2004.

Christiansen, B., Jepsen, N., Kivi, R., Hansen, G., Larsen, N., and Korsholm, U. S.: Trends and annual cycles in soundings of Arctic tropospheric ozone, Atmos Chem Phys, 17, 9347–9364, https://doi.org/10.5194/acp-17-9347-2017, 2017.

Clifton, O. E., Fiore, A. M., Massman, W. J., Baublitz, C. B., Coyle, M., Emberson, L., Fares, S., Farmer, D. K., Gentine, P., Gerosa, G., Guenther, A. B., Helmig, D., Lombardozzi, D. L., Munger, J. W., Patton, E. G., Pusede, S. E., Schwede, D. B., 1280 Silva, S. J., Sörgel, M., Steiner, A. L., and Tai, A. P. K.: Dry Deposition of Ozone Over Land: Processes, Measurement, and Modeling, Rev. Geophys., 58, e2019RG000670, https://doi.org/10.1029/2019RG000670, 2020.

Clifton, O. E., Schwede, D., Hogrefe, C., Bash, J. O., Bland, S., Cheung, P., Coyle, M., Emberson, L., Flemming, J., Fredj, E., Galmarini, S., Ganzeveld, L., Gazetas, O., Goded, I., Holmes, C. D., Horváth, L., Huijnen, V., Li, Q., Makar, P. A., Mammarella, I., Manca, G., Munger, J. W., Pérez-Camanyo, J. L., Pleim, J., Ran, L., San Jose, R., Silva, S. J., Staebler, R., 1285 Sun, S., Tai, A. P. K., Tas, E., Vesala, T., Weidinger, T., Wu, Z., and Zhang, L.: A single-point modeling approach for the intercomparison and evaluation of ozone dry deposition across chemical transport models (Activity 2 of AQMEII4), Atmos Chem Phys, 23, 9911–9961, https://doi.org/10.5194/acp-23-9911-2023, 2023.

Côté, J., Gravel, S., Méthot, A., Patoine, A., Roch, M., and Staniforth, A.: The Operational CMC–MRB Global Environmental Multiscale (GEM) Model. Part I: Design Considerations and Formulation, Mon. Weather Rev., 126, 1373–1395, 1290 https://doi.org/10.1175/1520-0493(1998)126<1373:TOCMGE>2.0.CO;2, 1998a.

Côté, J., Desmarais, J.-G., Gravel, S., Méthot, A., Patoine, A., Roch, M., and Staniforth, A.: The Operational CMC–MRB Global Environmental Multiscale (GEM) Model. Part II: Results, Mon. Weather Rev., 126, 1397–1418, https://doi.org/10.1175/1520-0493(1998)126<1397:TOCMGE>2.0.CO;2, 1998b.

Custard, K. D., Raso, A. R. W., Shepson, P. B., Staebler, R. M., and Pratt, K. A.: Production and Release of Molecular Bromine 1295 and Chlorine from the Arctic Coastal Snowpack, ACS Earth Space Chem., 1, 142–151, https://doi.org/10.1021/acsearthspacechem.7b00014, 2017.

Dekhtyareva, A., Holmén, K., Maturilli, M., Hermansen, O., and Graversen, R.: Effect of seasonal mesoscale and microscale meteorological conditions in Ny-Ålesund on results of monitoring of long-range transported pollution, Polar Res., 37, 1508196, https://doi.org/10.1080/17518369.2018.1508196, 2018.

1300 Eckhardt, S., Quennehen, B., Olivié, D. J. L., Berntsen, T. K., Cherian, R., Christensen, J. H., Collins, W., Crepinsek, S., Daskalakis, N., Flanner, M., Herber, A., Heyes, C., Hodnebrog, Ø., Huang, L., Kanakidou, M., Klimont, Z., Langner, J., Law, K. S., Lund, M. T., Mahmood, R., Massling, A., Myriokefalitakis, S., Nielsen, I. E., Nøjgaard, J. K., Quaas, J., Quinn, P. K., Raut, J.-C., Rumbold, S. T., Schulz, M., Sharma, S., Skeie, R. B., Skov, H., Uttal, T., von Salzen, K., and Stohl, A.: Current model capabilities for simulating black carbon and sulfate concentrations in the Arctic atmosphere: a multi-model evaluation
1305 using a comprehensive measurement data set, Atmos Chem Phys, 15, 9413–9433, https://doi.org/10.5194/acp-15-9413-2015, 2015.

Emerson, E. W., Hodshire, A. L., DeBolt, H. M., Bilsback, K. R., Pierce, J. R., McMeeking, G. R., and Farmer, D. K.: Revisiting particle dry deposition and its role in radiative effect estimates, Proc. Natl. Acad. Sci., 117, 26076–26082, https://doi.org/10.1073/pnas.2014761117, 2020.

1310 Eneroth, K., Holmén, K., Berg, T., Schmidbauer, N., and Solberg, S.: Springtime depletion of tropospheric ozone, gaseous elemental mercury and non-methane hydrocarbons in the European Arctic, and its relation to atmospheric transport, Atmos. Environ., 41, 8511–8526, https://doi.org/10.1016/j.atmosenv.2007.07.008, 2007.

Falk, S. and Sinnhuber, B.-M.: Polar boundary layer bromine explosion and ozone depletion events in the chemistry–climate model EMAC v2.52: implementation and evaluation of AirSnow algorithm, Geosci Model Dev, 11, 1115–1131,
1315 https://doi.org/10.5194/gmd-11-1115-2018, 2018.

Fan, S.-M. and Jacob, D. J.: Surface ozone depletion in Arctic spring sustained by bromine reactions on aerosols, Nature, 359, 522–524, https://doi.org/10.1038/359522a0, 1992.

Fernandez, R. P., Carmona-Balea, A., Cuevas, C. A., Barrera, J. A., Kinnison, D. E., Lamarque, J.-F., Blaszczak-Boxe, C., Kim, K., Choi, W., Hay, T., Blechschmidt, A.-M., Schönhardt, A., Burrows, J. P., and Saiz-Lopez, A.: Modeling the Sources
1320 and Chemistry of Polar Tropospheric Halogens (Cl, Br, and I) Using the CAM-Chem Global Chemistry-Climate Model, J. Adv. Model. Earth Syst., 11, 2259–2289, https://doi.org/10.1029/2019MS001655, 2019.

Fernandez, R. P., Berná, L., Tomazzeli, O. G., Mahajan, A. S., Li, Q., Kinnison, D. E., Wang, S., Lamarque, J.-F., Tilmes, S., Skov, H., Cuevas, C. A., and Saiz-Lopez, A.: Arctic halogens reduce ozone in the northern mid-latitudes, Proc. Natl. Acad. Sci., 121, e2401975121, https://doi.org/10.1073/pnas.2401975121, 2024.

1325 Foster, K. L., Plastridge, R. A., Bottenheim, J. W., Shepson, P. B., Finlayson-Pitts, B. J., and Spicer, C. W.: The Role of Br2 and BrCl in Surface Ozone Destruction at Polar Sunrise, Science, 291, 471–474, https://doi.org/10.1126/science.291.5503.471, 2001.

Frey, M. M., Norris, S. J., Brooks, I. M., Anderson, P. S., Nishimura, K., Yang, X., Jones, A. E., Nerentorp Mastromonaco, M. G., Jones, D. H., and Wolff, E. W.: First direct observation of sea salt aerosol production from blowing snow above sea
1330 ice, Atmos Chem Phys, 20, 2549–2578, https://doi.org/10.5194/acp-20-2549-2020, 2020.

Frieß, U., Sihler, H., Sander, R., Pöhler, D., Yilmaz, S., and Platt, U.: The vertical distribution of BrO and aerosols in the Arctic: Measurements by active and passive differential optical absorption spectroscopy, J. Geophys. Res. Atmospheres, 116, https://doi.org/10.1029/2011JD015938, 2011.

Ghahreman, R., Gong, W., Galí, M., Norman, A.-L., Beagley, S. R., Akingunola, A., Zheng, Q., Lupu, A., Lizotte, M.,
1335 Levasseur, M., and Leaitch, W. R.: Dimethyl sulfide and its role in aerosol formation and growth in the Arctic summer – a modelling study, Atmos Chem Phys, 19, 14455–14476, https://doi.org/10.5194/acp-19-14455-2019, 2019.

Gong, S. L., Barrie, L. A., Blanchet, J.-P., von Salzen, K., Lohmann, U., Lesins, G., Spacek, L., Zhang, L. M., Girard, E., Lin, H., Leaitch, R., Leighton, H., Chylek, P., and Huang, P.: Canadian Aerosol Module: A size-segregated simulation of

atmospheric aerosol processes for climate and air quality models 1. Module development, J. Geophys. Res. Atmospheres, 108,
1340   AAC 3-1, https://doi.org/10.1029/2001JD002002, 2003.

Gong, W., Dastoor, A. P., Bouchet, V. S., Gong, S., Makar, P. A., Moran, M. D., Pabla, B., Ménard, S., Crevier, L.-P.,
Cousineau, S., and Venkatesh, S.: Cloud processing of gases and aerosols in a regional air quality model (AURAMS),
Atmospheric Res., 82, 248–275, https://doi.org/10.1016/j.atmosres.2005.10.012, 2006.

Gong, W., Makar, P. A., Zhang, J., Milbrandt, J., Gravel, S., Hayden, K. L., Macdonald, A. M., and Leaitch, W. R.: Modelling
1345   aerosol–cloud–meteorology interaction: A case study with a fully coupled air quality model (GEM-MACH), Atmos. Environ.,
115, 695–715, https://doi.org/10.1016/j.atmosenv.2015.05.062, 2015.

Gong, W., Beagley, S. R., Cousineau, S., Sassi, M., Munoz-Alpizar, R., Ménard, S., Racine, J., Zhang, J., Chen, J., Morrison,
H., Sharma, S., Huang, L., Bellavance, P., Ly, J., Izdebski, P., Lyons, L., and Holt, R.: Assessing the impact of shipping
emissions on air pollution in the Canadian Arctic and northern regions: current and future modelled scenarios, Atmos Chem
1350   Phys, 18, 16653–16687, https://doi.org/10.5194/acp-18-16653-2018, 2018.

Gong, W., Beagley, S., and Ghahreman, R.: Sources and Processes Affecting Air Pollution in the Arctic and Northern High
Latitudes—A Modelling Study, in: Air Pollution Modeling and its Application XXVIII, Cham, 97–105, 2022.

Gong, W., Beagley, S. R., Ghahreman, R., Sharma, S., Huang, L., Quinn, P. K., Massling, A., Pernov, J. B., Skov, H., Cal-
zolai, G., Traversi, R., Aas, W., Yttri, K. E., Vestenius, M., Makkonen, U., Kivekas, N., Kulmala, M., Aalto, P., and Fiebig,
1355   M.: Modelling Arctic atmospheric aerosols: representation of aerosol processing by ice and mixed-phase clouds, in: Air
Pollution Modeling and Its Application XXIX, 8pp, 2024.

Gryning, S.-E., Batchvarova, E., Floors, R., Münkel, C., Sørensen, L. L., and Skov, H.: Observed aerosol-layer depth at Station
Nord in the high Arctic, Int. J. Climatol., 43, 3247–3263, https://doi.org/10.1002/joc.8027, 2023.

Halfacre, J. W., Knepp, T. N., Shepson, P. B., Thompson, C. R., Pratt, K. A., Li, B., Peterson, P. K., Walsh, S. J., Simpson,
1360   W. R., Matrai, P. A., Bottenheim, J. W., Netcheva, S., Perovich, D. K., and Richter, A.: Temporal and spatial characteristics
of ozone depletion events from measurements in the Arctic, Atmos Chem Phys, 14, 4875–4894, https://doi.org/10.5194/acp-
14-4875-2014, 2014.

Hansen, K. M., Christensen, J. H., Brandt, J., Frohn, L. M., Geels, C., Skjøth, C. A., and Li, Y.-F.: Modeling short-term
variability of α-hexachlorocyclohexane in Northern Hemispheric air, J. Geophys. Res. Atmospheres, 113,
1365   https://doi.org/10.1029/2007JD008492, 2008.

Hanson, D. R., Ravishankara, A. R., and Lovejoy, E. R.: Reaction of BrONO2 with H2O on submicron sulfuric acid aerosol
and the implications for the lower stratosphere, J. Geophys. Res. Atmospheres, 101, 9063–9069,
https://doi.org/10.1029/96JD00347, 1996.

Hatakka, J., Aalto, T., Aaltonen, V., Aurela, M., Hakola, H., Komppula, M., T. Laurila, Lihavainen, H., Paatero, J., Salminen,
1370   K., and Viisanen, Y.: Overview of the atmospheric research activities and results at Pallas GAW station, Boreal Environ. Res.,
8, 365–383, 2003.

Hausmann, M. and Platt, U.: Spectroscopic measurement of bromine oxide and ozone in the high Arctic during Polar Sunrise
Experiment 1992, J. Geophys. Res. Atmospheres, 99, 25399–25413, https://doi.org/10.1029/94JD01314, 1994.

He, P., Bian, L., Zheng, X., Yu, J., Sun, C., Ye, P., and Xie, Z.: Observation of surface ozone in the marine boundary layer
1375   along a cruise through the Arctic Ocean: From offshore to remote, Atmospheric Res., 169, 191–198,
https://doi.org/10.1016/j.atmosres.2015.10.009, 2016.

Heidam, N. Z., Christensen, J., Wåhlin, P., and Skov, H.: Arctic atmospheric contaminants in NE Greenland: levels, variations, origins, transport, transformations and trends 1990–2001, Contam. Greenl. Environ. Update, 331, 5–28, https://doi.org/10.1016/j.scitotenv.2004.03.033, 2004.

1380   Helmig, D., Ganzeveld, L., Butler, T., and Oltmans, S. J.: The role of ozone atmosphere-snow gas exchange on polar, boundary-layer tropospheric ozone – a review and sensitivity analysis, Atmos Chem Phys, 7, 15–30, https://doi.org/10.5194/acp-7-15-2007, 2007.

Helmig, D., Cohen, L. D., Bocquet, F., Oltmans, S., Grachev, A., and Neff, W.: Spring and summertime diurnal surface ozone fluxes over the polar snow at Summit, Greenland, Geophys. Res. Lett., 36, https://doi.org/10.1029/2008GL036549, 2009.

1385   Herrmann, M., Sihler, H., Frieß, U., Wagner, T., Platt, U., and Gutheil, E.: Time-dependent 3D simulations of tropospheric ozone depletion events in the Arctic spring using the Weather Research and Forecasting model coupled with Chemistry (WRF-Chem), Atmos Chem Phys, 21, 7611–7638, https://doi.org/10.5194/acp-21-7611-2021, 2021.

Hertel, O., Christensen, J., Runge, E. H., Asman, W. A. H., Berkowicz, R., Hovmand, M. F., and Hov, Ø.: Development and testing of a new variable scale air pollution model—ACDEP, Atmos. Environ., 29, 1267–1290, https://doi.org/10.1016/1352-1390   2310(95)00067-9, 1995.

Hirdman, D., Sodemann, H., Eckhardt, S., Burkhart, J. F., Jefferson, A., Mefford, T., Quinn, P. K., Sharma, S., Ström, J., and Stohl, A.: Source identification of short-lived air pollutants in the Arctic using statistical analysis of measurement data and particle dispersion model output, Atmos Chem Phys, 10, 669–693, https://doi.org/10.5194/acp-10-669-2010, 2010.

Hole, L. R., Christensen, J. H., Ruoho-Airola, T., Tørseth, K., Ginzburg, V., and Glowacki, P.: Past and future trends in 1395   concentrations of sulphur and nitrogen compounds in the Arctic, Atmos. Environ., 43, 928–939, https://doi.org/10.1016/j.atmosenv.2008.10.043, 2009.

Huang, J. and Jaeglé, L.: Wintertime enhancements of sea salt aerosol in polar regions consistent with a sea ice source from blowing snow, Atmos Chem Phys, 17, 3699–3712, https://doi.org/10.5194/acp-17-3699-2017, 2017.

Huang, J., Jaeglé, L., Chen, Q., Alexander, B., Sherwen, T., Evans, M. J., Theys, N., and Choi, S.: Evaluating the impact of 1400   blowing-snow sea salt aerosol on springtime BrO and O3 in the Arctic, Atmos Chem Phys, 20, 7335–7358, https://doi.org/10.5194/acp-20-7335-2020, 2020.

Huang, L., Gong, S. L., Jia, C. Q., and Lavoué, D.: Relative contributions of anthropogenic emissions to black carbon aerosol in the Arctic, J. Geophys. Res. Atmospheres, 115, https://doi.org/10.1029/2009JD013592, 2010.

Inness, A., Ades, M., Agustí-Panareda, A., Barré, J., Benedictow, A., Blechschmidt, A.-M., Dominguez, J. J., Engelen, R., 1405   Eskes, H., Flemming, J., Huijnen, V., Jones, L., Kipling, Z., Massart, S., Parrington, M., Peuch, V.-H., Razinger, M., Remy, S., Schulz, M., and Suttie, M.: The CAMS reanalysis of atmospheric composition, Atmos Chem Phys, 19, 3515–3556, https://doi.org/10.5194/acp-19-3515-2019, 2019.

Jacobi, H.-W., Morin, S., and Bottenheim, J. W.: Observation of widespread depletion of ozone in the springtime boundary layer of the central Arctic linked to mesoscale synoptic conditions, J. Geophys. Res. Atmospheres, 115, 1410   https://doi.org/10.1029/2010JD013940, 2010.

Jaeglé, L., Shah, V., Thornton, J. A., Lopez-Hilfiker, F. D., Lee, B. H., McDuffie, E. E., Fibiger, D., Brown, S. S., Veres, P., Sparks, T. L., Ebben, C. J., Wooldridge, P. J., Kenagy, H. S., Cohen, R. C., Weinheimer, A. J., Campos, T. L., Montzka, D. D., Digangi, J. P., Wolfe, G. M., Hanisco, T., Schroder, J. C., Campuzano-Jost, P., Day, D. A., Jimenez, J. L., Sullivan, A. P., Guo, H., and Weber, R. J.: Nitrogen Oxides Emissions, Chemistry, Deposition, and Export Over the Northeast United States

1415 During the WINTER Aircraft Campaign, J. Geophys. Res. Atmospheres, 123, 12,368-12,393, https://doi.org/10.1029/2018JD029133, 2018.

Jaffe, D. A. and Wigder, N. L.: Ozone production from wildfires: A critical review, Atmos. Environ., 51, 1–10, https://doi.org/10.1016/j.atmosenv.2011.11.063, 2012.

Jiang, W.: Instantaneous secondary organic aerosol yields and their comparison with overall aerosol yields for aromatic and
1420 biogenic hydrocarbons, Atmos. Environ., 37, 5439–5444, https://doi.org/10.1016/j.atmosenv.2003.09.018, 2003.

Jones, A. E., Anderson, P. S., Begoin, M., Brough, N., Hutterli, M. A., Marshall, G. J., Richter, A., Roscoe, H. K., and Wolff, E. W.: BrO, blizzards, and drivers of polar tropospheric ozone depletion events, Atmospheric Chem. Phys., 9, 4639–4652, https://doi.org/10.5194/acp-9-4639-2009, 2009.

Jonson, J. E. and Isaksen, I. S. A.: Tropospheric ozone chemistry. The impact of cloud chemistry, J. Atmospheric Chem., 16,
1425 99–122, https://doi.org/10.1007/BF00702781, 1993.

Junninen, H., Ahonen, L., Bianchi, F., Quéléver, L., Schallhart, S., Dada, L., Manninen, H. E., Leino, K., Lampilahti, J., Buenrostro Mazon, S., Rantala, P., Räty, M., Kontkanen, J., Negri, S., Aliaga, D., Garmash, O., Alekseychik, P., Lipp, H., Tamme, K., Levula, J., Sipilä, M., Ehn, M., Worsnop, D., Zilitinkevich, S., Mammarella, I., Rinne, J., Vesala, T., Petäjä, T., Kerminen, V.-M., and Kulmala, M.: Terpene emissions from boreal wetlands can initiate stronger atmospheric new particle
1430 formation than boreal forests, Commun. Earth Environ., 3, 93, https://doi.org/10.1038/s43247-022-00406-9, 2022.

Kaiser, J. W., Heil, A., Andreae, M. O., Benedetti, A., Chubarova, N., Jones, L., Morcrette, J.-J., Razinger, M., Schultz, M. G., Suttie, M., and van der Werf, G. R.: Biomass burning emissions estimated with a global fire assimilation system based on observed fire radiative power, Biogeosciences, 9, 527–554, https://doi.org/10.5194/bg-9-527-2012, 2012.

Kämäri, J., Joki-Heiskala, P., Christensen, J., Degermann, E., Derome, J., Hoff, R., and Kahkonen, A. M.: Acidifying
1435 pollutants, Arctic haze, and acidifications in the Arctic, in: AMAP Assessment Report: Arctic Pollution Issues. Arctic Monitoring and Assessment Programme (AMAP), Arctic Monitoring and Assessment Programme, Oslo, Norway, 859, 1998.

Kanaya, Y., Miyazaki, K., Taketani, F., Miyakawa, T., Takashima, H., Komazaki, Y., Pan, X., Kato, S., Sudo, K., Sekiya, T., Inoue, J., Sato, K., and Oshima, K.: Ozone and carbon monoxide observations over open oceans on R/V Mirai from 67° S to 75° N during 2012 to 2017: testing global chemical reanalysis in terms of Arctic processes, low ozone levels at low latitudes,
1440 and pollution transport, Atmos Chem Phys, 19, 7233–7254, https://doi.org/10.5194/acp-19-7233-2019, 2019.

Kanaya, Y., Sommariva, R., Saiz-Lopez, A., Mazzeo, A., Koenig, T., Kawana, K., Johnson, J., Colomb, A., Tulet, P., Molloy, S., Galbally, I., Volkamer, R., Mahajan, A., Halfacre, J., Shepson, P., Schmale, J., Angot, H., Blomquist, B., Shupe, M. D., Helmig, D., Gil, J., Lee, M., Chen, G., Lee, J., Aikin, K., Parrish, D., Holloway, J., Ryerson, T., Pollack, I., Williams, E., Lerner, B., Weiheimer, A., Campos, T., Flocke, F., Spackman, R., Staebler, R., Aliabadi, A. A., Gong, W., Van Malderen, R.,
1445 Thompson, A. M., Stauffer, R., Kollonige, D. E., Martin, J.-C. G., Fujiwara, M., Read, K., Rowlinson, M., Sato, K., Kurokawa, J., Iwamoto, Y., Taketani, F., Takashima, H., Comas, M. N., Panagi, M., and Schultz, M.: Observational ozone data over the global oceans and polar regions: The TOAR-II Oceans data set version 2024, Submitt. ESSD, 2024.

Krnavek, L., Simpson, W. R., Carlson, D., Domine, F., Douglas, T. A., and Sturm, M.: The chemical composition of surface snow in the Arctic: Examining marine, terrestrial, and atmospheric influences, Atmos. Environ., 50, 349–359,
1450 https://doi.org/10.1016/j.atmosenv.2011.11.033, 2012.

Law, K. S., Stohl, A., Quinn, P. K., Brock, C. A., Burkhart, J. F., Paris, J.-D., Ancellet, G., Singh, H. B., Roiger, A., Schlager, H., Dibb, J., Jacob, D. J., Arnold, S. R., Pelon, J., and Thomas, J. L.: Arctic Air Pollution: New Insights from POLARCAT-IPY, Bull. Am. Meteorol. Soc., 95, 1873–1895, https://doi.org/10.1175/BAMS-D-13-00017.1, 2014.

Law, K. S., Hjorth, J. L., Pernov, J. B., Whaley, C. H., Skov, H., Collaud Coen, M., Langner, J., Arnold, S. R., Tarasick, D.,
1455 Christensen, J., Deushi, M., Effertz, P., Faluvegi, G., Gauss, M., Im, U., Oshima, N., Petropavlovskikh, I., Plummer, D.,
Tsigaridis, K., Tsyro, S., Solberg, S., and Turnock, S. T.: Arctic Tropospheric Ozone Trends, Geophys. Res. Lett., 50,
e2023GL103096, https://doi.org/10.1029/2023GL103096, 2023.

Leaitch, W. R., Korolev, A., Aliabadi, A. A., Burkart, J., Willis, M. D., Abbatt, J. P. D., Bozem, H., Hoor, P., Köllner, F.,
Schneider, J., Herber, A., Konrad, C., and Brauner, R.: Effects of 20–100 nm particles on liquid clouds in the clean summertime
1460 Arctic, Atmos Chem Phys, 16, 11107–11124, https://doi.org/10.5194/acp-16-11107-2016, 2016.

Lehrer, E., Wagenbach, D., and Platt, U.: Aerosol chemical composition during tropospheric ozone depletion at Ny
Ålesund/Svalbard, Tellus B Chem. Phys. Meteorol., https://doi.org/10.3402/tellusb.v49i5.15987, 1997.

Lehrer, E., Hönninger, G., and Platt, U.: A one dimensional model study of the mechanism of halogen liberation and vertical
transport in the polar troposphere, Atmos Chem Phys, 4, 2427–2440, https://doi.org/10.5194/acp-4-2427-2004, 2004.

1465 Logan, J. A.: An analysis of ozonesonde data for the troposphere: Recommendations for testing 3-D models and development
of a gridded climatology for tropospheric ozone, J. Geophys. Res. Atmospheres, 104, 16115–16149,
https://doi.org/10.1029/1998JD100096, 1999.

Long, R. W., Whitehill, A., Habel, A., Urbanski, S., Halliday, H., Colón, M., Kaushik, S., and Landis, M. S.: Comparison of
ozone measurement methods in biomass burning smoke: an evaluation under field and laboratory conditions, Atmos Meas
1470 Tech, 14, 1783–1800, https://doi.org/10.5194/amt-14-1783-2021, 2021.

Lurmann, F. W., Lloyd, A. C., and Atkinson, R.: A chemical mechanism for use in long-range transport/acid deposition
computer modeling, J. Geophys. Res. Atmospheres, 91, 10905–10936, https://doi.org/10.1029/JD091iD10p10905, 1986.

Magnussen, S. and Taylor, S. W.: Inter- and intra-annual profiles of fire regimes in the managed forests of Canada and
implications for resource sharing, Int. J. Wildland Fire, 21, 328–341, 2012.

1475 Mahajan, A. S., Shaw, M., Oetjen, H., Hornsby, K. E., Carpenter, L. J., Kaleschke, L., Tian-Kunze, X., Lee, J. D., Moller, S.
J., Edwards, P., Commane, R., Ingham, T., Heard, D. E., and Plane, J. M. C.: Evidence of reactive iodine chemistry in the
Arctic boundary layer, J. Geophys. Res. Atmospheres, 115, https://doi.org/10.1029/2009JD013665, 2010.

Makar, P. A., Bouchet, V. S., and Nenes, A.: Inorganic chemistry calculations using HETV—a vectorized solver for the
SO_4^{2-}–NO_3^-–NH_4^+ system based on the ISORROPIA algorithms, Atmos. Environ., 37, 2279–2294,
1480 https://doi.org/10.1016/S1352-2310(03)00074-8, 2003.

Makar, P. A., Gong, W., Milbrandt, J., Hogrefe, C., Zhang, Y., Curci, G., Žabkar, R., Im, U., Balzarini, A., Baró, R., Bianconi,
R., Cheung, P., Forkel, R., Gravel, S., Hirtl, M., Honzak, L., Hou, A., Jiménez-Guerrero, P., Langer, M., Moran, M. D., Pabla,
B., Pérez, J. L., Pirovano, G., San José, R., Tuccella, P., Werhahn, J., Zhang, J., and Galmarini, S.: Feedbacks between air
pollution and weather, Part 1: Effects on weather, Atmos. Environ., 115, 442–469,
1485 https://doi.org/10.1016/j.atmosenv.2014.12.003, 2015a.

Makar, P. A., Gong, W., Hogrefe, C., Zhang, Y., Curci, G., Žabkar, R., Milbrandt, J., Im, U., Balzarini, A., Baró, R., Bianconi,
R., Cheung, P., Forkel, R., Gravel, S., Hirtl, M., Honzak, L., Hou, A., Jiménez-Guerrero, P., Langer, M., Moran, M. D., Pabla,
B., Pérez, J. L., Pirovano, G., San José, R., Tuccella, P., Werhahn, J., Zhang, J., and Galmarini, S.: Feedbacks between air
pollution and weather, part 2: Effects on chemistry, Atmos. Environ., 115, 499–526,
1490 https://doi.org/10.1016/j.atmosenv.2014.10.021, 2015b.

Marelle, L., Thomas, J. L., Ahmed, S., Tuite, K., Stutz, J., Dommergue, A., Simpson, W. R., Frey, M. M., and Baladima, F.: Implementation and Impacts of Surface and Blowing Snow Sources of Arctic Bromine Activation Within WRF-Chem 4.1.1, J. Adv. Model. Earth Syst., 13, e2020MS002391, https://doi.org/10.1029/2020MS002391, 2021.

Mårtensson, E. M., Nilsson, E. D., de Leeuw, G., Cohen, L. H., and Hansson, H.-C.: Laboratory simulations and parameterization of the primary marine aerosol production, J. Geophys. Res. Atmospheres, 108, https://doi.org/10.1029/2002JD002263, 2003.

Massling, A., Nielsen, I. E., Kristensen, D., Christensen, J. H., Sørensen, L. L., Jensen, B., Nguyen, Q. T., Nøjgaard, J. K., Glasius, M., and Skov, H.: Atmospheric black carbon and sulfate concentrations in Northeast Greenland, Atmos Chem Phys, 15, 9681–9692, https://doi.org/10.5194/acp-15-9681-2015, 2015.

McDuffie, E. E., Fibiger, D. L., Dubé, W. P., Lopez-Hilfiker, F., Lee, B. H., Thornton, J. A., Shah, V., Jaeglé, L., Guo, H., Weber, R. J., Michael Reeves, J., Weinheimer, A. J., Schroder, J. C., Campuzano-Jost, P., Jimenez, J. L., Dibb, J. E., Veres, P., Ebben, C., Sparks, T. L., Wooldridge, P. J., Cohen, R. C., Hornbrook, R. S., Apel, E. C., Campos, T., Hall, S. R., Ullmann, K., and Brown, S. S.: Heterogeneous N2O5 Uptake During Winter: Aircraft Measurements During the 2015 WINTER Campaign and Critical Evaluation of Current Parameterizations, J. Geophys. Res. Atmospheres, 123, 4345–4372, https://doi.org/10.1002/2018JD028336, 2018.

Michalowski, B. A., Francisco, J. S., Li, S.-M., Barrie, L. A., Bottenheim, J. W., and Shepson, P. B.: A computer model study of multiphase chemistry in the Arctic boundary layer during polar sunrise, J. Geophys. Res. Atmospheres, 105, 15131–15145, https://doi.org/10.1029/2000JD900004, 2000.

Moeini, O., Tarasick, D. W., McElroy, C. T., Liu, J., Osman, M. K., Thompson, A. M., Parrington, M., Palmer, P. I., Johnson, B., Oltmans, S. J., and Merrill, J.: Estimating wildfire-generated ozone over North America using ozonesonde profiles and a differential back trajectory technique, Atmospheric Environ. X, 7, 100078, https://doi.org/10.1016/j.aeaoa.2020.100078, 2020.

Monahan, E. C., Spiel, D. E., and Davidson, K. L.: A Model of Marine Aerosol Generation Via Whitecaps and Wave Disruption, in: Oceanic Whitecaps: And Their Role in Air-Sea Exchange Processes, edited by: Monahan, E. C. and Niocaill, G. M., Springer Netherlands, Dordrecht, 167–174, https://doi.org/10.1007/978-94-009-4668-2_16, 1986.

Monks, P. S., Archibald, A. T., Colette, A., Cooper, O., Coyle, M., Derwent, R., Fowler, D., Granier, C., Law, K. S., Mills, G. E., Stevenson, D. S., Tarasova, O., Thouret, V., von Schneidemesser, E., Sommariva, R., Wild, O., and Williams, M. L.: Tropospheric ozone and its precursors from the urban to the global scale from air quality to short-lived climate forcer, Atmos Chem Phys, 15, 8889–8973, https://doi.org/10.5194/acp-15-8889-2015, 2015a.

Monks, S. A., Arnold, S. R., Emmons, L. K., Law, K. S., Turquety, S., Duncan, B. N., Flemming, J., Huijnen, V., Tilmes, S., Langner, J., Mao, J., Long, Y., Thomas, J. L., Steenrod, S. D., Raut, J. C., Wilson, C., Chipperfield, M. P., Diskin, G. S., Weinheimer, A., Schlager, H., and Ancellet, G.: Multi-model study of chemical and physical controls on transport of anthropogenic and biomass burning pollution to the Arctic, Atmos Chem Phys, 15, 3575–3603, https://doi.org/10.5194/acp-15-3575-2015, 2015b.

Moran, M. D., Pavlovic, R., and Anselmo, D.: Regional Air Quality Deterministic Prediction System (RAQDPS): Update from version 019 to version 020, 2018.

Nenes, A., Pandis, S. N., and Pilinis, C.: Continued development and testing of a new thermodynamic aerosol module for urban and regional air quality models, Atmos. Environ., 33, 1553–1560, https://doi.org/10.1016/S1352-2310(98)00352-5, 1999.

Odum, J. R., Hoffmann, T., Bowman, F., Collins, D., Flagan, R. C., and Seinfeld, J. H.: Gas/Particle Partitioning and Secondary
1530 Organic Aerosol Yields, Environ. Sci. Technol., 30, 2580–2585, https://doi.org/10.1021/es950943+, 1996.

Oltmans, S. J., Johnson, B. J., and Harris, J. M.: Springtime boundary layer ozone depletion at Barrow, Alaska: Meteorological
influence, year-to-year variation, and long-term change, J. Geophys. Res. Atmospheres, 117,
https://doi.org/10.1029/2011JD016889, 2012.

Orlando, J. J. and Burkholder, J. B.: Identification of BrONO as the Major Product in the Gas-Phase Reaction of Br with NO2,
1535 J. Phys. Chem. A, 104, 2048–2053, https://doi.org/10.1021/jp993713g, 2000.

Oum, K. W., Lakin, M. J., and Finlayson-Pitts, B. J.: Bromine activation in the troposphere by the dark reaction of O3 with
seawater ice, Geophys. Res. Lett., 25, 3923–3926, https://doi.org/10.1029/1998GL900078, 1998.

Pernov, J. B., Bossi, R., Lebourgeois, T., Nøjgaard, J. K., Holzinger, R., Hjorth, J. L., and Skov, H.: Atmospheric VOC
measurements at a High Arctic site: characteristics and source apportionment, Atmos Chem Phys, 21, 2895–2916,
1540 https://doi.org/10.5194/acp-21-2895-2021, 2021.

Pernov, J. B., Hjorth, J. L., Sørensen, L. L., and Skov, H.: On the dynamics of ozone depletion events at Villum Research
Station in the High Arctic, EGUsphere, 2024, 1–42, https://doi.org/10.5194/egusphere-2024-1676, 2024.

Peterson, P. K., Pöhler, D., Sihler, H., Zielcke, J., General, S., Frieß, U., Platt, U., Simpson, W. R., Nghiem, S. V., Shepson,
P. B., Stirm, B. H., Dhaniyala, S., Wagner, T., Caulton, D. R., Fuentes, J. D., and Pratt, K. A.: Observations of bromine
1545 monoxide transport in the Arctic sustained on aerosol particles, Atmos Chem Phys, 17, 7567–7579,
https://doi.org/10.5194/acp-17-7567-2017, 2017.

Peterson, P. K., Hartwig, M., May, N. W., Schwartz, E., Rigor, I., Ermold, W., Steele, M., Morison, J. H., Nghiem, S. V., and
Pratt, K. A.: Snowpack measurements suggest role for multi-year sea ice regions in Arctic atmospheric bromine and chlorine
chemistry, Elem. Sci. Anthr., 7, 14, https://doi.org/10.1525/elementa.352, 2019.

1550 Pfister, G. G., Emmons, L. K., Hess, P. G., Honrath, R., Lamarque, J.-F., Val Martin, M., Owen, R. C., Avery, M. A., Browell,
E. V., Holloway, J. S., Nedelec, P., Purvis, R., Ryerson, T. B., Sachse, G. W., and Schlager, H.: Ozone production from the
2004 North American boreal fires, J. Geophys. Res. Atmospheres, 111, https://doi.org/10.1029/2006JD007695, 2006.

Platt, S. M., Hov, Ø., Berg, T., Breivik, K., Eckhardt, S., Eleftheriadis, K., Evangeliou, N., Fiebig, M., Fisher, R., Hansen, G.,
Hansson, H.-C., Heintzenberg, J., Hermansen, O., Heslin-Rees, D., Holmén, K., Hudson, S., Kallenborn, R., Krejci, R.,
1555 Krognes, T., Larssen, S., Lowry, D., Lund Myhre, C., Lunder, C., Nisbet, E., Nizzetto, P. B., Park, K.-T., Pedersen, C. A.,
Aspmo Pfaffhuber, K., Röckmann, T., Schmidbauer, N., Solberg, S., Stohl, A., Ström, J., Svendby, T., Tunved, P., Tørnkvist,
K., van der Veen, C., Vratolis, S., Yoon, Y. J., Yttri, K. E., Zieger, P., Aas, W., and Tørseth, K.: Atmospheric composition in
the European Arctic and 30 years of the Zeppelin Observatory, Ny-Ålesund, Atmos Chem Phys, 22, 3321–3369,
https://doi.org/10.5194/acp-22-3321-2022, 2022.

1560 Pratt, K. A., Custard, K. D., Shepson, P. B., Douglas, T. A., Pöhler, D., General, S., Zielcke, J., Simpson, W. R., Platt, U.,
Tanner, D. J., Gregory Huey, L., Carlsen, M., and Stirm, B. H.: Photochemical production of molecular bromine in Arctic
surface snowpacks, Nat. Geosci., 6, 351–356, https://doi.org/10.1038/ngeo1779, 2013.

Rantanen, M., Karpechko, A. Yu., Lipponen, A., Nordling, K., Hyvärinen, O., Ruosteenoja, K., Vihma, T., and Laaksonen,
A.: The Arctic has warmed nearly four times faster than the globe since 1979, Commun. Earth Environ., 3, 168,
1565 https://doi.org/10.1038/s43247-022-00498-3, 2022.

Saiz-Lopez, A. and von Glasow, R.: Reactive halogen chemistry in the troposphere, Chem. Soc. Rev., 41, 6448–6472, https://doi.org/10.1039/C2CS35208G, 2012.

Sander, R., Jöckel, P., Kirner, O., Kunert, A. T., Landgraf, J., and Pozzer, A.: The photolysis module JVAL-14, compatible with the MESSy standard, and the JVal PreProcessor (JVPP), Geosci. Model Dev., 7, 2653–2662, https://doi.org/10.5194/gmd-7-2653-2014, 2014.

Sandu, A. and Sander, R.: Technical note: Simulating chemical systems in Fortran90 and Matlab with the Kinetic PreProcessor KPP-2.1, Atmos Chem Phys, 6, 187–195, https://doi.org/10.5194/acp-6-187-2006, 2006.

Sarwar, G., Gantt, B., Schwede, D., Foley, K., Mathur, R., and Saiz-Lopez, A.: Impact of Enhanced Ozone Deposition and Halogen Chemistry on Tropospheric Ozone over the Northern Hemisphere, Environ. Sci. Technol., 49, 9203–9211, https://doi.org/10.1021/acs.est.5b01657, 2015.

Schweitzer, F., Mirabel, P., and George, C.: Uptake of Hydrogen Halides by Water Droplets, J. Phys. Chem. A, 104, 72–76, https://doi.org/10.1021/jp992621o, 2000.

Shindell, D. T., Chin, M., Dentener, F., Doherty, R. M., Faluvegi, G., Fiore, A. M., Hess, P., Koch, D. M., MacKenzie, I. A., Sanderson, M. G., Schultz, M. G., Schulz, M., Stevenson, D. S., Teich, H., Textor, C., Wild, O., Bergmann, D. J., Bey, I., Bian, H., Cuvelier, C., Duncan, B. N., Folberth, G., Horowitz, L. W., Jonson, J., Kaminski, J. W., Marmer, E., Park, R., Pringle, K. J., Schroeder, S., Szopa, S., Takemura, T., Zeng, G., Keating, T. J., and Zuber, A.: A multi-model assessment of pollution transport to the Arctic, Atmos Chem Phys, 8, 5353–5372, https://doi.org/10.5194/acp-8-5353-2008, 2008.

Simpson, D., Benedictow, A., Berge, H., Bergström, R., Emberson, L. D., Fagerli, H., Flechard, C. R., Hayman, G. D., Gauss, M., Jonson, J. E., Jenkin, M. E., Nyíri, A., Richter, C., Semeena, V. S., Tsyro, S., Tuovinen, J.-P., Valdebenito, Á., and Wind, P.: The EMEP MSC-W chemical transport model – technical description, Atmos Chem Phys, 12, 7825–7865, https://doi.org/10.5194/acp-12-7825-2012, 2012.

Simpson, W.: Atmospheric measurements via Multiple Axis Differential Optical Absorption Spectroscopy (MAXDOAS), Utqiagvik (Barrow), Alaska 2012-2018, https://doi.org/10.18739/A2222R550, 2018.

Simpson, W., Perovich, Donald, Matrai, P., Shepson, P., and Chavez, F.: The Collaborative O-Buoy Project: Deployment of a Network of Arctic Ocean Chemical Sensors for the IPY and beyond (urn:uuid:b43c0daa-162b-4c45-95da-4baf82d6958b), https://doi.org/10.18739/A2WD4W, 2009.

Simpson, W. R., Alvarez-Aviles, L., Douglas, T. A., Sturm, M., and Domine, F.: Halogens in the coastal snow pack near Barrow, Alaska: Evidence for active bromine air-snow chemistry during springtime, Geophys. Res. Lett., 32, https://doi.org/10.1029/2004GL021748, 2005.

Simpson, W. R., von Glasow, R., Riedel, K., Anderson, P., Ariya, P., Bottenheim, J., Burrows, J., Carpenter, L. J., Frieß, U., Goodsite, M. E., Heard, D., Hutterli, M., Jacobi, H.-W., Kaleschke, L., Neff, B., Plane, J., Platt, U., Richter, A., Roscoe, H., Sander, R., Shepson, P., Sodeau, J., Steffen, A., Wagner, T., and Wolff, E.: Halogens and their role in polar boundary-layer ozone depletion, Atmos Chem Phys, 7, 4375–4418, https://doi.org/10.5194/acp-7-4375-2007, 2007.

Simpson, W. R., Peterson, P. K., Frieß, U., Sihler, H., Lampel, J., Platt, U., Moore, C., Pratt, K., Shepson, P., Halfacre, J., and Nghiem, S. V.: Horizontal and vertical structure of reactive bromine events probed by bromine monoxide MAX-DOAS, Atmos Chem Phys, 17, 9291–9309, https://doi.org/10.5194/acp-17-9291-2017, 2017.

Singh, H. B., Anderson, B. E., Brune, W. H., Cai, C., Cohen, R. C., Crawford, J. H., Cubison, M. J., Czech, E. P., Emmons, L., Fuelberg, H. E., Huey, G., Jacob, D. J., Jimenez, J. L., Kaduwela, A., Kondo, Y., Mao, J., Olson, J. R., Sachse, G. W., Vay,

S. A., Weinheimer, A., Wennberg, P. O., and Wisthaler, A.: Pollution influences on atmospheric composition and chemistry
1605 at high northern latitudes: Boreal and California forest fire emissions, Atmos. Environ., 44, 4553–4564,
https://doi.org/10.1016/j.atmosenv.2010.08.026, 2010.

Skamarock, W. C., Klemp, J. B., Dudhia, J., Gill, D. O., Barker, D., Wang, W., and Powers, J. G.: A Description of the
Advanced Research WRF Model Version 3, 2008.

Skov, H., Christensen, J. H., Goodsite, M. E., Heidam, N. Z., Jensen, B., Wåhlin, P., and Geernaert, G.: Fate of Elemental
1610 Mercury in the Arctic during Atmospheric Mercury Depletion Episodes and the Load of Atmospheric Mercury to the Arctic,
Environ. Sci. Technol., 38, 2373–2382, https://doi.org/10.1021/es030080h, 2004.

Skov, H., Hjorth, J., Nordstrøm, C., Jensen, B., Christoffersen, C., Bech Poulsen, M., Baldtzer Liisberg, J., Beddows, D.,
Dall'Osto, M., and Christensen, J. H.: Variability in gaseous elemental mercury at Villum Research Station, Station Nord, in
North Greenland from 1999 to 2017, Atmos Chem Phys, 20, 13253–13265, https://doi.org/10.5194/acp-20-13253-2020, 2020.

1615 Smith, G. C., Roy, F., Reszka, M., Surcel Colan, D., He, Z., Deacu, D., Belanger, J.-M., Skachko, S., Liu, Y., Dupont, F.,
Lemieux, J.-F., Beaudoin, C., Tranchant, B., Drévillon, M., Garric, G., Testut, C.-E., Lellouche, J.-M., Pellerin, P., Ritchie,
H., Lu, Y., Davidson, F., Buehner, M., Caya, A., and Lajoie, M.: Sea ice forecast verification in the Canadian Global Ice Ocean
Prediction System, Q. J. R. Meteorol. Soc., 142, 659–671, https://doi.org/10.1002/qj.2555, 2016.

Soares, J., Sofiev, M., Geels, C., Christensen, J. H., Andersson, C., Tsyro, S., and Langner, J.: Impact of climate change on
1620 the production and transport of sea salt aerosol on European seas, Atmos Chem Phys, 16, 13081–13104,
https://doi.org/10.5194/acp-16-13081-2016, 2016.

Solberg, S., Schmidbauer, N., Semb, A., Stordal, F., and Hov, Ø.: Boundary-layer ozone depletion as seen in the Norwegian
Arctic in spring, J. Atmospheric Chem., 23, 301–332, https://doi.org/10.1007/BF00055158, 1996.

Sommar, J., Andersson, M. E., and Jacobi, H.-W.: Circumpolar measurements of speciated mercury, ozone and carbon
1625 monoxide in the boundary layer of the Arctic Ocean, Atmos Chem Phys, 10, 5031–5045, https://doi.org/10.5194/acp-10-5031-
2010, 2010.

Strand, A. and Hov, Ø.: A two-dimensional global study of tropospheric ozone production, J. Geophys. Res. Atmospheres, 99,
22877–22895, https://doi.org/10.1029/94JD01945, 1994.

Stroud, C. A., Makar, P. A., Zhang, J., Moran, M. D., Akingunola, A., Li, S.-M., Leithead, A., Hayden, K., and Siu, M.:
1630 Improving air quality model predictions of organic species using measurement-derived organic gaseous and particle emissions
in a petrochemical-dominated region, Atmos Chem Phys, 18, 13531–13545, https://doi.org/10.5194/acp-18-13531-2018,
2018.

Swanson, W. F., Graham, K. A., Halfacre, J. W., Holmes, C. D., Shepson, P. B., and Simpson, W. R.: Arctic Reactive Bromine
Events Occur in Two Distinct Sets of Environmental Conditions: A Statistical Analysis of 6 Years of Observations, J. Geophys.
1635 Res. Atmospheres, 125, e2019JD032139, https://doi.org/10.1029/2019JD032139, 2020.

Swanson, W. F., Holmes, C. D., Simpson, W. R., Confer, K., Marelle, L., Thomas, J. L., Jaeglé, L., Alexander, B., Zhai, S.,
Chen, Q., Wang, X., and Sherwen, T.: Comparison of model and ground observations finds snowpack and blowing snow
aerosols both contribute to Arctic tropospheric reactive bromine, Atmos Chem Phys, 22, 14467–14488,
https://doi.org/10.5194/acp-22-14467-2022, 2022.

1640   Thomas, D. C., Christensen, J. H., Massling, A., Pernov, J. B., and Skov, H.: The effect of the 2020 COVID-19 lockdown on atmospheric black carbon levels in northeastern Greenland, Atmos. Environ., 269, 118853, https://doi.org/10.1016/j.atmosenv.2021.118853, 2022.

Thomas, J. L., Raut, J.-C., Law, K. S., Marelle, L., Ancellet, G., Ravetta, F., Fast, J. D., Pfister, G., Emmons, L. K., Diskin, G. S., Weinheimer, A., Roiger, A., and Schlager, H.: Pollution transport from North America to Greenland during summer
1645   2008, Atmos Chem Phys, 13, 3825–3848, https://doi.org/10.5194/acp-13-3825-2013, 2013.

Toyota, K., McConnell, J. C., Lupu, A., Neary, L., McLinden, C. A., Richter, A., Kwok, R., Semeniuk, K., Kaminski, J. W., Gong, S.-L., Jarosz, J., Chipperfield, M. P., and Sioris, C. E.: Analysis of reactive bromine production and ozone depletion in the Arctic boundary layer using 3-D simulations with GEM-AQ: inference from synoptic-scale patterns, Atmos Chem Phys, 11, 3949–3979, https://doi.org/10.5194/acp-11-3949-2011, 2011.

1650   Toyota, K., McConnell, J. C., Staebler, R. M., and Dastoor, A. P.: Air–snowpack exchange of bromine, ozone and mercury in the springtime Arctic simulated by the 1-D model PHANTAS – Part 1: In-snow bromine activation and its impact on ozone, Atmospheric Chem. Phys., 14, 4101–4133, https://doi.org/10.5194/acp-14-4101-2014, 2014.

Tschudi, M. A., Meier, W. N., and Stewart, J. S.: An enhancement to sea ice motion and age products at the National Snow and Ice Data Center (NSIDC), The Cryosphere, 14, 1519–1536, https://doi.org/10.5194/tc-14-1519-2020, 2020.

1655   Uttal, T., Makshtas, A., and Laurila, T.: The Tiksi International Hydrometeorological Observatory - An Arctic members Partnership, Bull. World Meteorol. Organ., 62, 22–26, 2013.

Uttal, T., Starkweather, S., Drummond, J. R., Vihma, T., Makshtas, A. P., Darby, L. S., Burkhart, J. F., Cox, C. J., Schmeisser, L. N., Haiden, T., Maturilli, M., Shupe, M. D., De Boer, G., Saha, A., Grachev, A. A., Crepinsek, S. M., Bruhwiler, L., Goodison, B., McArthur, B., Walden, V. P., Dlugokencky, E. J., Persson, P. O. G., Lesins, G., Laurila, T., Ogren, J. A., Stone,
1660   R., Long, C. N., Sharma, S., Massling, A., Turner, D. D., Stanitski, D. M., Asmi, E., Aurela, M., Skov, H., Eleftheriadis, K., Virkkula, A., Platt, A., Førland, E. J., Iijima, Y., Nielsen, I. E., Bergin, M. H., Candlish, L., Zimov, N. S., Zimov, S. A., O'Neill, N. T., Fogal, P. F., Kivi, R., Konopleva-Akish, E. A., Verlinde, J., Kustov, V. Y., Vasel, B., Ivakhov, V. M., Viisanen, Y., and Intrieri, J. M.: International Arctic Systems for Observing the Atmosphere: An International Polar Year Legacy Consortium, Bull. Am. Meteorol. Soc., 97, 1033–1056, https://doi.org/10.1175/BAMS-D-14-00145.1, 2016.

1665   Van Dam, B., Helmig, D., Burkhart, J. F., Obrist, D., and Oltmans, S. J.: Springtime boundary layer O3 and GEM depletion at Toolik Lake, Alaska, J. Geophys. Res. Atmospheres, 118, 3382–3391, https://doi.org/10.1002/jgrd.50213, 2013.

Van Dam, B., Helmig, D., Doskey, P. V., and Oltmans, S. J.: Summertime surface O3 behavior and deposition to tundra in the Alaskan Arctic, J. Geophys. Res. Atmospheres, 121, 8055–8066, https://doi.org/10.1002/2015JD023914, 2016.

Van Malderen, R., Thompson, A. M., Kollonige, D. E., Stauffer, R. M., Smit, H. G. J., Chang, K.-L., and et al.: Global Ground-
1670   based Tropospheric Ozone Measurements: Reference Data and Individual Site Trends (2000-2022) from the TOAR-II/HEGIFTOM Project, Submitt. ACP, 2024.

Wachsmuth, M., Gäggeler, H. W., von Glasow, R., and Ammann, M.: Accommodation coefficient of HOBr on deliquescent sodium bromide aerosol particles, Atmos Chem Phys, 2, 121–131, https://doi.org/10.5194/acp-2-121-2002, 2002.

Wagner, A., Bennouna, Y., Blechschmidt, A.-M., Brasseur, G., Chabrillat, S., Christophe, Y., Errera, Q., Eskes, H., Flemming,
1675   J., Hansen, K. M., Inness, A., Kapsomenakis, J., Langerock, B., Richter, A., Sudarchikova, N., Thouret, V., and Zerefos, C.: Comprehensive evaluation of the Copernicus Atmosphere Monitoring Service (CAMS) reanalysis against independent observations: Reactive gases, Elem. Sci. Anthr., 9, 00171, https://doi.org/10.1525/elementa.2020.00171, 2021.

Walker, T. W., Jones, D. B. A., Parrington, M., Henze, D. K., Murray, L. T., Bottenheim, J. W., Anlauf, K., Worden, J. R., Bowman, K. W., Shim, C., Singh, K., Kopacz, M., Tarasick, D. W., Davies, J., von der Gathen, P., Thompson, A. M., and
1680 Carouge, C. C.: Impacts of midlatitude precursor emissions and local photochemistry on ozone abundances in the Arctic, J. Geophys. Res. Atmospheres, 117, https://doi.org/10.1029/2011JD016370, 2012.

Wang, S., McNamara, S. M., Moore, C. W., Obrist, D., Steffen, A., Shepson, P. B., Staebler, R. M., Raso, A. R. W., and Pratt, K. A.: Direct detection of atmospheric atomic bromine leading to mercury and ozone depletion, Proc. Natl. Acad. Sci., 116, 14479–14484, https://doi.org/10.1073/pnas.1900613116, 2019.

1685 Wang, Y., Ridley, B., Fried, A., Cantrell, C., Davis, D., Chen, G., Snow, J., Heikes, B., Talbot, R., Dibb, J., Flocke, F., Weinheimer, A., Blake, N., Blake, D., Shetter, R., Lefer, B., Atlas, E., Coffey, M., Walega, J., and Wert, B.: Springtime photochemistry at northern mid and high latitudes, J. Geophys. Res. Atmospheres, 108, https://doi.org/10.1029/2002JD002227, 2003.

Wesely, M. L.: Parameterization of surface resistances to gaseous dry deposition in regional-scale numerical models,
1690 Atmospheric Environ. 1967, 23, 1293–1304, https://doi.org/10.1016/0004-6981(89)90153-4, 1989.

Whaley, C. H., Mahmood, R., von Salzen, K., Winter, B., Eckhardt, S., Arnold, S., Beagley, S., Becagli, S., Chien, R.-Y., Christensen, J., Damani, S. M., Dong, X., Eleftheriadis, K., Evangeliou, N., Faluvegi, G., Flanner, M., Fu, J. S., Gauss, M., Giardi, F., Gong, W., Hjorth, J. L., Huang, L., Im, U., Kanaya, Y., Krishnan, S., Klimont, Z., Kühn, T., Langner, J., Law, K. S., Marelle, L., Massling, A., Olivié, D., Onishi, T., Oshima, N., Peng, Y., Plummer, D. A., Popovicheva, O., Pozzoli, L., Raut,
1695 J.-C., Sand, M., Saunders, L. N., Schmale, J., Sharma, S., Skeie, R. B., Skov, H., Taketani, F., Thomas, M. A., Traversi, R., Tsigaridis, K., Tsyro, S., Turnock, S., Vitale, V., Walker, K. A., Wang, M., Watson-Parris, D., and Weiss-Gibbons, T.: Model evaluation of short-lived climate forcers for the Arctic Monitoring and Assessment Programme: a multi-species, multi-model study, Atmos Chem Phys, 22, 5775–5828, https://doi.org/10.5194/acp-22-5775-2022, 2022.

Whaley, C. H., Law, K. S., Hjorth, J. L., Skov, H., Arnold, S. R., Langner, J., Pernov, J. B., Bergeron, G., Bourgeois, I.,
1700 Christensen, J. H., Chien, R.-Y., Deushi, M., Dong, X., Effertz, P., Faluvegi, G., Flanner, M., Fu, J. S., Gauss, M., Huey, G., Im, U., Kivi, R., Marelle, L., Onishi, T., Oshima, N., Petropavlovskikh, I., Peischl, J., Plummer, D. A., Pozzoli, L., Raut, J.-C., Ryerson, T., Skeie, R., Solberg, S., Thomas, M. A., Thompson, C., Tsigaridis, K., Tsyro, S., Turnock, S. T., von Salzen, K., and Tarasick, D. W.: Arctic tropospheric ozone: assessment of current knowledge and model performance, Atmos Chem Phys, 23, 637–661, https://doi.org/10.5194/acp-23-637-2023, 2023.

1705 Wittrock, F., Müller, R., Richter, A., Bovensmann, H., and Burrows, J. P.: Measurements of iodine monoxide (IO) above Spitsbergen, Geophys. Res. Lett., 27, 1471–1474, https://doi.org/10.1029/1999GL011146, 2000.

Yang, X., Cox, R. A., Warwick, N. J., Pyle, J. A., Carver, G. D., O'Connor, F. M., and Savage, N. H.: Tropospheric bromine chemistry and its impacts on ozone: A model study, J. Geophys. Res. Atmospheres, 110, https://doi.org/10.1029/2005JD006244, 2005.

1710 Yang, X., Pyle, J. A., and Cox, R. A.: Sea salt aerosol production and bromine release: Role of snow on sea ice, Geophys. Res. Lett., 35, https://doi.org/10.1029/2008GL034536, 2008.

Yang, X., Pyle, J. A., Cox, R. A., Theys, N., and Van Roozendael, M.: Snow-sourced bromine and its implications for polar tropospheric ozone, Atmos Chem Phys, 10, 7763–7773, https://doi.org/10.5194/acp-10-7763-2010, 2010.

Yang, X., Blechschmidt, A.-M., Bognar, K., McClure-Begley, A., Morris, S., Petropavlovskikh, I., Richter, A., Skov, H.,
1715 Strong, K., Tarasick, D. W., Uttal, T., Vestenius, M., and Zhao, X.: Pan-Arctic surface ozone: modelling vs. measurements, Atmos Chem Phys, 20, 15937–15967, https://doi.org/10.5194/acp-20-15937-2020, 2020.

Young, P. J., Naik, V., Fiore, A. M., Gaudel, A., Guo, J., Lin, M. Y., Neu, J. L., Parrish, D. D., Rieder, H. E., Schnell, J. L., Tilmes, S., Wild, O., Zhang, L., Ziemke, J., Brandt, J., Delcloo, A., Doherty, R. M., Geels, C., Hegglin, M. I., Hu, L., Im, U., Kumar, R., Luhar, A., Murray, L., Plummer, D., Rodriguez, J., Saiz-Lopez, A., Schultz, M. G., Woodhouse, M. T., and Zeng, G.: Tropospheric Ozone Assessment Report: Assessment of global-scale model performance for global and regional ozone distributions, variability, and trends, Elem. Sci. Anthr., 6, 10, https://doi.org/10.1525/elementa.265, 2018.

Zhai, S., Swanson, W., McConnell, J. R., Chellman, N., Opel, T., Sigl, M., Meyer, H., Wang, X., Jaeglé, L., Stutz, J., Dibb, J. E., Fujita, K., and Alexander, B.: Implications of Snowpack Reactive Bromine Production for Arctic Ice Core Bromine Preservation, J. Geophys. Res. Atmospheres, 128, e2023JD039257, https://doi.org/10.1029/2023JD039257, 2023.

Zhang, L., Gong, S., Padro, J., and Barrie, L.: A size-segregated particle dry deposition scheme for an atmospheric aerosol module, Atmos. Environ., 35, 549–560, https://doi.org/10.1016/S1352-2310(00)00326-5, 2001.